Gust Load Alleviation Exploiting Structural Nonlinearity

Thesis submitted in accordance with the requirements of
the University of Liverpool for the degree of Doctor in Philosophy
by
Guanqun Gai

Feburary 2017

Abstract

Gust interaction is a crucial design consideration for civil aircraft. A gust disturbance is defined as any air velocity component normal to the flight path. Gust interactions can rapidly change the aerodynamic forces acting on a wing and in turn the loads on the aircraft. Indeed, during this interaction, the structure of the aircraft may experience significant dynamic loading. It is therefore desirable to utilise gust load alleviation systems in aircraft design. This thesis investigates the influence of nonlinear structural behaviour in aeroelastic systems for gust load alleviation. In conjunction to the study of nonlinearities in structures, numerical methods for the fast prediction of stability and dynamic response for the nonlinear aeroelastic systems are required. To this end, this thesis investigates the nonlinear model order reduction framework based on eigenmode decomposition.

The nonlinear model reduction approach based on eigenmode decomposition is formulated and extended to include expansion terms up to fifth order such that higher-order nonlinear behaviour of a physical system can be captured. The method is first applied to a two degree-of-freedom pitch-plunge aerofoil structural model in unsteady incompressible flow. Structural stiffness nonlinearity is introduced as a fifth-order polynomial, while the aerodynamics follow linear theory. It is demonstrated that the reduced-order model is capable of accurately capturing the nonlinear aeroelastic behaviour arising from gust excitation. Furthermore, an analysis of the computational cost associated with constructing such reduced-order model and its applicability to more complex aeroelastic problems is provided.

The model reduction approach is then extended for a full-scale passenger aircraft exhibiting geometric structural nonlinearity. A structured approach to identify the dominant modes required to construct an accurate reduced-order model for such nonlinear aeroelastic system is presented. The effect of structural nonlinearities are studied through time domain gust response calculations and the reduced order model results are compared against the full-order reference solution. It is demonstrated that both the linear and nonlinear reduced-order models are capable of accurately predicting the dynamic gust response of aircraft structures while achieving significant reduction in system size.

Acknowledgements

I would like to acknowledge my supervisors Dr Sebastian Timme and Professor Ken Badcock for their assistance and support. I particularly wish to thank Dr Sebastian Timme who is a great mentor and without whom I would certainly have been lost. His ideas and suggestions to this work are invaluable and much appreciated.

Thanks also to the other members of the Computational Fluid Dynamics Laboratory at the University of Liverpool, both past and present, with special thanks to Professor Ken Badcock for his continued support.

Last, but not least, my family, shall not be forgotten for their support and patience.

The work was supported by an Engineering and Physical Sciences Research Council (EPSRC) Industrial CASE Studentship award and sponsored by Airbus in the UK.

Declaration

I confirm that the thesis is my own work, that I have not presented anyone else's work as my own and that full and appropriate acknowledgement has been given where reference has been made to the work of others.

Guanqun Gai
Feburary 2017

List of Publications

Gai, G., Timme, S. and Badcock, K. J., "An Assessment of Load Reduction of Nonlinear Aircraft Structures Using Reduced Order Model," Presented at the DiPaRT - Loads and Aeroelastics 2016 Annual Meeting at CFMS, Bristol, United Kingdom, 2016.

Gai, G., Timme, S. and Badcock, K. J., "Reduced-Order Modelling of Nonlinear Aircraft Structures," Presented at the Royal Aeronautical Society (RAeS) Applied Aerodynamics Conference 2016, Bristol, United Kingdom, 2016.

Gai, G. and Timme, S., "Nonlinear Reduced-Order Modelling for Limit-Cycle Oscillation Analysis," *Nonlinear Dynamics*, Vol. 84, No. 2, 2016, pp. 991–1009.

Gai, G. and Timme, S., "Nonlinear Model Reduction of Aeroelastic Systems with Discrete and Geometric Structural Nonlinearity for Gust Response Analysis," Presented at the DiPaRT - Loads and Aeroelastics 2014 Annual Meeting at CFMS, Bristol, United Kingdom, 2014.

Tantaroudas, N. D., Da Ronch, A., Gai, G. and Badcock, K. J., "An Adaptive Aeroelastic Control Approach using Non Linear Reduced Order Models," *AIAA Paper 2014–2590*, Presented at the 14th AIAA Aviation Technology, Integration, and Operations Conference, Atlanta, Georgia, 2014.

Table of Contents

List of Figures

List of Tables

List of Symbols

A	= Jacobian matrix
A_{ff}	= matrix relating fluid unknowns to their first time derivatives
A_{fx}	= coupling matrix relation fluid equations to structural degrees-of-freedom
A_L	= Jacobian matrix for the aerofoil system
A_N	= nonlinear Jacobian matrix
a_h	= non-dimensional distance from mid-chord to elastic axis
$\boldsymbol{\mathcal{B}}$	= multilinear vector function of second order derivatives
B_c	= coupling matrix relating control inputs to the aerodynamic forces
B_g	= vector relating gust disturbance to the aerodynamic forces
b	= semichord
$\boldsymbol{\mathcal{C}}$	= multilinear vector function of third order derivatives
C	= structural damping matrix
C_a	= finite element aerodynamic damping matrix
C_s	= finite element structural damping matrix
$C_L, C_{M\alpha}$	= lift and pitch moment coefficients about elastic axis
$C_{M\delta}$	= moment coefficient about flap hinge
$\tilde{C}$	= total damping matrix
C_α, C_h	= damping coefficients in pitch and plunge about elastic axis
C_δ	= damping in flap deflection about hinge
c_h	= non-dimensional distance from mid-chord to flap hinge
$\boldsymbol{\mathcal{D}}$	= multilinear vector function of fourth order derivatives
D	= viscous damping force
D_a	= coupling matrix relating aerodynamic states to the aerodynamic forces
D_f	= coupling matrix relating the structural equations to the aerodynamic states
$\boldsymbol{\mathcal{E}}$	= multilinear vector function of fifth order derivatives
$\boldsymbol{F}$	= all higher order derivatives with respect to the system states
$\boldsymbol{F}_A$	= aerodynamic force vector
$\boldsymbol{f}_a$	= vector of aerodynamic forces influenced purely by initial conditions
$\boldsymbol{f}_e$	= vector of any externally applied forces or moments
$\boldsymbol{f}_g$	= vector of external gust disturbance
f_α, f_h, f_δ	= nonlinear spring polynomials up to fifth order

$f_\alpha, f_\xi, f_\delta$ = nonlinear spring polynomials after non-dimensionalisation
H_δ = applied moment about flap hinge
$\bar{H}_\delta$ = non-dimensionalised flap hinge moment
h = physical plunge deformation positive down
I = identity matrix
I_α = second moment of inertia of aerofoil about elastic axis
I_δ = second moment of inertia of flap about hinge axis
K = structural stiffness matrix
K_a = finite element aerodynamic stiffness matrix
K_s = finite element structural stiffness matrix
$\tilde{K}$ = total stiffness matrix
K_α, K_h = stiffness in pitch and plunge about elastic axis
K_δ = stiffness in flap deflection about hinge
K_η, C_η = modal stiffness and damping matrices
$\boldsymbol{k}_N$ = nonlinear vector arising from polynomial stiffness
$\mathcal{L}$ = the Lagrangian
L, M_α = lift and pitch moment about elastic axis
M = structural mass matrix
M_t = tangent mass matrix
M_a = finite element aerodynamic mass matrix
M_s = finite element structural mass matrix
$\tilde{M}$ = total mass matrix
M_δ = flap hinge moment about hinge axis
m = aerofoil-flap mass
O = zero matrix
$\boldsymbol{Q}_{\text{ext}}$ = vector of external forces
$\boldsymbol{Q}_{\text{gyr}}$ = vector of gyroscopic forces
$\boldsymbol{Q}_{\text{stiff}}$ = vector of elastic forces
Q_i = generalised external forces
q_i = generalised coordinates
$\boldsymbol{R}$ = (nonlinear) residual vector
r_α = radius of gyration of the aerofoil-flap system about elastic axis
r_δ = reduced radius of gyration of the flap
S_α = static moment of inertia of aerofoil about elastic axis
S_δ = static moment of inertia of aerofoil about flap hinge
T = transformation matrix
T_{KE} = total kinetic energy of system
t = physical time
U = freestream velocity
$\bar{u}$ = reduced velocity

V = total potential energy of system

$\boldsymbol{W}$ = n-dimensional state space vector for an aeroelastic system

$\boldsymbol{W}_f$ = aerofoil augmented aerodynamic states

$\boldsymbol{w}_f$ = vector of fluid states

$\boldsymbol{W}_s$ = vector of structural states

$w_{0.75}$ = non-dimensional downwash at three-quarter chord

$\boldsymbol{X}_s$ = aerofoil structural degrees-of-freedom

$\boldsymbol{x}$ = physical degrees-of-freedom of a structural model

$\boldsymbol{x}_e$ = vector of beam nodal deformation displacements and rotations

$\boldsymbol{x}_r$ = vector of beam rigid-body displacements and rotations

x_α = non-dimensional offset of aerofoil-flap centre of gravity from elastic axis

x_δ = reduced aerofoil-flap centre of gravity from flap hinge

$\boldsymbol{z}$ = complex state-space vector of the reduced order system

α = physical pitch angle positive counter clockwise

$\beta_{\alpha 3}, \beta_{\alpha 5}$ = nonlinear stiffness coefficients in pitch

$\beta_{\delta 3}, \beta_{\delta 5}$ = nonlinear stiffness coefficients in flap

$\beta_{\xi 3}, \beta_{\xi 5}$ = nonlinear stiffness coefficients in plunge

δ = flap deflection angle positive clockwise

$\boldsymbol{\zeta}$ = vector of quaternion parameters

$\zeta_h, \zeta_\alpha, \zeta_\delta$ = damping ratios in plunge, pitch and flap

$\boldsymbol{\eta}$ = finite number of m modal amplitudes

$\boldsymbol{\Theta}$ = vector of independ ent system parameters

λ = eigenvalue

μ = mass ratio

Ξ = matrix with ‘mass normalised structural modes

ξ = non-dimensional plunge

τ = non-dimensional time

$\boldsymbol{\Phi}$ = right modal matrix

Φ_k = the Küsser function

Φ_w = the Wagner function

$\boldsymbol{\phi}$ = right eigenvector

$\boldsymbol{\Psi}$ = left modal matrix

$\boldsymbol{\psi}$ = left eigenvector

Ω = quaternion matrix

ω_h = uncoupled natural frequency in plunge

$\omega_x, \omega_y, \omega_z$ = angular velocity vector components

ω_α = uncoupled natural frequency in pitch

ω_δ = uncoupled natural frequency in flap

$\bar{\omega}_1$ = uncoupled natural frequency ratio plunge/pitch

$\bar{\omega}_2$ = uncoupled natural frequency ratio flap/pitch

List of Acronyms

CFD	= computational fluid dynamics
DLM	= doublet-lattice method
FFAST	= future fast aeroelastic simulation technologies
HALE	= high-altitude long-endurance
LCO	= limit-cycle oscillation
POD	= proper orthogonal decomposition
ROM	= reduced order model

Chapter 1

Introduction

Gust interaction is a crucial design consideration in aircraft aeroelasticity. A gust disturbance, defined as any air velocity component normal to the flight path, changes the effective angle of attack of the lifting surfaces. This in turn rapidly changes the aerodynamic forces acting on the lifting surfaces which translates onto the rest of the body. During this interaction, the structure of the aircraft may experience significant loading. This is particularly true for highly flexible structures exhibiting large deformations and changes in their geometry, which would in turn affect the aerodynamic loads acting upon the structure. The inherent problem posed by gust phenomena, thus, is one of safety, and ensuring an acceptable gust response is part of the requirements of the airworthiness regulations [1].

It is therefore desirable to utilise gust load alleviation systems in aircraft design. Traditionally and up till now, gust load alleviation employs active control systems which changes the wing's control surface deflection angle to counteract the effect of increasing aerodynamic loads. Typically, this takes the form of a closed-loop control law which relates the measured gust response to a control surface deflection input. This adds significant complexity to flight control systems. In particular, to safeguard against system failures system redundancy must be introduced, which leads to weight penalty. The possible alternative to the actively controlled gust alleviation approach is to use passive methods relying on nonlinear structural behaviour.

The main focus of this work is the assessment of novel concepts which intentionally introduce structural nonlinearity into the wing for gust load alleviation. It is important to stress that, while passive nonlinear devices add weight, an overall weight reduction can be expected. There are two distinct challenges to be addressed. First, the concepts for introducing nonlinearity into structural configurations must be explored. Secondly, in conjuction to this, numerical solutions for the fast and efficient prediction of stability and dynamic response for nonlinear aeroelastic systems are required. Consequently, nonlinear aeroelastic modelling plays a crucial and central role in this work. The following literature survey aims to briefly summarise studies in which structural nonlinearity

has been intentionally exploited for benefits. It then moves on to describe recent developments in the modelling of nonlinear aeroelasticity. The driving force in literature is currently focused on the high-altitude long-endurance (HALE) aircraft configurations, however, due to composite materials and novel configurations, civil aircraft can potentially benefit in the future.

1.1 Designed Structural Nonlinearities

The intentional implementation of structural nonlinearity as a design benefit is still largely unexplored. Investigations which have been published almost exclusively fall into two categories: active aeroelastic tailoring and energy harvesting.

Sousa et al. [2] explored the effect of combined structural nonlinearities in vibrating aeroelastic systems for the enhancement of piezoelectric energy generation. Their study presents both theoretical modelling and experimental test of a pitch-plunge aerofoil with piezoelectric coupling in the plunge degree-of-freedom. Nonlinearities in the form of freeplay and cubic stiffness are introduced into the pitch degree-of-freedom. A state-space model is formulated with unsteady aerodynamics theory based on Wagner's indicial function. Comparison between the linear model and the freeplay model at the onset of limit-cycle oscillation (LCO) showed an increase of more than 100% in voltage gain.

Kota [3] studied two concepts which allow for the active variation of torsional constant and the axial shear stiffness of the wing box. In one approach, the variable torsion stiffness is achieved by a mechanism which changed the lateral location of the front and rear webs. The advantage of this concept is that the bending stiffness is independent with respect to the lateral position of the webs. The variable shear stiffness concept consists of two flanges connected by inclined cross-pieces; by connecting and disconnecting the cross-pieces via the means of hydraulics or electrical actuation, the shear stiffness can be varied. Static finite element analysis on the first concept demonstrated a variation in torsional stiffness of up to 20%. No dynamic response analysis was performed however.

Chen et al. [4] proposed the Variable Stiffness Spar concept where a segmented spar is interconnected by articulated joints at the wing ribs. Electrical actuation rotates the spar segments through and up to an angle of 90 degrees. While the spar segments are in the horizontal orientation the wing box exhibits lower torsional stiffness as the Variable Stiffness Spar is 'uncoupled'. When the spars are rotated they lock and join increasing overall torsional stiffness of the wingbox. Numerical studies with the inclusion of the Variable Stiffness Spar in the F/A-18 wingbox show improved aircraft roll performance in transonic flight.

Cooper [5] presented two concepts of adaptive internal structures utilising active control of the wing's internal spar orientation and location. In the first concept, the

wing box consists of the standard front and rear spar but also in addition a central moveable spar. In the second concept, the wingbox consists only of the front and rear spars which can, in addition, rotate. Variations of the flutter speed with respect to the spar orientation are evaluated and presented numerically.

All of the above methods utilises active actuation of internal structural elements to change the static structual properties for the purpose of aeroelastic tailoring and flight optimization as well as piezoelectric energy generation. In respect to gust alleviation these methods are unsatisfactory. Gust interference is often sudden and it is impractical, for example, to actively change the orientation of a wing spar during the gust disturbance. In addition, an actively controlled system such the ones described in this section presents the same disadvantages as the current gust alleviation system using active control. Complicated flight control systems are required for many internal components such that hydraulic actuators results in a weight penalty. It is therefore necessary that the structural nonlinearity is inherent in the structural setup of the wing and performs through passive reaction-based mechanism.

1.2 Aircraft Aeroelastic Modelling

The central focus of this work is on the modelling of aeroelasticity and fluid-structure interaction. In the view of introducing passive nonlinear structural behaviour into a wing which changes its inherent physical behaviour, the goal is to be able to predict the resulting aeroelastic responses and stability properties. Traditionally, for conventional aircraft, linear analysis has been demonstrated to be very successful for aeroelastic evaluations as the structural models are assumed to be fully linear. However, with structural nonlinearities and their related behaviours, nonlinear consideration in analysis becomes increasingly important.

A comprehensive review of general aeroelasticity is given by Livne and Weisshaar [6] where a detailed review of the key developments of aeroelasticity for unconventional aircraft over the past 100 years is discussed. Attention is drawn to the importance of inclusion of rigid body degrees-of-freedom in aeroelastic analysis. The impact of nonlinearities in aeroelasticity such as geometric and freeplay on the flight dynamic response is discussed. For instance, lightweight aircraft with very high aspect ratio wings are suspectible to nonlinear aeroelastic behaviour. Typically, with very large deformations geometric nonlinearities may affect the effective stiffness of the wing which consequently lead to variations of the structural natural frequencies under load. This can result in LCO involving coupled rigid-body and elastic motion of the complete vehicle.

A summary of nonlinear aeroelasticity phenomena is provided by Dowell and Tang [7] where broad discussions are provided on several types of aeroelastic nonlin-

earities including control surface freeplay of a two dimensional aerofoil and geometrical nonlinearities associated with large beam deformations.

A detailed review of sources of inherent structural nonlinearities present in aeroelastic systems is attributed to Lee et al. [8]. In the broadest sense, aeroelastic structural nonlinearities can be classified into two categories: distributed and concentrated. Distributed structural nonlinearity is associated with deformations which affect the entire structure, for example, nonlinearity arising from the change in overall geometry or configuration of the structure. This is true for very flexible aircrafts exhibiting large deformation where the assumptions of the theory of linear structural analysis no longer apply. Concentrated nonlinearity occurs locally and can be found, for example, in the hinge of a control surface such as a flap or aileron.

One type of such concentrated nonlinearity is cubic hardening stiffness. This nonlinearity typically represents aerofoil sections experiencing wing twist where the torsional stiffness increases with the twist angle. A softening nonlinearity, whereby the torsional stiffness decreases with increasing deformation angle can approximate a torsionally buckled structure. Another type of nonlinearity occurs in control surface hinges where backlash often produces a flat-spot of zero restoring force in the force-displacement curve. Physically, for a small displacement gap, for example, between minus and plus one degree flap deflection, the flap hinge offers no resistance force. This type of nonlinearity is commonly referred to as control surface freeplay. The flat spot can also be replaced with a linear profile in the force-displacement curve. This mathematically represents the case if the hinge spring has preload and the resulting profile is referred to as bilinear stiffness. More examples of concentrated structural nonlinearity are discussed by Lee et al. [8].

In terms of aerodynamics, nonlinearities can arise in the transonic regime where inviscid, incompressible theory no longer applies. One such nonlinearity can be attributed to the formation of shock waves. The unsteady forces generated by shock motion can destabilize an aerofoil and consequently lower the flutter speed. Such fluid-structure interaction is, in general, highly complex. Computational fluid dynamics (CFD) must replace linear aerodynamic theories to capture such phenomena. Therefore it is important to consider and establish accurate and efficient modelling approaches to address nonlinearities arising from the fluid.

1.2.1 Structural Modelling

One of the earliest works on modelling nonlinear aeroelasticity is attributed to van Schoor and von Flotow [9]. They presented an aeroelastic modelling and analysis process for the 'Michelob Light Eagle' human powered aircraft which functioned as the prototype to the 'Daedalus' aircraft. The model formulation coupled a standard finite element structural model with unsteady strip aerodynamics. The nonlinearity

associated with flexible structure is dealt with by linearising the governing equations about nonlinear equilibrium points. The study highlighted the important effect of flight speed and altitude upon the structural dynamic frequencies and the importance of the inclusion of aeroelastic effect in flight dynamic modelling as significant changes to the rigid-body modes were demonstrated when structural flexibility is included into the flight dynamics model.

Later, Patil et al. [10] presented a complete aeroelastic formulation for a HALE type aircraft. Of particular interest is the construction of the structural dynamics model, which utilised the existing nonlinear beam framework developed by Hodges [11] and provides accurate formulation of geometrically exact beam dynamics undergoing large deformations. The results, primarly flutter speed, have been validated against the Goland wing [12].

Drela [13] developed an analysis tool integrating structural, aerodynamic, and control law aspects for conceptual aircraft design. The model relies upon an isotropic geometrically nonlinear beam formulation and lifting line aerodynamics.

Furthering the analysis scope of nonlinear aeroelasticity, Cesnik and Brown [14] introduced a strain-based finite element beam framework to capture both the effect of geometrical nonlinearity and anisotropic piezoelectric composites for a HALE type aircraft. The aim was to model the impact of roll control using these piezoelectric devices. In this study, the fuselage is treated as a rigid-body constrained only to roll motion. The unsteady aerodynamic model coupled to the structural model is Peters' finite state theory [15]. Comparison between roll actuation from conventional 20 degree aileron deflection and piezoelectric demonstrated up to 60% improvement on roll authority.

Extension upon this work by Cesnik and Su [16] added flexibility to all aspect of the aircraft. The fuselage and tail plane are modelled by the same nonlinear beam model. Two baseline aircraft configurations were presented; one single-wing and one joined-wing. The models are once again constrained to motion only in roll. Numerical results were presented for flutter analysis and roll performance. Later, Su and Cesnik [17] incorporated the effect of discrete gust disturbance and skin wrinkling into their aeroelastic flying wing model.

More recently several works have been presented concerning the combination of geometrical structural nonlinearity, flight dynamics, and unsteady aerodynamics for flying wings. Patil and Hodges [18] presented a study coupling the nonlinear structural dynamics effect with large motion flight dynamics. The flying wing is constructed using a one dimensional nonlinear beam model. Once again, the unsteady aerodynamics are modelled by Peters' finite state theory. Later, Patil and Taylor [19] evaluated the effect of various gust models including both discrete gust and continuous turbulence.

Palacios and Cesnik [20] developed a framework to study the nonlinear aeroelastic behaviour of slender wings in compressible flow. The flow is simulated using three

dimensional Euler equations and is coupled with a structural modeling framework constructed from a combined one and two dimensional model. The one dimensional model is a geometrically nonlinear beam model and captures the nature of slender wing structures with a single dominant spatial direction. The two dimensional model allows the evaluations of cross-sectional deformations, in particular, effective aerofoil camber changes due to cross-sectional warping. Due to the extremely large size of the coupled nonlinear structure - nonlinear aerodynamic problem only static simulation results are presented.

Garcia [21] coupled a geometrically nonlinear finite element beam model with full Navier-Stokes flow solver. The test case presented is a cantilevered swept wing model. Significant differences in the static solution is shown between the linear and nonlinear structural models.

Shearer and Cesnik [22] presented a complete low-order model for a very flexible aircraft coupling structural and flight dynamics. The six degree-of-freedom reference point of the aircraft is coupled with geometrically nonlinear structural dynamic response. The complete structural equations are combined with Peters' finite state aerodynamics. The final aeroelastic equations of motion couple first and second order differential equations and are integrated using an modified implicit Newmark-β method [23]. Numerical studies were performed on a test case representative of a twin-tailed HALE-type aircraft. Results show a comparison of the dynamic response from purely nonlinear rigid-body equations with coupled nonlinear rigid-body and structural dynamics. It was concluded that a coupled model is necessary for capturing accurately asymmetrical flight manoeuvres while linearised analysis can be sufficient for symmetric flight manoeuvres.

Murua et al. [24] investigated the coupled aeroleasticity and flight dynamic effect of very flexible aircraft. The structural model uses a displacement-based geometrically nonlinear beam formulation and this is coupled with unsteady vortex lattice aerodynamic theory. A series of open-loop transient response calculations are presented along with flutter analysis. Cook et al. [25] extended upon this beam model to replace the aerodynamic formulation with the two dimensional unsteady theory of Leishmann [26]. The focus of this study is for gust alleviation via control.

1.2.2 Aerodynamics and Aeroelasticity Modelling

Aside from the modelling of structural nonlinearity, the other key aspect of aeroelastic modelling is the aerodynamics. This will play an important role in both gust response calculations, and also stability calculations for the flutter speed.

In the calculation of the flutter speed, conventional approaches accepted on an industrial standard are the k and $p-k$ methods. Commercial finite-flement (FE) software packages such as NASTRAN [27] readily provide such solution methods to the flutter equation. However, these methods rely on the assumption of incompressible

inviscid aerodynamics in the frequency domain which becomes inapplicable for flight in the transonic regime.

The stability characteristics of an aeroelastic system can be determined by time domain simulations. To accurately predict the flutter speed in the transonic flight regime the incorporation of CFD is necessary. However, the incurred computational cost for such process to evaluate entire parameter spaces for the critical flight condition is very high. This is because utilising such methodology requires the action of repeatedly solving systems with millions of degrees-of-freedom which is particularly important from an industrial perspective. Consequently, reducing the cost of such analysis procedure becomes a important goal of research investigation.

One approach to overcome the high computational cost utilises theory of dynamical systems. Instability is determined by evaluating the Hopf bifurcation which commonly relate, for aeroelastic systems, to the onset of flutter or LCO. A Hopf bifurcation refers to the case where a pair of complex conjugate eigenvalues crosses the imaginary axis with respect to a change in an independent system parameter. The independent system parameter for the case of aeroelastic systems can be, for example in the case of flutter speed calculations, the free stream velocity. The method of determining the Hopf bifurcation is aimed to provide a faster way to evaluate system stability over traditional time marching simulations.

The first attempt in this approach at transonic flow conditions is attributed to Morton and Beran [28]. In their study, a two degree-of-freedom aerofoil is coupled with the Euler equations. The direct calculation of the Hopf point is demonstrated to be fast and efficient and are consistent with time integration methods. Results are also presented to show the computed flutter boundary of the aerofoil with respect to the Mach number. Badcock et al. [29] extended upon this method to utilise a sparse matrix solver. In particular, the test case in this paper is a symmetric aerofoil in transonic flow. Two major difficulties were addressed in this approach: the construction of the Jacobian matrix and the solution of the linear system in the Newton iteration for the convergence to the eigen-solution. The linear system is large, coupling a CFD model to structural dynamics model, and consequently, convergence problems associated with applying a direct solver to this large linear system were resolved by using an iterative sparse linear solver. Application of this approach on a symmetric NACA0012 aerofoil was shown to trace the flutter boundaries across 25 Mach numbers at a time cost of three to four time marching simulations.

Later, Badcock et al. [30] extended upon this work to demonstrate its capability to trace out the entire flutter boundary of the AGARD 445.6 wing. The additional difficulties addressed in this work include deforming geometry of the three dimensional wing, dealing with the structural equations in modal space, dealing with the relationship between non-matching fluid and structural grids, and finally a significant increase in problem size. The issue of the mismatch between the structual and aerodynamic grid

points is addressed through the constant-volume-tetrahedron transformation method. The deformation of the wing geometry means the fluid mesh must also undergo deformation which is achieved by transfinite interpolation. Results show that the flutter boundary across eight Mach numbers can be traced out in a time of less than half of a single time marching simulation. It is also demonstrated that despite the increase in problem size the number iterations required by the linear solver has not increased. Hence it is concluded that the performance obtained from the aerofoil case is preserved in the wing case.

Badcock et al. [31] presented a study on the evaluation of fast prediction methods for the onset of wing rock. Several proposed fast methods are tested for the evaluation of the wing rock onset angle and compared with full time domain simulation result. These are direct stability calculation by evaluating the Hopf bifurcation, direct inverse power method, linearised time domain method and also reduced system by proper orthogonal decomposition approach. The model test case used here is a 80 degree delta-wing. A consistent onset angle result of 24.3 degrees is obtained across all the methods and relative CPU time for the different methods with respect to a single steady state calculation is given.

Improving upon the method developed, Badcock and Woodgate [32] presented the development of the Schur complement method. The approach uses a reformulation of the linearised eigenvalue problem that exploits the Schur complement. This allows for the system Jacobian to be decoupled into its constitutive parts resulting in a nonlinear eigenvalue problem of smaller dimension. In essence, the coupled aeroelastic system is restructured as a modified structural eigenvalue problem with the interaction term that depends on both structural and fluid parameters. The evaluation of this term involves the highest computational cost because it requires inverse operations on high dimensional CFD matrices. Four test cases are presented in this study for validation of method: the Goland wing model [12], the supersonic transport model for the evaluation control surface buzz, the multidisciplinary design optimisation wing and finally the Open Source Fighter. For the Goland wing model, comparison against NASTRAN showed excellent agreement for the eigenvalue mode traces which at the same time provided physical insight into the flutter mechanisms associated with each mode. Similar mode tracing results and corresponding computational time are reported for the remaining test cases.

Timme et al. [33] applied the inexact Lyapunov inverse iteration method for the analysis of aeroelastic stability problems via Hopf bifurcations using CFD. The inexact Lyapunov inverse iteration approach allows for the estimate of the critical eigensolution and the corresponding independent parameter using only information of the equilibrium point provided it is within the vicinity of the instability onset. The test cases includes a two degree-of-freedom aerofoil and a Goland wing.

1.2.3 Approaches to Reduced-Order Modelling

Alternatively reduced-order models can be constructed. This approach extracts the dominant dynamics of an aeroelastic system to form a lower-dimensional model while preserving accurate prediction of the full-order model.

One type of model reduction is based on the nonlinear system identification technique of the Volterra theory. This method is based on defining a transfer function in either the time or frequency domain to model the input-output relationship of the dynamic system under consideration. This method allows for the representation of an arbitrary system input as a series summation of integrals of Volterra kernels. A detailed summary of the method can be found in the work of Silva [34].

Another method is proper orthogonal decomposition (POD) an overview of which can be found in the review presented by Lucia et al. [35]. This approach uses snapshots or samples of the full-order system's dynamical response to form a mode basis for the construction of the reduced-order model. This is done by projecting the full-order system onto this mode basis. Typically the snapshots are taken during a dynamic history of interest where critical information can be captured relating to the dominant system dynamics.

Hall et al. [36] presented a method for the construction of reduced-order models based on proper orthogonal decomposition for transonic flow problems in the frequency domain. The POD modes here are calculated at discrete frequencies and 20 modes were used. The numerical test cases used are aerofoils in two dimensional flow. Good agreement in the eigenspectrum between the full and reduced system was demonstrated.

A different method to construct reduced-order models relies on eigenmode decomposition. The general approach of this method also involves projecting the full-order system. Here, the projection is made onto a finite number of eigenmodes at a point of interest. An application of this method based on the centre manifold theory was investigated to compute LCO response in transonic flow by Woodgate and Badcock [37]. In this appoach, the full-order system is projected onto a single critical eigenvector evaluated at the flutter point. The test case model used is the Goland wing and excellent agreement is demonstrated between the full-order and reduced-order model.

The impact of structural parameter variability due to uncertainty within this centre manifold model order reduction framework was studied by Badcock et al. [38]. The important additional theoretical step in this approach to model structural uncertainty is to add an additional uncertainty parameter in the Taylor series expansion. The method is applied to a pitch-plunge aerofoil with cubic spring and also a Goland wing with introduced local nonlinearity for a tip store.

Da Ronch et al. [39] presented a systematic approach for the model reduction of fluid-structure-flight models and subsequent control application based on the reduced model. The model order reduction approach exploits the eigenmode decomposition of

the coupled system's Jacobian matrix in conjuction with the Taylor expansion of the nonlinear full-order residual. By projecting the full-order system upon the eigenmode basis, a smaller set of equations governing the dominant dynamics of the system can be constructed. The smaller dimensional model also allows for the application of control laws for gust load alleviation. Two test cases were presented in this study which are a sectional two dimensional aerofoil with degrees-of-freedom in pitch and plunge and also a fully three dimensional unmanned aerial vehicle modelled using nonlinear geometrically exact beam equations. In addition, two gust models are utilised in the test cases. These are the standardised discrete 1-cosine profile and also continuous turbulence, whereby the history is generated using Von Kármán spectrum. The paper presents a clear formulation of the reduction approach and the results show in general an excellent agreement between the reduced-order model and the reference full-order solution.

Da Ronch et al. [40] then extended upon this work to include model order reduction for gust loads. Here, the novelty introduced is the representation of the gust influence within the reduced-order model by introducing a specific gust term in the Taylor expansion of the residual. This allows for an arbitrary number of different gust profiles to be applied to the resulting reduced-order model without the need to regenerate the model itself. Results are presented for aerofoil and wing models to demonstrate the capability of the method.

Timme et al. [41] presented a unified approach for the modeling of CFD based flutter and gust response calculation for realistic aircraft configurations based on this model order reduction framework. In this work, the well-established industrial CFD code DLR-TAU is used for the calculation of aerodynamic influence. Results are presented for two test cases: the Goland wing and the XRF1 aircraft model which is a representation of a wide-body passenger aircraft.

1.3 Overview of Work and Outline of Thesis

The aim of the work is to develop and implement nonlinear aeroelastic simulation tools for analysing aeroelastic systems with structural nonlinearity.

The central framework introduced here is the approach of nonlinear model order reduction by eigenmode decomposition. Chapter 2 presents the theoretical formulation of the model order reduction method within the context of aeroelastic systems.

Chapter 3 introduces the construction of the nonlinear aeroelastic system of a three degree-of-freedom pitch-plunge aerofoil with trailing edge flap. The structural model is nonlinear in that the stiffness corresponding to each degree-of-freedom is represented in polynomial form up to the quintic order. Stability analysis is performed for the determination of the linear flutter speed. Freeplay is introduced into pitch degree-of-freedom and time domain response is simulated for further model validation. Gust

response simulations are presented to investigate the linear structural response and this is demonstrated in conjuction with linear reduced-order model. Comparisons are made between the responses of the full and reduced-order model. Lastly, the effect of structural nonlinearity in polynomial form is examined. Both cubic and quintic-order nonlinearity are introduced into the pitch degree-of-freedom and the corresponding reduced-order models are examined. Specifically, the limit-cycle response behaviour of the aerofoil is studied in detail. The novelty here is the application of higher-order reduced-order models (ROM) to represent higher-order structural nonlinearity. It is critical that the ROM accurately reproduces the associated LCO behaviour.

Chapter 4 introduces the geometrically exact beam model [42,43] which accounts for large deformations and geometrical structural nonlinearity. Several aeroelastic models are constructed using the beam framework with increasing system and complexity. The first is a flexible cantilever beam. This beam is coupled with unsteady potential strip aerodynamics. The aerodynamic model is coupled by assigning aerofoil sections to each finite element nodal point along the beam span and therefore representative of a slender aircraft wing. Gust response simulation is calculated and compared against an identical model constructed in NASTRAN. The second model aims to include rigid body flight dynamics effects. The beam model is rigid and unrestrained in every degree-of-freedom such that it is free-flying. It is coupled with the same unsteady aerodynamics model. Results are presented to show both the free response of the rigid wing to an initial disturbance as well as a gust reponse to the standardised 1-cosine discrete gust. The final two models are full scale, large nonlinear aircraft structures based on the FFAST model for gust response simulation as well as the application of nonlinear model reduction. In regards to the nonlinear model reduction, a structured guideline is presented such that the dominant modes can always be identified to construct an accuracte reduced-order model. The novelty here is the representation of a large-scale civil aircraft industrial model using a geometrically nonlinear beam formulation. In addition, the application of reduced-order modelling is demonstrated for this large nonlinear structural system. In particular, attention is focused on choosing the important eigenmodes used for the basis such that the resulting ROM accurately represents the full-order system.

Chapter 5 concludes the thesis and suggests outlook and directions for future work. The analytical aeroelastic coefficients of the models studied in this thesis are given in complete detail in the appendices. In addition, the beam finite-element geometric properties of the FFAST model are given here as well.

Chapter 2

Nonlinear Model Reduction

This chapter describes the derivation of the model reduction framework based on eigenmode decomposition with the novel extension to include up to fifth-order terms in the Taylor expansion allowing, in principle, for the prediction of higher-order nonlinear dynamics. Specific attention is focused on expanding the reduced model about the system parameters. Linear and nonlinear versions of the formulations are discussed.

2.1 Full-Order Nonlinear Model

A typical aeroelastic model is generally given as a set of second-order ordinary differential equations with the standard structural mass, damping and stiffness matrices: M, C and K

$$M\ddot{\boldsymbol{x}} + C\dot{\boldsymbol{x}} + K\boldsymbol{x} = \boldsymbol{f}_a + \boldsymbol{f}_g \tag{2.1}$$

where $\boldsymbol{f}_a$ and $\boldsymbol{f}_g$ represent the general external forcing arising from aerodynamic influence and external disturbances, respectively. The aerodynamic repesentation is general and can be modelled by either linear theory or fully nonlinear computational fluid dynamics (CFD) models. The vector $\boldsymbol{x}$ denotes the physical degrees-of-freedom of the structural model and $\dot{(\,)}$ denotes derivative with respect to time. Specific structural models that align with this general representation are investigated in Chapters 3 and 4.

This fully coupled nonlinear model describing the dynamics of an aeroelastic system can be represented in first-order semi-discrete state-space form. Denote by $\boldsymbol{W}$ the n-dimensional state-space vector partitioned into structural states $\boldsymbol{W}_s$ and aerodynamic states $\boldsymbol{W}_f$. Here, $\boldsymbol{W}_s = \left[\boldsymbol{x}^T, \dot{\boldsymbol{x}}^T\right]^T$. Written as a set of first-order ordinary differential equations, the state-space equations are given as

$$\frac{\mathrm{d}\boldsymbol{W}}{\mathrm{d}t} = \boldsymbol{R}\left(\boldsymbol{W}, \boldsymbol{\Theta}\right) \tag{2.2}$$

where $\boldsymbol{R}$ is the nonlinear residual vector corresponding to the unknowns $\boldsymbol{W}$, while $\boldsymbol{\Theta}$ is a vector of independent system parameters. The system has a reference equilibrium

point $\boldsymbol{W}_0$ for given constants $\boldsymbol{\Theta}_0$ the solution of which can be obtained depending in the type of the system. For the idealised simple aerofoil model as presented in Chapter 3 the equilibrium point is trivial. Whereas, in the case of a complex large aircraft type structure as described in Section 4.2.4, the equilibrium point is obtained by trimming the aircraft through an iterative process. The residual vanishes with $\boldsymbol{R}(\boldsymbol{W}_0, \boldsymbol{\Theta}_0) = 0$ at this equilibrium point. If linear aerodynamics is used to model the fluid physics, the size of the system tends to be small. This is illustrated in the physical models as described in Sections 3.1 and 4.2.4. If the aerodynamic model is constructed using CFD, the vector of aerodynamic states $\boldsymbol{W}_f$ typically extends to a size in the order of millions. Equation (2.2) can be integrated in time in physical space directly using standard schemes of the Runge-Kutta family.

2.2 Physics Based Model Reduction Using Eigenmodes

Define $\boldsymbol{w} = \boldsymbol{W} - \boldsymbol{W}_0$ as the increment in the state-space vector with respect to an equilibrium solution. Define also $\boldsymbol{\theta} = \boldsymbol{\Theta} - \boldsymbol{\Theta}_0$ as the increment in the system's independent parameters with respect to the equilibrium values. The nonlinear residual in Eq. (2.2) can then be expanded in a multi-variate Taylor series about the reference equilibrium point with respect to the system states $\boldsymbol{W}$ and parameters $\boldsymbol{\Theta}$ as

$$\boldsymbol{R}(\boldsymbol{W}, \boldsymbol{\Theta}) = A\boldsymbol{w} + \boldsymbol{F}(\boldsymbol{w}) + \Big(\boldsymbol{R}_\Theta(\boldsymbol{W}_0, \boldsymbol{\Theta}_0) + A_\Theta \boldsymbol{w} + \boldsymbol{F}_\Theta(\boldsymbol{w})\Big)\boldsymbol{\theta} \tag{2.3}$$

where $A = \partial \boldsymbol{R}/\partial \boldsymbol{W}$ is the system Jacobian matrix and $\boldsymbol{F}$ represents all higher order derivatives in $\boldsymbol{W}$. Subscript Θ denotes differentiation with respect to it. While only first-order derivatives in $\boldsymbol{\Theta}$ are retained here for clarity, higher order derivatives are included as well in the subsequent discussion. Note that while the residual at the equilibrium is zero, its derivative with respect to the parameters is not in general.

The function $\boldsymbol{F}$ is explicitly written as

$$\boldsymbol{F}(\boldsymbol{w}) \approx \tfrac{1}{2!}\boldsymbol{\mathcal{B}}(\boldsymbol{w}, \boldsymbol{w}) + \tfrac{1}{3!}\boldsymbol{\mathcal{C}}(\boldsymbol{w}, \boldsymbol{w}, \boldsymbol{w}) + \tfrac{1}{4!}\boldsymbol{\mathcal{D}}(\boldsymbol{w}, \boldsymbol{w}, \boldsymbol{w}, \boldsymbol{w}) + \tfrac{1}{5!}\boldsymbol{\mathcal{E}}(\boldsymbol{w}, \boldsymbol{w}, \boldsymbol{w}, \boldsymbol{w}, \boldsymbol{w}) \tag{2.4}$$

where $\boldsymbol{\mathcal{B}}$ to $\boldsymbol{\mathcal{E}}$ are multilinear vector functions of higher order derivatives. Here functions up to fifth order with respect to the arguments $\boldsymbol{w}$ are retained. More specifically,

evaluated about the equilibrium point (indicated by subscript 0), these are

$$\begin{aligned}
\boldsymbol{\mathcal{B}}(\boldsymbol{x},\boldsymbol{y}) &= \sum_{j,k=1}^{n} \left.\frac{\partial^2 \boldsymbol{R}}{\partial W_j \partial W_k}\right|_0 x_j y_k \\
\boldsymbol{\mathcal{C}}(\boldsymbol{x},\boldsymbol{y},\boldsymbol{z}) &= \sum_{j,k,l=1}^{n} \left.\frac{\partial^3 \boldsymbol{R}}{\partial W_j \partial W_k \partial W_l}\right|_0 x_j y_k z_l \\
\boldsymbol{\mathcal{D}}(\boldsymbol{x},\boldsymbol{y},\boldsymbol{z},\boldsymbol{a}) &= \sum_{j,k,l,o=1}^{n} \left.\frac{\partial^4 \boldsymbol{R}}{\partial W_j \partial W_k \partial W_l \partial W_o}\right|_0 x_j y_k z_l a_o \\
\boldsymbol{\mathcal{E}}(\boldsymbol{x},\boldsymbol{y},\boldsymbol{z},\boldsymbol{a},\boldsymbol{b}) &= \sum_{j,k,l,o,p=1}^{n} \left.\frac{\partial^5 \boldsymbol{R}}{\partial W_j \partial W_k \partial W_l \partial W_o \partial W_p}\right|_0 x_j y_k z_l a_o b_p
\end{aligned} \tag{2.5}$$

Note that $\boldsymbol{\mathcal{B}}$ to $\boldsymbol{\mathcal{E}}$ are symmetric multilinear functions [44] with respect to their arguments. The multi-variate Taylor expansion of Eq. (2.3) is the starting point for the model reduction formulation described hereafter.

2.2.1 Multiple Modes Nonlinear Model Reduction

In the model reduction approach using multiple eigenmodes, the full-order system is projected onto a small basis of m eigenvectors of the Jacobian matrix A evaluated at the equilibrium point. The eigensolutions of the Jacobian matrix are complex-valued in general. Such eigensolutions exist, for example, as modes of structural vibration. In the case the aerodynamics is modelled using CFD, complex-valued fluid modes exist as well. Otherwise for linear aerodynamics, eigensolutions associated with the fluid unknowns are purely real-valued. Often, a suitable choice is then to retain lower frequency, weakly damped modes which are associated with large amplitudes and hence dominate the system dynamics.

The set of right eigenvectors $\boldsymbol{\phi}_i$ is obtained by solving

$$A\boldsymbol{\phi}_i = \lambda_i \boldsymbol{\phi}_i, \quad \text{for} \quad i = 1, \ldots, m \tag{2.6}$$

while the adjoint problem

$$A^H \boldsymbol{\psi}_i = \bar{\lambda}_i \boldsymbol{\psi}_i, \quad \text{for} \quad i = 1, \ldots, m \tag{2.7}$$

gives the set of left eigenvectors $\boldsymbol{\psi}_i$. The superscript H denotes the conjugate transpose (i.e. Hermitian). The right and left eigenvectors are used to form the corresponding modal matrices, denoted by Φ and Ψ,

$$\Phi = [\boldsymbol{\phi}_1, \ldots, \boldsymbol{\phi}_m], \quad \Psi = [\boldsymbol{\psi}_1, \ldots, \boldsymbol{\psi}_m], \quad \Phi, \Psi \in \mathbb{C}^{n \times m} \tag{2.8}$$

Note, for each eigenvector only one of the complex conjugate pairs is included in the modal matrices and it is typically the one with positive frequency. It is convenient to scale the eigenvectors to satisfy the biorthonormality conditions,

$$\Psi^H \Phi = I, \quad \Psi^H \bar{\Phi} = O, \quad I, O \in \mathbb{R}^{m \times m} \tag{2.9}$$

where matrices I and O are the identity matrix and a zero matrix, respectively. The biorthonormality conditions also provide the following results

$$\Psi^H A \Phi = \Lambda, \quad \Psi^H A \bar{\Phi} = O \tag{2.10}$$

where $\Lambda \in \mathbb{C}^{m \times m}$ is a diagonal matrix containing the eigenvalues.[1]

The vector $\boldsymbol{w}$ is represented by a small set of m eigenvectors using the following coordinate transformation

$$\boldsymbol{w} = \Phi \boldsymbol{z} + \bar{\Phi} \bar{\boldsymbol{z}} \tag{2.11}$$

where $\boldsymbol{z} \in \mathbb{C}^m$ is the state-space vector governing the dynamics of the reduced order nonlinear system. Essentially, $\boldsymbol{w}$ is represented as a linear combination of right eigenvectors with $\boldsymbol{z}$ as the time-dependent amplitude. The nonlinear ROM is then formed by substitution. Premultiplying each term by the Hermitian of the left modal matrix, the nonlinear reduced formulation takes the form

$$\frac{\mathrm{d}\boldsymbol{z}}{\mathrm{d}t} = \Lambda \boldsymbol{z} + \Psi^H \boldsymbol{F}\big(\Phi \boldsymbol{z} + \bar{\Phi} \bar{\boldsymbol{z}}\big) + \Psi^H \Big(\boldsymbol{R}_\Theta + A_\Theta \Phi \boldsymbol{z} + A_\Theta \bar{\Phi} \bar{\boldsymbol{z}} + \boldsymbol{F}_\Theta \big(\Phi \boldsymbol{z} + \bar{\Phi} \bar{\boldsymbol{z}}\big) \Big) \boldsymbol{\theta} \tag{2.12}$$

Contained in function $\boldsymbol{F}$, the functions $\boldsymbol{\mathcal{B}}$ to $\boldsymbol{\mathcal{E}}$ depending on the state variables $\boldsymbol{w}$ have to be transformed as well to be written in terms of $\boldsymbol{z}$. The explicit evaluation of the functions $\boldsymbol{\mathcal{B}}$ to $\boldsymbol{\mathcal{E}}$ in Eq. (2.12) are given in Appendix A. Observe while the biorthonormality conditions of Eq. (2.10) hold true for the Jacobian matrix A, they do not apply to A_Θ. The evaluation of $\boldsymbol{F}_\Theta$ simply requires the terms $\boldsymbol{\mathcal{B}}_\Theta$ to $\boldsymbol{\mathcal{E}}_\Theta$ which means differentiating all the functions in Eq. (2.5) with respect to $\boldsymbol{\Theta}$. Once the equilibrium point and eigensolution are determined, the terms of the reduced formulation involving full-order operations only need to be calculated once and stored initially. Operations involved, when solving Eq. (2.12) for arbitrary parameter changes, scale with m rather than n.

[1] Note in the case of a real-valued eigensolution, the biorthonormality conditions can no longer be satisfied as $\boldsymbol{\phi} = \bar{\boldsymbol{\phi}}$. These eigenvectors are then scaled such that $\boldsymbol{\psi}^H \boldsymbol{\phi} = \frac{1}{2}$ giving $\boldsymbol{\psi}^H A \boldsymbol{\phi} = \frac{1}{2}\lambda$ which is convenient in order to use consistent notation when dealing both with real- and complex-valued modes.

Note a linear reduced order model (ROM) is formed by neglecting all the higher order terms of Eq. (2.12) giving

$$\frac{\mathrm{d}\boldsymbol{z}}{\mathrm{d}t} = \Lambda \boldsymbol{z} + \Psi^H \boldsymbol{R}_\Theta \boldsymbol{\theta} \tag{2.13}$$

Equations (2.12) and (2.13) can be integrated in time directly using complex arithmetic by standard Runge-Kutta schemes.

2.2.2 Critical Mode Nonlinear Model Reduction

A special case arises when a single critical mode is used as the basis with $m = 1$. The critical mode corresponds to a single pair of complex conjugate eigenvalues of the Jacobian matrix with vanishing real part, namely a Hopf bifurcation [44]. In this case, Eqs. (2.6) and (2.7) each reduce to a single eigenvalue problem and the evaluation of the vector functions as shown in Eq. (A.5) requires signifcantly fewers terms as all summations vanish. Similarly to the previous multiple modes case, this single eigenvector is scaled to satisfy biorthonormality conditions such that Eq. (2.10) is satisfied.

Denoting the critical eigenvector as $\boldsymbol{\phi}_c$ the vector $\boldsymbol{w}$ can now be represented in terms of this critical mode using the centre manifold theorem [44, 45]

$$\boldsymbol{w} = z\boldsymbol{\phi}_c + \bar{z}\bar{\boldsymbol{\phi}}_c + \boldsymbol{y} \tag{2.14}$$

the sum $z\boldsymbol{\phi}_c + \bar{z}\bar{\boldsymbol{\phi}}_c$ represents the component of the full-order solution which is governed by the space spanned by the critical eigenvector, while $\boldsymbol{y}$ represents the component which is not in the critical space with $\boldsymbol{\psi}_c^H \boldsymbol{y} = 0$.

The centre manifold theorem states that the dynamics of the full-order system are dominated by the critical space in the vicinity of the bifurcation point giving the expression for $\boldsymbol{y}$ [45]

$$\boldsymbol{y} = \tfrac{1}{2}\boldsymbol{k}_{20} z^2 + \boldsymbol{k}_{11} z\bar{z} + \tfrac{1}{2}\boldsymbol{k}_{02}\bar{z}^2 \tag{2.15}$$

The evaluation for the vectors $\boldsymbol{k}_{20}$, $\boldsymbol{k}_{11}$ and $\boldsymbol{k}_{02}$ are given in Appendix B.

The time derivative of z is obtained by premultiplying Eq. (2.3) with $\boldsymbol{\psi}_c^H$ and substituting in Eq. (2.14)

$$\frac{\mathrm{d}z}{\mathrm{d}t} = i\omega z + \boldsymbol{\psi}_c^H \boldsymbol{F}\left(z\boldsymbol{\phi}_c + \bar{z}\bar{\boldsymbol{\phi}}_c + \boldsymbol{y}\right) + \boldsymbol{\psi}_c^H \Big(\boldsymbol{R}_\Theta + A_\Theta + \boldsymbol{F}_\Theta \left(z\boldsymbol{\phi}_c + \bar{z}\bar{\boldsymbol{\phi}}_c + \boldsymbol{y}\right) \Big)\boldsymbol{\theta} \tag{2.16}$$

The functions $\boldsymbol{\mathcal{B}}$ to $\boldsymbol{\mathcal{E}}$ now have a simpler explicit form due to the fact that there is only one mode. These are given in Appendix B. Equations (2.12) and (2.16) govern the dynamics of the reduced model based on multiple modes and the single critical mode, respectively.

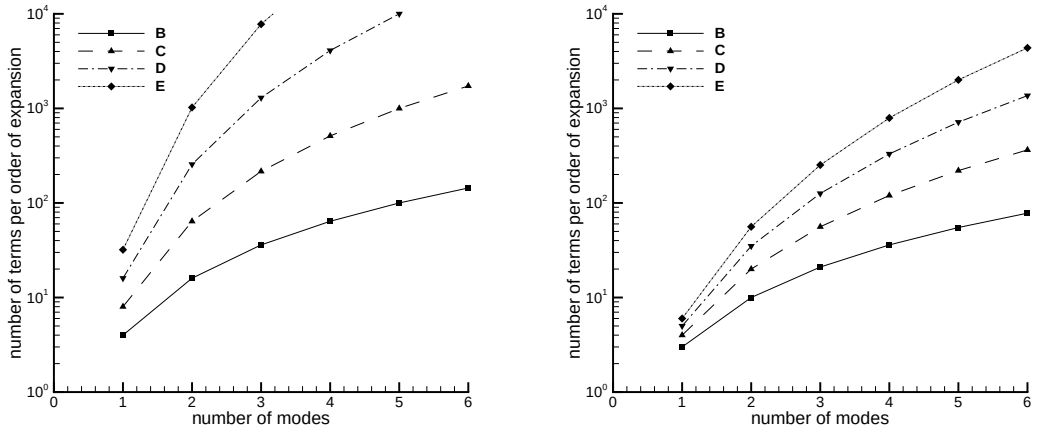

(a) direct

(b) exploiting symmetry

Figure 2.1: Number of terms per order of expansion

2.3 Discussion of Computational Cost

Now the cost of forming and integrating the reduced formulation is discussed in more detail. As explicitly shown in Appendix A, each function of increasing order of derivative $\boldsymbol{\mathcal{B}}$ to $\boldsymbol{\mathcal{E}}$ involves increasing numbers of terms for its evaluation when written as function of $\boldsymbol{z}$. This relation is presented in Fig. 2.1. The symmetry properties of the multilinear functions, e.g. $\boldsymbol{\mathcal{B}}(\boldsymbol{x},\boldsymbol{y}) = \boldsymbol{\mathcal{B}}(\boldsymbol{y},\boldsymbol{x})$, $\boldsymbol{\mathcal{C}}(\boldsymbol{x},\boldsymbol{y},\boldsymbol{y}) = \boldsymbol{\mathcal{C}}(\boldsymbol{y},\boldsymbol{x},\boldsymbol{y}) = \boldsymbol{\mathcal{C}}(\boldsymbol{y},\boldsymbol{y},\boldsymbol{x})$ and so on, can be exploited to gain two advantages. First, fewer terms are required to construct the ROM initially, and secondly, fewer operations are performed for the evaluation of the dynamics of $\boldsymbol{z}$ in Eq. (2.12). Thus, the costs of forming and integrating the reduced model are both decreased.

In the case of simpler models, all the terms of the ROM can be evaluated analytically. However, if the physical model is more complex, such as a finite element model for the structure and CFD for nonlinear aerodynamics, then analytical evaluation is usually not possible. Thus, a matrix-free approach using finite differences is necessary to construct the functions of higher order derivatives requiring only the evaluation of the residual function. The number of residual evaluations per finite difference approximation depends on the order of derivative to be approximated and the order of the finite difference. As an example in Appendix A, the second order central difference schemes in Eq. (A.6) involve between two to six residual evaluations for the functions $\boldsymbol{\mathcal{B}}$ to $\boldsymbol{\mathcal{E}}$ with a single argument.

In addition, the finite difference approximations of the functions $\boldsymbol{\mathcal{B}}$ to $\boldsymbol{\mathcal{E}}$ are defined for a single argument. Consequently for a function with mixed arguments, i.e. different eigenvectors, a set of identities must be used to place the evaluation in a suitable form with a single argument, e.g. $\boldsymbol{\mathcal{B}}(\boldsymbol{x},\boldsymbol{y}) = \frac{1}{4}\big(\boldsymbol{\mathcal{B}}(\boldsymbol{x}+\boldsymbol{y},\boldsymbol{x}+\boldsymbol{y}) - \boldsymbol{\mathcal{B}}(\boldsymbol{x}-\boldsymbol{y},\boldsymbol{x}-\boldsymbol{y})\big)$,

$\boldsymbol{\mathcal{C}}(\boldsymbol{x},\boldsymbol{y},\boldsymbol{y}) = \frac{1}{6}\big(\boldsymbol{\mathcal{C}}(\boldsymbol{x}+\boldsymbol{y},\boldsymbol{x}+\boldsymbol{y},\boldsymbol{x}+\boldsymbol{y}) + \boldsymbol{\mathcal{C}}(\boldsymbol{x}-\boldsymbol{y},\boldsymbol{x}-\boldsymbol{y},\boldsymbol{x}-\boldsymbol{y}) - 2\boldsymbol{\mathcal{C}}(\boldsymbol{x},\boldsymbol{x},\boldsymbol{x})\big)$ and so on. Thus, several finite differences are required for a term with mixed arguments. Additionally, the arguments of the terms are, in general, complex-valued. In situations where complex arithmetic is not possible, such as industrial finite element or CFD codes, these identities must be used again to isolate the real and imaginary parts of the arguments which results in additional finite difference operations as established by Kuznetsov [44].

It can be concluded that the total number of residual evaluations required to approximate a single function of a higher order derivative is significantly higher than the number of terms shown in Fig. 2.1. Using many modes in the ROM basis as well as higher order Taylor expansion, millions of full-order residual evaluations could be required making the construction of the ROM prohibitive. Few, well selected, dominant modes must therefore be chosen.

The above analysis of computational cost shows that if the number of modes used in the reduced model construction is large, then forming the reduced model becomes increasingly expensive. This is particularly true when the physical problem is complex and analytical expressions of the Jacobian matrix and higher derivatives are not possible such that finite difference approximations must be used. The number of residual evaluations required for the finite differences can easily grow to the order of millions for the reduced model formulation including fifth-order terms. In the case where only the single critical mode is used, the associated computational cost is always feasible.

Time integrating the ROM demands the evaluation of the dynamics of the reduced state $\boldsymbol{z}$ in Eq. (2.12). The computational cost associated with running the ROM is directly related to the results presented in Fig. 2.1. Once the ROM terms are evaluated either analytically or by finite differences, projection with Ψ^H gives complex-valued terms, the number of which scales with m. Integration methods for ordinary differential equations, such as schemes of the Runge-Kutta family, are readily available working with complex arithmetic as well. Using industrial CFD codes in the full-order model, the cost of integrating the governing equations of the reduced order model will remain small in comparison.

Chapter 3

Typical Section Aerofoil

The first aeroelastic model, which includes the effect of passive structural nonlinearity and the implementation of nonlinear analysis techniques, is a typical 2D aerofoil section with degrees-of-freedom in pitch, plunge and flap.

Previous work in literature largely focuses on aerofoil sections with two degrees-of-freedom in pitch and plunge with the emphasis on flutter and limit-cycle oscillation (LCO). One work of particular importance is attributed to Lee et al. [46, 47]. In their work, a two degrees-of-freedom aerofoil model with cubic stiffness springs in bending and torsion is presented and this nonlinear structural model is coupled with unsteady linear aerodynamic theory. In Lee et al. [47] the effects of hardening and softening springs on the two degrees-of-freedom aerofoil system are investigated. The emphasis in the study is that of the flutter point. It is found for softening springs that the flutter point depends strongly on the system initial conditions while this is not the case for hardening springs. It is also demonstrated that in the presence of hardening springs the effect of LCO is induced instead of the typical divergent flutter at airspeeds above the linear flutter point. The work of Lee et al. [46, 47] illustrated in a clear way the formulation of the equations of motion from the coupling of the structural equations to the unsteady aerodynamic model.

This formulation provided the basis of the two degrees-of-freedom aerofoil model presented by Da Ronch et al. [48] for the purpose of demonstrating model order reduction. The model is constructed in exactly the same way with nonlinear spring stiffness represented by polynomials up to the cubic-order in both pitch and plunge degrees-of-freedom. The aerodynamics formulation of Lee et al. [46, 47] is extended to include additional contributions from prescribed massless trailing-edge flap input as well as discrete gust perturbations. The nonlinear model order reduction approach described in Chapter 2 is applied to the aeroelastic system. Key results showed the comparison of the full-order model and the reduced-order model for aeroelastic response to initial perturbation as well as discrete gust disturbance. The reduced model is used as well in the application of H^∞ control for gust alleviation. The current work builds upon this

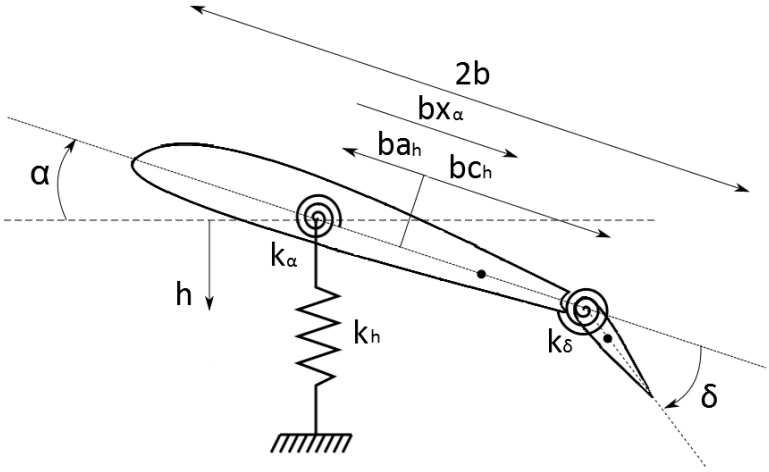

Figure 3.1: Pitch-plunge aerofoil with trailing-edge flap

numerical model to include the trailing-edge flap as an additional degree-of-freedom and thus is no longer assumed massless. Furthermore, the degree of structural nonlinearity is extended to quintic-order with the aim that this higher-order nonlinearity is to be representated accurately by the reduced-order model.

There are a few sources in literature where a three degrees-of-freedom aerofoil has been considered. Kanda and Dowell [49] studied the worst-case gust response of such an aerofoil system using matched-filter theory. It is demonstrated that the worst-case gust profile generated by matched-filter theory is significantly different from a standard discrete gust idealisation and generates a response amplitude that is close to twice that of the worst-case 1-cosine gust. Conner et al. [50] presented a study comparing the experimental and computational system of a typical aerofoil section with control surface free-play. The comparison between the numerical and experimental setup show a 15% difference in the linearised flutter speed. The dynamic time history presented in the paper show accurate although slightly conservative numerical prediction of the experimental result. The key result is demonstrated in that the dynamic response of the aerofoil system scaled with the size of the control surface freeplay. Later, Trickey et al. [51] utilised the same experimental setup to study the effect of freeplay upon the induction of LCO. Time histories comparing numerical and experimental LCO were presented.

On the subject of freeplay nonlinearity where the structural stiffness is represented by piecewise segments, it is important to note that for systems with piecewise changes, standard time integration methods typically cannot capture precisely the location of the switching point where the change in stiffness profile occurs [52]. One way to address this issue was presented by Conner et al. [53] which utilised Hénon's method. Hénon's method allows for the determination of the switch point in a piecewise system exactly

in just one integration step. This is done by rearranging the state-space equations such that time becomes the dependent state variable and the variable corresponding to the piecewise stiffness change (for example, flap deflection) becomes the independent variable. The rearranged state-space equations are then integrated with respect to this spatial variable and the increment in time from the current time to exactly the switching point is obtained. The Hénon's method is readily included as an additional step in a standard Runge-Kutta integration scheme whenever change in subdomain is detected. Tang and Dowell [54] also presented a study on the typical three degrees-of-freedom aerofoil section with focus on control surface free-play. The study involves comparison between experimental and theoretical modelling of the aerofoil section. One particular highlight of the theoretical model is the implementation of Peters' finite state aerodynamic theory [15]. The results presented include flutter, LCO and gust responses. It is concluded that an increase in initial pitching angle contributed to a reduction in flow velocity required for large LCO oscillations.

In this chapter, the complete structural formulation of the three degrees-of-freedom aerofoil with polynomial spring nonlinearity is first introduced. This is followed by the coupled linear aerodynamics model based on Wagner's and Küssner's functions. Next, linear stability results are presented to evaluate the linear flutter point and provide numerical verification with results established in literature. Further numerical verification is demonstrated by introducing structural free-play into the torsional degree-of-freedom and the free response simulated in time. This is again compared against results found in literature. Gust response analysis is then investigated for the linear structural model and the corresponding linear reduced-order model. Finally the study moves onto the effects of higher-order structural nonlinearity in limit-cycle oscillation analysis and corresponding nonlinear model reduction. The chapter finishes with conclusions on the aerofoil investigation.

3.1 Formulation

3.1.1 Structural Model

Consider a three degrees-of-freedom 2D aerofoil (Fig. 3.1) elastically supported in plunge and pitch and equipped with a trailing-edge flap. The plunge deformation is indicated by h positive downward. The pitch angle α is denoted positive nose up, and δ is the flap deflection angle positive down. The structural system consists of three elastic springs and dampers associated with each degree-of-freedom.

To derive the structural equations of motion it is beneficial to use Lagrange equations given as follows

$$\frac{\mathrm{d}}{\mathrm{d}t}\left(\frac{\partial \mathcal{L}}{\partial \dot{q}_i}\right) - \frac{\partial \mathcal{L}}{\partial q_i} + \frac{\partial D}{\partial \dot{q}_i} = Q_i, \quad i = 1, 2, \ldots, n \tag{3.1}$$

Here $\mathcal{L}$ is the Lagrangian defined in the classical form $\mathcal{L} = T_{KE} - V$ where T_{KE} is the total kinetic energy of the aeroelastic system and V is the potential energy. The viscous damping forces are denoted by D and the generalised forces are denoted by Q_i which include any contribution which cannot be derived from a potential function such as aerodynamic or external forces. The expression q_i denotes the generalised coordinates defined as a finite set of independent variables.

The equations of motion are thus derived in dimensional form with nonlinear spring terms as follows

$$\begin{aligned} m\ddot{h} + S_\alpha \ddot{\alpha} + S_\delta \ddot{\delta} + C_h \dot{h} + K_h f_h &= -L \\ S_\alpha \ddot{h} + I_\alpha \ddot{\alpha} + \left(I_\delta + b\left(c_h - a_h\right) S_\alpha\right) \ddot{\delta} + C_\alpha \dot{\alpha} + K_\alpha f_\alpha &= M_\alpha \\ S_\delta \ddot{h} + \left(I_\delta + b\left(c_h - a_h\right) S_\delta\right) \ddot{\alpha} + I_\delta \ddot{\delta} + C_\delta \dot{\delta} + K_\delta f_\delta &= M_\delta + H_\delta \end{aligned} \tag{3.2}$$

where f_h, f_α, and f_δ are the nonlinear spring polynomials up to fifth-order, while the terms K_h, K_α and K_δ denote the stiffness coefficients in bending, torsion and flap, respectively. The terms C_h, C_α and C_δ are the viscous damping coefficients in the respective degrees-of-freedom. The right-hand side terms L, M_α, and M_δ are the total aerodynamic lift, pitching moment $\big($about the elastic axis$\big)$ and flap hinge moment $\big($about the hinge axis$\big)$, respectively. The term H_δ represented any artificially prescribed external hinge moment for the purpose of control inputs. The static moment of the aerofoil-flap system about the elastic axis is denoted by $S_\alpha = mx_\alpha b$, while $S_\delta = mx_\delta b$ is the static moment of only the flap about the hinge axis. Similarly, I_α and I_δ are the moments of inertia. The remaining terms m, b, c_h, and a_h are the aerofoil-flap mass, the semi-chord, the non-dimensional distance from the mid-chord to the flap hinge, and to the elastic axis, respectively.

It is convenient to express equations in non-dimensional form. First h is non-dimensionalisd with respect to the semi-chord and then the non-dimensional time τ is introduced. These are given as

$$h = \xi b \quad \text{and} \quad \frac{\mathrm{d}}{\mathrm{d}t} = \frac{\mathrm{d}}{\mathrm{d}\tau}\frac{U}{b} \tag{3.3}$$

where U is the reference freestream velocity. Also the following parameters are introduced

$$\begin{aligned} x_\alpha &= \frac{S_\alpha}{m\,b}, \quad r_\alpha = \sqrt{\frac{I_\alpha}{m\,b^2}}, \quad \bar{\omega}_1 = \frac{\omega_h}{\omega_\alpha} \\ x_\delta &= \frac{S_\delta}{m\,b}, \quad r_\delta = \sqrt{\frac{I_\delta}{m\,b^2}}, \quad \bar{\omega}_2 = \frac{\omega_\delta}{\omega_\alpha} \end{aligned} \tag{3.4}$$

Here, x_α is the offset of the centre of gravity of the aerofoil-flap system from the elastic axis non-dimensionalised by the semi-chord b. The term x_δ is the reduced centre of

gravity distance from the flap hinge. The radius of gyration of the aerofoil-flap system about the elastic axis is denoted by r_α. Correspondingly, r_δ is the reduced radius of gyration of the flap, that is, the radius at which the entire mass of the aerofoil-flap would have to be concentrated to give the moment of inertia of the flap I_δ. The natural uncoupled frequency in plunge is denoted $\omega_h = \sqrt{K_h/m}$ and similarly for pitch $\omega_\alpha = \sqrt{K_\alpha/I_\alpha}$ and flap $\omega_\delta = \sqrt{K_\delta/I_\delta}$. The uncoupled natural frequency ratios in plunge and flap with respect to pitch are denoted by $\bar{\omega}_1$ and $\bar{\omega}_2$, respectively. Lastly, the corresponding damping ratios are defined as

$$\zeta_h = \frac{C_h}{2\sqrt{mK_h}}, \quad \zeta_\alpha = \frac{C_\alpha}{2\sqrt{I_\alpha K_\alpha}} \quad \text{and} \quad \zeta_\delta = \frac{C_\delta}{2\sqrt{I_\delta K_\delta}} \tag{3.5}$$

for the three degrees-of-freedom.

The resulting equations are given as follows in non-dimensional form, where $(\,)'$ indicates derivative with respect to non-dimensional time,

$$\begin{aligned}
\xi'' + x_\alpha \alpha'' + x_\delta \delta'' + 2\zeta_\xi \frac{\bar{\omega}_1}{\overline{u}} \xi' + \frac{\bar{\omega}_1^2}{\overline{u}^2} f_\xi &= -\frac{C_L}{\pi\mu} \\
x_\alpha \xi'' + r_\alpha^2 \alpha'' + \left(r_\delta^2 + (c_h - a_h)\, x_\delta\right) \delta'' + 2\zeta_\alpha \frac{r_\alpha^2}{\overline{u}} \alpha' + \frac{r_\alpha^2}{\overline{u}^2} f_\alpha &= \frac{2C_{M\alpha}}{\pi\mu} \\
x_\delta \xi'' + \left(r_\delta^2 + (c_h - a_h)\, x_\delta\right) \alpha'' + r_\delta^2 \delta'' + 2\zeta_\delta \frac{\bar{\omega}_2 r_\delta^2}{\overline{u}} \delta' + \frac{\bar{\omega}_2^2 r_\delta^2}{\overline{u}^2} f_\delta &= \frac{2C_{M\delta}}{\pi\mu} + \bar{H}_\delta
\end{aligned} \tag{3.6}$$

where the nonlinear spring polynomials f_ξ, f_α, and f_δ are

$$\begin{aligned}
f_\xi &= \xi + \beta_{\xi 3}\xi^3 + \beta_{\xi 5}\xi^5 \\
f_\alpha &= \alpha + \beta_{\alpha 3}\alpha^3 + \beta_{\alpha 5}\alpha^5 \\
f_\delta &= \delta + \beta_{\delta 3}\delta^3 + \beta_{\delta 5}\delta^5
\end{aligned} \tag{3.7}$$

with $\beta_{\xi 3}$ and $\beta_{\xi 5}$ as the specific stiffness coefficients relating to cubic and quintic terms. Analogous coefficients apply to pitch and flap degrees-of-freedom denoted by subscripts α and δ. Figure 3.2 illustrates the torsional spring stiffness f_α for the linear case as well as two baseline nonlinear configurations which will be discussed in Section 3.2.4 hereafter.

The reduced velocity $\bar{u}$ and the mass ratio μ are defined as

$$\bar{u} = \frac{U}{\omega_\alpha b} \quad \text{and} \quad \mu = \frac{m}{\pi\rho b} \tag{3.8}$$

The term $\bar{H}_\delta$ is the non-dimensional H_δ.

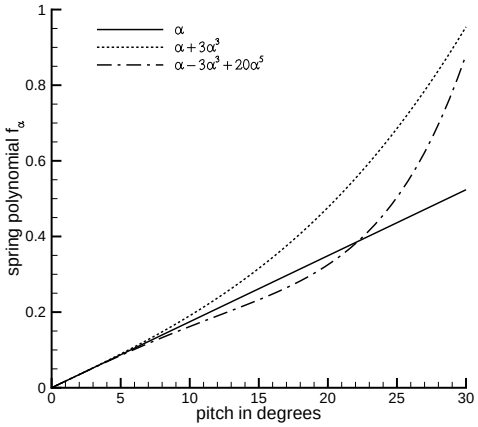

Figure 3.2: Torsional spring stiffness polynomial f_α

3.1.2 Wagner and Küssner Aerodynamics

The definitions of sectional lift and moment coefficients are introduced as

$$C_L = \frac{L}{\frac{1}{2}\rho U^2 2b}, \quad C_{M\alpha} = \frac{M_\alpha}{\frac{1}{2}\rho U^2 (2b)^2} \quad \text{and} \quad C_{M\delta} = \frac{M_\delta}{\frac{1}{2}\rho U^2 (2b)^2} \tag{3.9}$$

where ρ is the reference flow density. Fung [55] show that the aerodynamic force and moment coefficients can be expressed in time domain via Wagner's function.

Following the work of Kanda and Dowell [49] the unsteady aerodynamic forces and moments can be separated into two components; contributions from the wing motion due to both circulatory and non-circulatory origin and gust disturbance. The coefficients can then be written as

$$C_L = C_L^m + C_L^g, \quad C_{M\alpha} = C_{M\alpha}^m + C_{M\alpha}^g \quad \text{and} \quad C_{M\delta} = C_{M\delta}^m + C_{M\delta}^g \tag{3.10}$$

where the superscripts m and g denote to contributions from aerofoil motion and gust, respectively. To proceed with the aerodynamic formulation, the non-dimensional downwash at the three-quarter chord point is introduced

$$w_{0.75}(\tau) = \alpha(\tau) + \xi'(\tau) + \left(\tfrac{1}{2} - a_h\right)\alpha'(\tau) + \pi^{-1}T_{10}\delta(\tau) + \frac{1}{2}\pi^{-1}T_{11}\delta'(\tau) \tag{3.11}$$

The lift coefficient from purely the structural motion in pitch, plunge and flap deflection is obtained from Theodorsen [56] and Lee et al. [46] as

$$\begin{aligned} C_L^m = {} & \pi\left(\xi'' - a_h\alpha''\right) + \pi\alpha' - T_4\delta' - T_1\delta'' \\ & + 2\pi\left(w_{0.75}(0)\,\Phi_w(\tau) + \int_0^\tau w'_{0.75}(\sigma)\,\Phi_w(\tau-\sigma)\,d\sigma\right) \end{aligned} \tag{3.12}$$

where the last line denotes the circulatory contribution. Accordingly, the moment coefficients are defined as

$$C_{M\alpha}^{m} = \tfrac{1}{2}\pi a_h\left(\xi^{''} - a_h\alpha^{''}\right) - \tfrac{1}{2}\pi\left(\tfrac{1}{2} - a_h\right)\alpha^{'} - \tfrac{1}{16}\pi\alpha^{''} - \left(T_4 + T_{10}\right)\delta - \left(T_1 - T_8 - \left(c_h - a_h\right)T_4 + \tfrac{1}{2}T_{11}\right)\delta^{'} + \left(T_7 + \left(c_h - a_h\right)T_1\right)\delta^{''} + \pi\left(a_h + \tfrac{1}{2}\right)\left(w_{0.75}\left(0\right)\Phi_w\left(\tau\right) + \int_0^{\tau} w_{0.75}^{'}\left(\sigma\right)\Phi_w\left(\tau - \sigma\right)d\sigma\right) \quad (3.13)$$

and

$$C_{M\delta}^{m} = -\tfrac{1}{2}\left(2T_{13}\,\alpha^{''} - T_1\xi - \left(T_4\left(a_h - \tfrac{1}{2}\right) - T_1 - 2T_9\right)\alpha^{'}\right) + \tfrac{1}{2}\pi^{-1}\left(T_3\delta^{''} + \tfrac{1}{2}T_4T_{11}\delta^{'} - \left(T_5 - T_4T_{10}\right)\delta\right) - \tfrac{1}{2}T_{12}\left(w_{0.75}\left(0\right)\Phi_w\left(\tau\right) + \int_0^{\tau} w_{0.75}^{'}\left(\sigma\right)\Phi_w\left(\tau - \sigma\right)d\sigma\right) \quad (3.14)$$

where the Wagner function $\Phi_w\left(\tau\right)$ is given by

$$\Phi_w\left(\tau\right) = 1 - \Psi_1 e^{-\varepsilon_1\tau} - \Psi_2 e^{-\varepsilon_2\tau} \quad (3.15)$$

with constants $\Psi_1 = 0.165$, $\Psi_2 = 0.335$, $\varepsilon_1 = 0.0455$ and $\varepsilon_2 = 0.3$ following Jones' approximation [57]. The Wagner function describes the ratio of transient to steady state lift (with circulatory origin) for a general aerofoil motion and $\Phi_w(0) = 0.5$. The terms T_i are constants relating to the aerofoil geometry as given by Theodorsen [56].

The lift and moment coefficients here may, in addition, be modified by additional gust influence terms due to an arbitrary gust excitation $W_g(\tau)$. From Dessi and Mastroddi [58] these are given as follows

$$C_L^g = 2\pi\left(W_g\left(0\right)\Psi_k\left(\tau\right) + \int_0^{\tau} W_g^{'}(\sigma)\Psi_k\left(\tau - \sigma\right)d\sigma\right) \quad (3.16)$$

$$C_{M\alpha}^g = \pi\left(a_h + \tfrac{1}{2}\right)\left(W_g\left(0\right)\Psi_k\left(\tau\right) + \int_0^{\tau} W_g^{'}(\sigma)\Psi_k\left(\tau - \sigma\right)d\sigma\right) \quad (3.17)$$

where the influence of the gust disturbance on the flap hinge moment is neglected ($C_{m\delta}^g = 0$) as discussed in Kanda and Dowell [49]. The term $\Psi_k\left(\tau\right)$ is the Küssner function approximated in the following form

$$\Psi_k\left(\tau\right) = 1 - \Psi_3 e^{-\varepsilon_3\tau} - \Psi_4 e^{-\varepsilon_4\tau} \quad (3.18)$$

with constants $\Psi_3 = 0.5792$, $\Psi_4 = 0.4208$, $\varepsilon_3 = 0.1393$ and $\varepsilon_4 = 1.802$ given by Leishman [26]. The Küssner function describes the ratio of transient to steady state lift for an aerofoil penetrating a sharp-edged gust and $\Psi_k(0) = 0$.

3.1.3 Recasting into First-Order Form

The above equations governing the system dynamics contain integro-differential terms. The terms involving the convolution integral can be eliminated by introducing the following variables as first presented by Lee et al. [46]

$$
\begin{aligned}
w_1 &= \int_0^\tau e^{-\varepsilon_1(\tau-\sigma)}\alpha\,(\sigma)\,d\sigma & w_2 &= \int_0^\tau e^{-\varepsilon_2(\tau-\sigma)}\alpha\,(\sigma)\,d\sigma \\
w_3 &= \int_0^\tau e^{-\varepsilon_1(\tau-\sigma)}\xi\,(\sigma)\,d\sigma & w_4 &= \int_0^\tau e^{-\varepsilon_2(\tau-\sigma)}\xi\,(\sigma)\,d\sigma \\
w_5 &= \int_0^\tau e^{-\varepsilon_1(\tau-\sigma)}\delta\,(\sigma)\,d\sigma & w_6 &= \int_0^\tau e^{-\varepsilon_2(\tau-\sigma)}\delta\,(\sigma)\,d\sigma \\
w_7 &= \int_0^\tau e^{-\varepsilon_3(\tau-\sigma)}W_g\,(\sigma)\,d\sigma & w_8 &= \int_0^\tau e^{-\varepsilon_4(\tau-\sigma)}W_g\,(\sigma)\,d\sigma
\end{aligned}
\tag{3.19}
$$

The dynamics of these states are evaluated as

$$
\begin{aligned}
\dot{w_1} &= \alpha - \varepsilon_1 w_1 & \dot{w_2} &= \alpha - \varepsilon_2 w_2 \\
\dot{w_3} &= h - \varepsilon_1 w_3 & \dot{w_4} &= h - \varepsilon_2 w_4 \\
\dot{w_5} &= \delta - \varepsilon_1 w_5 & \dot{w_6} &= \delta - \varepsilon_2 w_6 \\
\dot{w_7} &= W_g - \varepsilon_3 w_7 & \dot{w_8} &= W_g - \varepsilon_4 w_8
\end{aligned}
\tag{3.20}
$$

using the Leibniz integral rule.

Both the structural equations and the aerodynamic force and moment expressions depend on the same shared system states, which are $\boldsymbol{X}_s$ for the structural degrees-of-freedom and $\boldsymbol{W}_f$ for the augmented aerodynamic states,

$$\boldsymbol{X}_s = [\xi, \alpha, \delta]^T \tag{3.21}$$

$$\boldsymbol{W}_f = [w_1, w_2, w_3, w_4, w_5, w_6, w_7, w_8]^T \tag{3.22}$$

By combining the equations and collecting the coefficients of common terms one obtains the governing ordinary differential equation decribing the dynamics of the structural system. This is expressed in matrix-vector form as

$$M\ddot{\boldsymbol{X}}_s + C\dot{\boldsymbol{X}}_s + K\boldsymbol{X}_s + \boldsymbol{k}_N(\boldsymbol{X}_s) + D_f\boldsymbol{W}_f = \boldsymbol{f}_a + \boldsymbol{f}_e \tag{3.23}$$

Similarly, the aerodynamics system in Eq. (3.20) can be formulated as

$$\dot{\boldsymbol{W}}_f = A_{ff}\boldsymbol{W}_f + A_{fx}\boldsymbol{X}_s + \boldsymbol{f}_g \tag{3.24}$$

In these previous equations, the matrix terms M, C and K are the effective mass, damping and stiffness matrices containing structural and aerodynamic contributions.

The term $\boldsymbol{k}_N$ is a nonlinear vector arising from the polynomial stiffness. The vector $\boldsymbol{f}_a$ arises from the influence of initial conditions upon the unsteady aerodynamic forces. The term $\boldsymbol{f}_e$ is the non-dimensional form of any applied external force or moment, for instance the flap hinge moment for control input. The matrix D_f relates the structural equations to the augmented aerodynamic states. The matrix A_{ff} relates the fluid unknowns to their first time derivatives and the matrix A_{fx} couples the fluid equations to the structural degrees-of-freedom. The vector $\boldsymbol{f}_g$ describes the influence of the external gust disturbance in the aerodynamic equations. The explicit form of these matrices and vectors are given in Appendix C.1.

In the final step, Eqs. (3.23) and (3.24) are recast in a coupled first-order ordinary differential equation of the general form as given in Eq. (2.2) where the unknowns are partitioned into structural and fluid contribution as

$$\boldsymbol{W} = \left[\boldsymbol{W}_s^T, \boldsymbol{W}_f^T\right]^T \quad \text{where} \quad \boldsymbol{W}_s = \left[\boldsymbol{X}_s^T, \dot{\boldsymbol{X}}_s^T\right]^T \tag{3.25}$$

and the system parameters $\boldsymbol{\Theta}$ consist of the reduced velocity $\bar{u}$, the gust velocity W_g and the prescribed external hinge moment H_δ. The corresponding residual $\boldsymbol{R}$ is given by

$$\boldsymbol{R}(\boldsymbol{W}, \boldsymbol{\Theta}) = A_L(\bar{u})\,\boldsymbol{W} + \boldsymbol{b}_N(\boldsymbol{W}, \bar{u}) + \boldsymbol{b}_a + \boldsymbol{b}_e(W_g, H_\delta) \tag{3.26}$$

The matrix A_L is defined as

$$A_L = \begin{pmatrix} 0 & I & 0 \\ -M^{-1}K & -M^{-1}C & A_{\dot{x}f} \\ A_{fx} & 0 & A_{ff} \end{pmatrix} \tag{3.27}$$

where the matrix block A_{ff} is the Jacobian matrix of the equations in Eq. (3.24) with respect to the fluid unknowns, while the matrix blocks $A_{\dot{x}f} = -M^{-1}D_f$ and A_{fx} couple the structural equations and the fluid equations. The vectors $\boldsymbol{b}_N$, $\boldsymbol{b}_a$ and $\boldsymbol{b}_e$ denote contributions from nonlinear terms, aerodynamics due to initial conditions and external inputs, respectively,

$$\boldsymbol{b}_N = \begin{pmatrix} 0 \\ -M^{-1}\boldsymbol{k}_N \\ 0 \end{pmatrix}, \quad \boldsymbol{b}_a = \begin{pmatrix} 0 \\ -M^{-1}\boldsymbol{f}_a \\ 0 \end{pmatrix}, \quad \text{and} \quad \boldsymbol{b}_e = \begin{pmatrix} 0 \\ -M^{-1}\boldsymbol{f}_e \\ \boldsymbol{f}_g \end{pmatrix} \tag{3.28}$$

Note that the equilibrium point for the aerofoil model presented herein is the trivial solution.

The set of first-order ordinary differential equations in time is the starting point for the application of the model reduction presented in Chapter 2. As the aerodynamics are linear following the theories of Wagner and Küssner, the higher-order terms in the model reduction arise only from the nonlinear terms contained in vector $\boldsymbol{b}_N$. The functions

$\boldsymbol{\mathcal{B}}$ to $\boldsymbol{\mathcal{E}}$ are evaluated analytically herein, which is straightforward for the pitch-plunge aerofoil structural model with linear aerodynamics, and have been tested by comparison with finite difference evaluations. Since the nonlinear residual, the Jacobian matrix and the higher-order derivatives are all known analytically, their derivatives with respect to the reduced velocity $\bar{u}$ follow immediately as well. To account for the gust input in the reduced model, the derivative of the external input vector $\boldsymbol{b}_e$ with respect to the gust velocity W_g is required adding a contribution to $\boldsymbol{R}_{\Theta}$ in Eq. (2.12). The same applies for control hinge moment $\bar{H}_\delta$. As is explicitly shown in Appendix C.1, the gust entries in vector $\boldsymbol{b}_e$ directly take the values of the gust velocity and thus the derivative with respect to gust velocity becomes trivial. Control input is currently not considered.

Operations with higher-order derivatives, such as vector multiplication, using dense array storage schemes becomes prohibitive. Since these higher dimensional arrays are very sparse due to the discrete polynomial form of the structural nonlinearity, a higher-order extension of the well known compressed sparse row format presented by Saad [59] has been devised for the work presented herein. All sparse array operations have been compared to equivalent dense operations for verification and very significant savings in computing time are achieved.

3.2 Results

This section presents numerical results obtained using this three degrees-of-freedom aerofoil model and also a reduced two degrees-of-freedom system with the flap de-activated. First, for the three degrees-of-freedom system, we deal with linear stability analysis for the evaluation of the flutter speed. Secondly, to further verify the structural model, freeplay is introduced into pitch degree-of-freedom and time domain response simulated and compared against published result in literature. Thirdly, gust response analysis is introduced. Lastly, the effect of structural nonlinearity in polynomial form is examined for the reduced two degrees-of-freedom system. Both cubic and quintic-order nonlinearity are introduced into the pitch degree-of-freedom and results of the corresponding reduced-order models are discussed. This is to illustrate the effect of hardening and softening nonlinearity upon the LCO response behaviour of the aerofoil. The specific novelty of this work here is the application of higher-order ROM to represent higher-order structural nonlinearity and capturing the associated LCO behaviour. The investigation of LCO response arising from higher-order structural nonlinearity within the ROM framework has been published in the journal of Nonlinear Dynamics.

3.2.1 Linear Stability Analysis

The eigenvalues of the Jacobian matrix provide insight into the system stability. The solution has three complex conjugate pairs of eigenvalues corresponding to the three

case	$\overline{\omega}_1$	$\overline{\omega}_2$	μ	a_h	x_α	x_δ	r_α	r_δ	c_h
1	0.2	3.5	100.0	-0.5	0.25	0.0125	0.5	0.0791	0.5
2	1.2	3.5	100.0	-0.5	0.25	0.0125	0.5	0.0791	0.6
3	0.2	–	100.0	-0.5	0.25	–	0.5	–	–

Table 3.1: Model parameters for aerofoil test cases

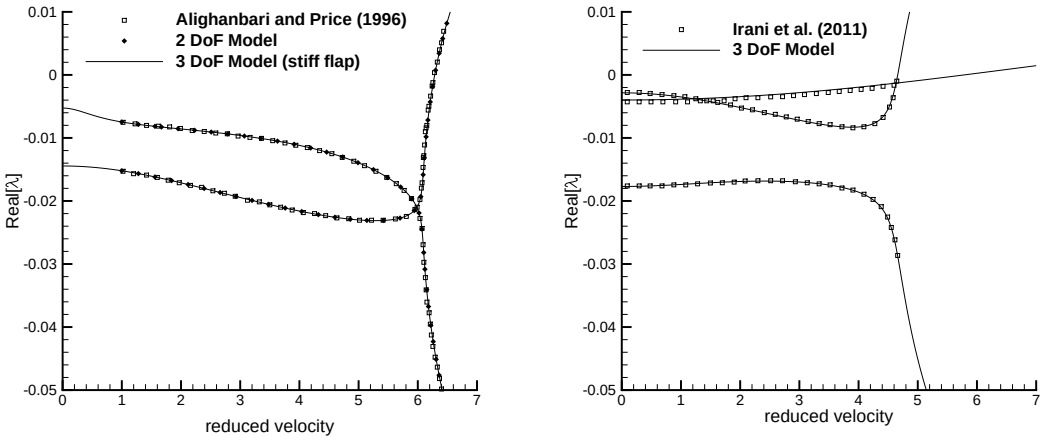

(a) mode trace for case 1

(b) mode trace for case 2

Figure 3.3: Mode traces for verification test cases 1 and 2

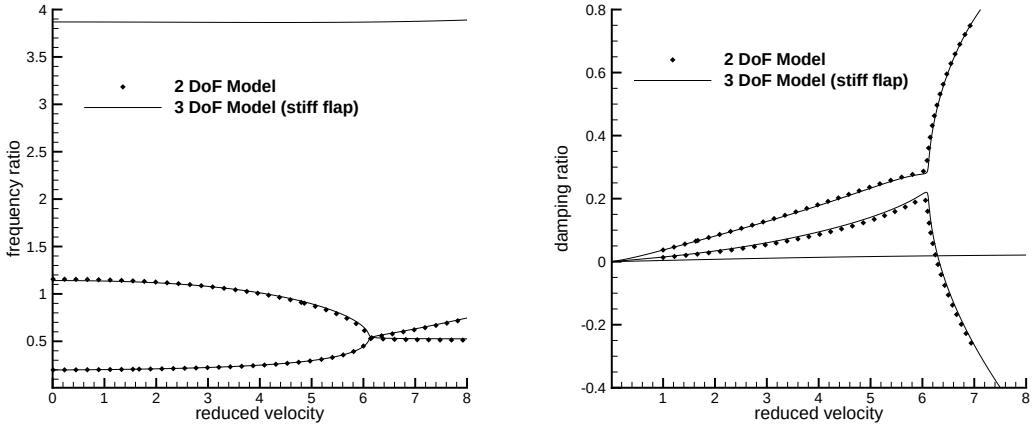

(a) frequency ratio

(b) damping ratio

Figure 3.4: Frequency and damping ratio traces for test case 1

structural degrees-of-freedom, as can be seen in Figs. 3.3 and 3.4, and eight purely real-valued eigenvalues corresponding to the aerodynamic states.

In order to determine the linear flutter point, one varies the reduced velocity and solves for the eigenvalues of the Jacobian matrix. The point where the real part of a pair of complex conjugate eigenvalues changes sign from negative to positive indicates

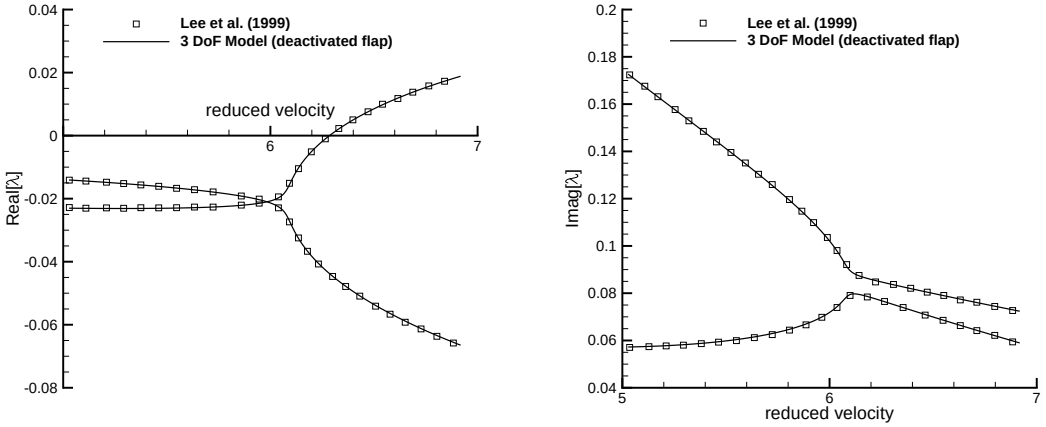

(a) real part

(b) imaginary part

Figure 3.5: Mode traces for verification test case 3

the onset of flutter. Since the model here is small in dimension, it is possible to solve for the eigensolution including right and left eigenvectors directly. In the case the fluid is modelled using CFD, the system's Jacobian matrix typically extends to a size of order of millions. Solving the eigenvalue problem directly becomes prohibitive and in this case, the Schur complement method [32] as discussed in Chapter 2 can be used, for instance.

The first comparison is made with a two degrees-of-freedom aerofoil model presented by Alighanbari and Price [60]. Since this specific comparison is made between a three degrees-of-freedom and a two degrees-of-freedom model, it is necessary to enforce a very high stiffness in the flap degree of freedom by setting a high value of $\overline{\omega}_2$. This effectively limits the dynamics of the three degrees-of-freedom model to a two degrees-of-freedom system. The system parameters used are given in Tab. 3.1 for case 1 with $\overline{\omega}_2$ enforced to be 300. The nonlinear stiffness coefficients are all set to zero. The mode tracing show excellent agreement to the result presented by Alighanbari and Price [60] in Fig. 3.3 (a). The linear instability point is found to be $\bar{u}_L = 6.285$; this value is also reported from a two degrees-of-freedom model investigated by Da Ronch et al. [48].

The corresponding frequency and damping ratios for this two degrees-of-freedom test case are given in Fig. 3.4. This is shown together with the results obtained for the three degrees-of-freedom aerofoil corresponding to case 1 in Tab. 3.1. Here, the third distinctive flap mode is observed. The damping ratio takes the form of the standard evaluation $-\lambda_R/\sqrt{\lambda_R^2 + \lambda_I^2}$ where subscripts R and I indicate real and imaginary parts of the eigenvalue.

The flutter speed is also verified against the results presented by Irani et al. [61]. The model presented by Irani et al. [61] is a three degrees-of-freedom aerofoil and the aeroelastic parameters are directly taken from the paper and given in Tab. 3.1 for

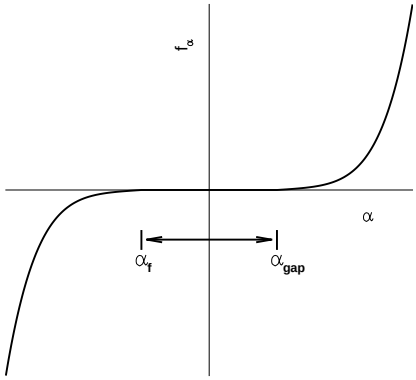

Figure 3.6: Representative freeplay stiffness profile

case 2. The flutter speed is calculated to be $\bar{u}_L = 4.663$ which matches the reported value. Figure 3.3 (b) shows the corresponding mode trace comparison.

Lastly, the stability problem is also verified against the results presented by Lee et al. [47] which is a two degrees-of-freedom aerofoil with aeroelastic parameters given in Tab. 3.1 case 3. Here, to allow for consistent comparison, the flap is deactivated and its dynamics fully removed from the equations of motion. The tracing of the eigenvalue problem, originating in the structural part of the coupled system, with respect to the reduced velocity is given in Fig. 3.5. This specific configuration will be investigated in further detail in Section 3.2.4.

3.2.2 Analysis of Pitch Free-Play

This section deals with the introduction of freeplay nonlinearity into the structural model. This constitutes part of the work aimed to provide additional numerical verification for the structural model. It was noted in the beginning of this chapter that precisely capturing the switching point where the change in structural stiffness occurs can be a challenge. In the current investigation the time step is set to a very small value such that accurately locating the switching point during the time integration is ensured.

A discrete freeplay gap can be introduced into each of the structural degrees-of-freedom. Here a single freeplay gap have been mathematically formulated and included into the pitch degree-of-freedom. This is achieved by modifying the non-dimensionalised state-space equations of motion (3.6). Specifically, the nonlinear spring polynomial f_α

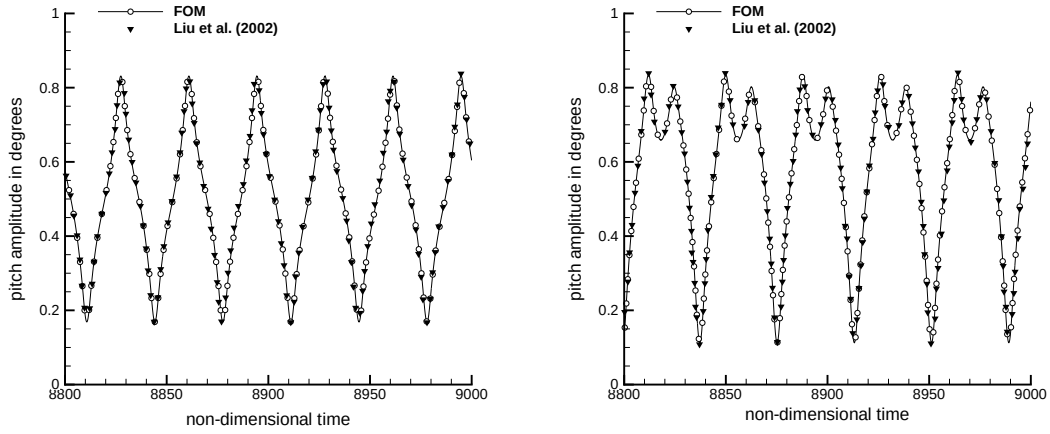

(a) $\bar{u}/\bar{u}_L = 0.2000$ (b) $\bar{u}/\bar{u}_L = 0.2200$

Figure 3.7: Steady state time history for freeplay (case 3)

given in Eq. (3.7) is now replaced with the following conditional form

$$f_\alpha = \begin{cases} (\alpha - \alpha_\mathrm{f} - \alpha_\mathrm{gap}) \\ +\beta_{\alpha 3}\left(\alpha - \alpha_\mathrm{f} - \alpha_\mathrm{gap}\right)^3 + \beta_{\alpha 5}\left(\alpha - \alpha_\mathrm{f} - \alpha_\mathrm{gap}\right)^5, & \alpha > \alpha_\mathrm{f} + \alpha_\mathrm{gap} \\ 0, & \alpha_\mathrm{f} < \alpha < \alpha_\mathrm{f} + \alpha_\mathrm{gap} \\ (\alpha - \alpha_\mathrm{f}) + \beta_{\alpha 3}\left(\alpha - \alpha_\mathrm{f}\right)^3 + \beta_{\alpha 5}\left(\alpha - \alpha_\mathrm{f}\right)^5, & \alpha < \alpha_\mathrm{f} \end{cases} \tag{3.29}$$

where α_f indicates the lower limit of zero stiffness range and α_gap indicates the upper limit. A typical profile for this conditional spring polynomial is illustrated in Fig. 3.6.

The updated equations of motion are integrated in time using the standard second order Runge-Kutta scheme. A direct if-condition placed in the time integration changes the evaluation of f_α based on the current value of pitch deflection α. This is how Eq. (3.29) is evaluated numerically. This essentially changes the equations of motions that is solved based on the value of α in the current time step.

For the purpose of comparison to established results, the flap is deactivated here and pitch freeplay modification to the resulting two degrees-of-freedom aerofoil model is verified against the results presented by Liu et al. [52]. The structural parameters used here is based on the values for case 3 in Tab. 3.1 which are originally chosen from Price et al. [62]. A pitch freeplay gap of 0.5 degrees between +0.25 and +0.75 degrees is specified. That is $\alpha_f = 0.25$ and $\alpha_{gap} = 0.5$. The polynomial pitch stiffness terms are zero with $\beta_{\alpha 3} = \beta_{\alpha 5} = 0$ and the plunge stiffness is enforced to be purely linear. The linear flutter speed for this system is reported in [48, 63] as well as verified in the previous Section 3.2.1 to be $\bar{u}_L = 6.2851$. In the presence of a freeplay gap in the torsional spring the system admits various nonlinear behaviour below the linear flutter point [52].

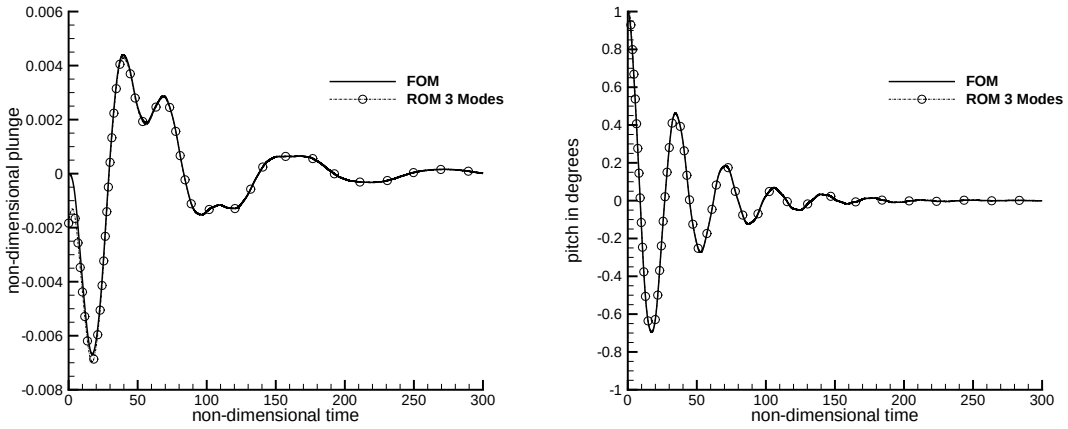

(a) plunge response

(b) pitch response

Figure 3.8: Free response to one degree initial disturbance in pitch angle at $\bar{u} = 5$

Two time domain simulations are performed at $\bar{u}/\bar{u}_L$ of 0.2000 and 0.2200 respectively with initial pitch of 3.0 degrees. The initial pitch angle is chosen to be a small value such that the steady-state response for pitch and plunge are small enough to ensure the validity of the linear aerodynamic model. The non-dimensional time step is chosen to be a small value at 0.01 to ensure stability and accuracy. Figure 3.7 shows the nonlinear steady-state responses. The results obtained by Runge-Kutta time integration shown by the steady-state oscillations show excellent agreement with the results reported by Liu et al. [52] as can be observed in Fig. 3.7.

3.2.3 Gust Response Analysis

In this section the three degrees-of-freedom model is considered for gust response simulation. Several numerical simulations were run to characterise the gust response of the dynamical system. The model parameters used here are based on case 1 in Tab. 3.1. The discrete 1-cosine gust input is defined as

$$W_g(\tau) = \tfrac{1}{2} W_0 \Big(1 - \cos\left(2\pi L_g^{-1} (\tau - \tau_0) \right) \Big) \tag{3.30}$$

with the gust intensity W_0, the gust wavelength L_g and the gust initial time τ_0.

It is of interest to compare the gust response behaviour as predicted by both the full-order model (FOM) and the reduced-order model (ROM). The structural model is linear, with the cubic and quintic spring coefficients set to zero. Consequently, a linear model reduction is sufficient. The construction of the ROM follows the method detailed in Chapter 2 where the basis vectors contained in the right and left modal matrices Φ, Ψ and the corresponding eigenvalues Λ are evaluated from the system Jacobian matrix.

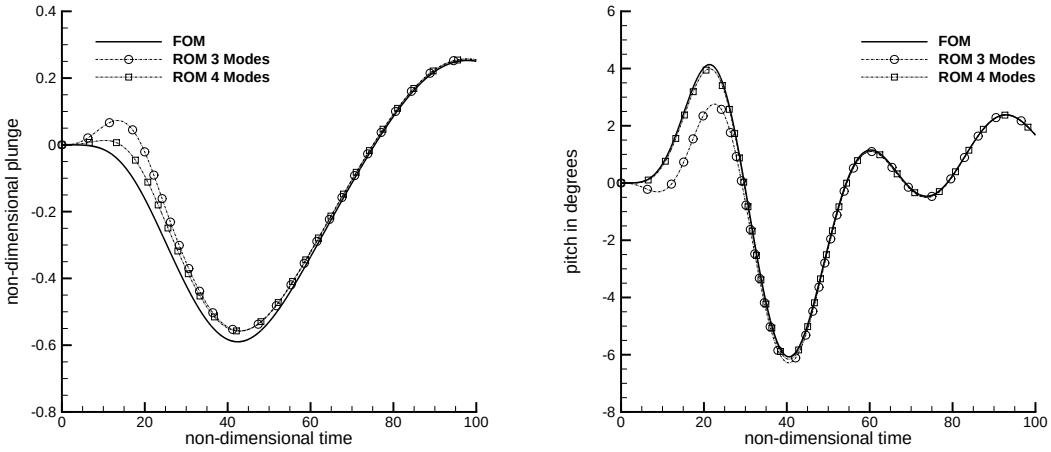

(a) plunge response (b) pitch response

Figure 3.9: Gust response to 1-cosine discrete gust input at $\bar{u} = 5$ with $W_0 = 0.1$, $L_g = 25$ and $\tau_0 = 0$

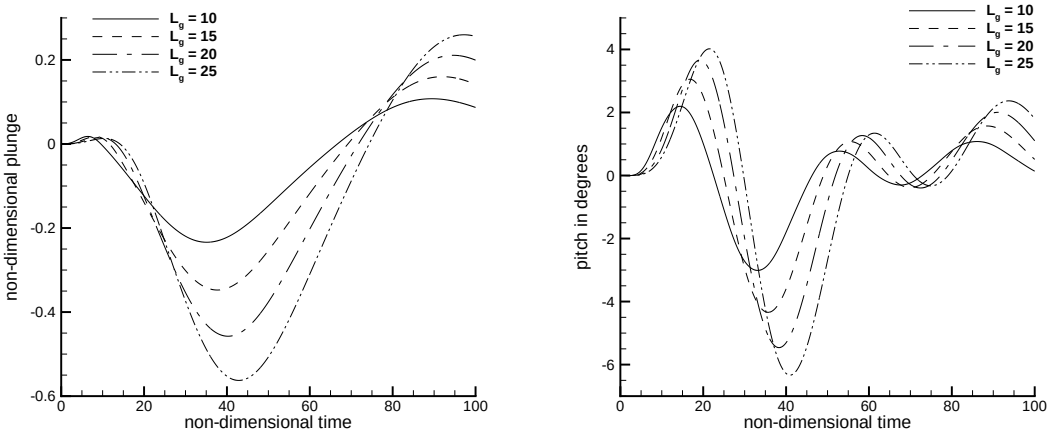

(a) plunge response (b) pitch response

Figure 3.10: ROM determination of worst-case gust response at $\bar{u} = 5.0$ with $W_0 = 0.1$ and $\tau_0 = 0$

Figure 3.8 shows a comparison between the FOM and the corresponding linear ROM for a free response to an initial disturbance of one degree in pitch at a subcritical reduced velocity of 5. Choices of the ROM basis plays an important role in the model's accuracy. For the results presented, the three structural eigensolutions are chosen for the reduced model construction. It is observed here that this is sufficient to accurately predict the free response. This allows a reduction in system size from fourteen to three. While this does not have a significant impact given the current model has few unknowns, should the aerodynamics be replaced by CFD a much larger system reduction is expected.

Figure 3.9 shows the time history comparison of a gust response for the FOM and

ROM. The gust parameters are $W_0 = 0.1$, $L_g = 25$, and $\tau_0 = 0$. One can observe the basis of the three modes originating from the structural system no longer accurately predicts the system response. This model still predicts accurately the transients after the gust disturbance, while significant differences between the FOM and ROM are observed in the time interval of the gust interaction. The inclusion of an additional fluid mode in the construction of the ROM corresponding to $\lambda = -0.1393$ once again captures the dynamic response of the FOM accurately. The reason is that this particular eigenvalue corresponds to the lower frequency time constant in the exponential representation of the Küssner function.

It is possible to determine the worst-case gust by carrying out gust simulations for varying gust parameters in a systematic parametric search. The ROM in particular is exploited here to provide fast solutions for dynamic time histories. In the discrete 1-cosine gust case, the gust parameter of interest is the wavelength L_g. Figure 3.10 shows the gust response profiles for various gust wavelengths calculated using the ROM at a reduced velocity of 5. Similar series of response profiles is obtained for the flap degree-of-freedom not shown herein. The worst-case gust response in relation with the gust wavelength is attributed to a match between gust frequency and the natural frequencies of the aeroelastic system.

To demonstrate the frequency content of the aeroelastic system, Fig. 3.11 shows the frequency content of the system's response to 5 degree initial perturbations in pitch and flap at reduced velocities of 1.0, 5.0 and 6.0, respectively. The values of the reduced velocites are chosen such that they are progressively closer to the linear flutter velocity. Three observable peaks corresponds to the frequencies of the modes originating in the structural degrees-of-freedoms. From the uncoupled natural frequency ratios $\overline{\omega}_1 = 0.2$ and $\overline{\omega}_1 = 3.5$ it can be deduced that the left most peak corresponds to the bending mode followed by torsion and flap. One should note that, although the frequency peaks for torsion and flap are mostly hidden by the dominant bending mode in the frequency content of the plunge time history, they are clearly observable for the pitch and flap signals. The shift in the frequency content of the system due to a change to the reduced velocity is readily observed here. Increasing the reduced velocity closer to the linear flutter speed leads to the merge of the peaks in torsion and bending representing the dominant bending-torsion flutter.

To highlight the interaction of the gust frequency with the structural frequencies, the Fourier analysis of the gust response is shown in Fig. 3.12 at two distinct gust wavelengths (i.e. gust frequencies) of $L_g = 1$ and $L_g = 30$ for both the pitch and flap responses. It is clear that the gust input with wavelength $L_g = 30$ excites predominantly the plunge mode at frequency ratio 0.2 while the gust with wavelength $L_g = 1$ excites the coupled flap mode at frequency ratio 4.0. Thus, an increase in plunge response amplitude is expected as the gust wavelength is increased close to $L_g = 30$.

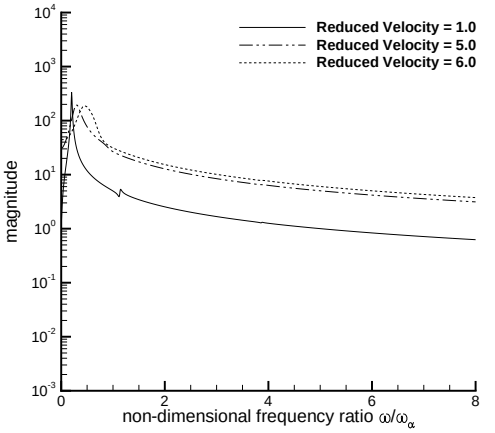

(a) Plunge history

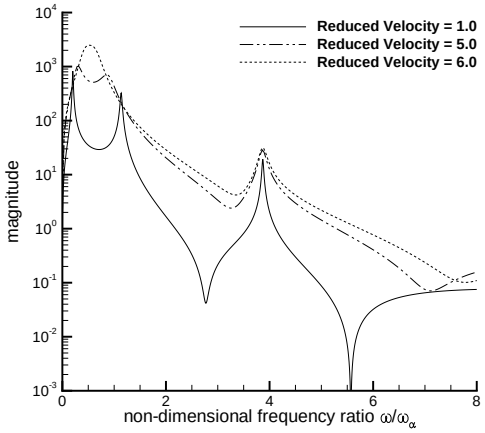

(b) Pitch history

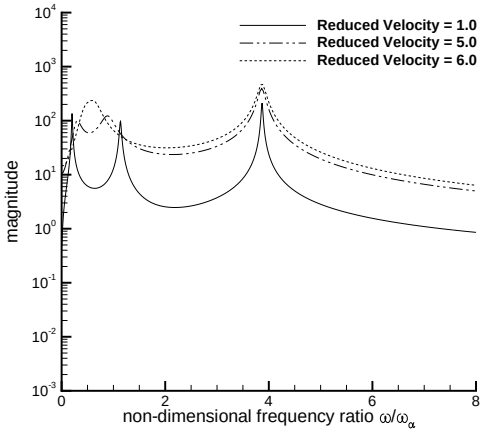

(c) Flap history

Figure 3.11: Frequency content of time responses to initial perturbations in pitch and flap

3.2.4 Limit-Cycle Oscillation and Model Reduction

Now limit-cycle oscillation behaviour is considered. For the results presented, the flap degree-of-freedom is deactivated. The structural model is hence reduced to a two degrees-of-freedom aerofoil elastically supported in plunge and pitch. This is to provide a comparable two degrees-of-freedom model in-line with the test cases reported in available literature. The structural model used for the analysis is described by the parameters $\bar{\omega}_1 = 0.2$, $\mu = 100$, $a_h = -0.5$, $x_\alpha = 0.25$ and $r_\alpha = 0.5$. While the plunge spring is linear, two different nonlinear springs in the pitch degree-of-freedom are considered. The first configuration, following Lee et al. [47], is a cubic hardening spring with $\beta_{\alpha 3} = 3$, while the second configuration, following Pettit and Beran [64], is cubic softening and quintic hardening with $\beta_{\alpha 3} = -3$ and $\beta_{\alpha 5} = 20$. No structural

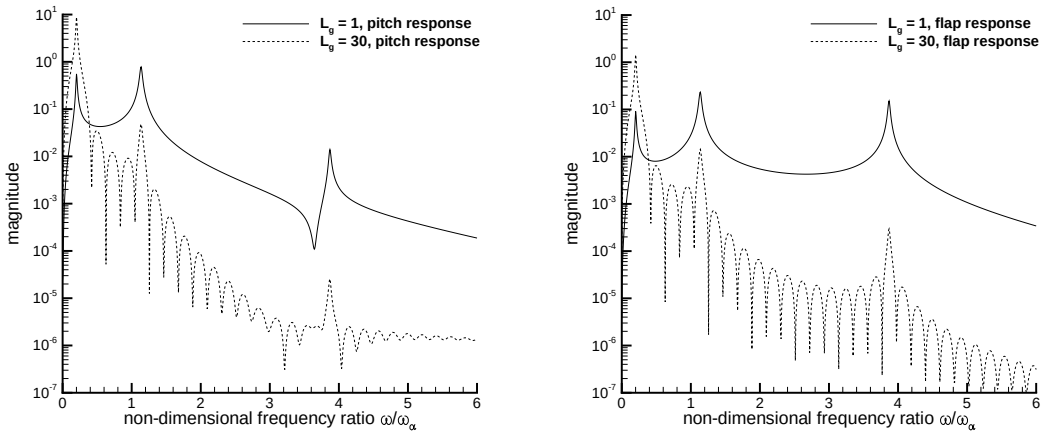

(a) Pitch history

(b) Flap history

Figure 3.12: Frequency content of time responses to gust disturbance

damping is assumed in the analysis herein. Note that up till now only the linear ROM is considered, here the focus shifts to the nonlinear ROM.

The first scenario considered here is LCO arising from a supercritical bifurcation corresponding to the case of a cubic hardening spring with $\beta_{\alpha 3} = 3$. The nonlinear ROM based both on multiple modes and the critical mode are constructed at the bifurcation point at $\bar{u}_L = 6.285$. Since the nonlinearity is cubic only, the terms up to $\boldsymbol{\mathcal{C}}$ must be evaluated in the ROM construction, while functions $\boldsymbol{\mathcal{D}}$ and $\boldsymbol{\mathcal{E}}$ are zero. Additionally, since the steady-state solution is trivial, $\boldsymbol{\mathcal{B}}$ is zero as well.

Limit-cycle oscillation induced by an initial disturbance is studied first. The reduced velocity is set to five percent above the bifurcation point and the system is excited by an initial disturbance in pitch of five degrees. Due to the nonlinear cubic hardening restoring moment in pitch, the system exhibits a stable LCO for reduced velocities above the flutter point. Figure 3.13 shows the time history of the LCO as predicted by both critical and multiple modes ROM compared with the full-order model solution. The two modes used in the construction of the multiple modes ROM originate from the structural vibration problem. Excellent agreement with the full-order solution is observed throughout. The critical mode ROM predicts the amplitude of the LCO well, although discrepancies are found during the transient response up to approximately 100 time units. Since the critical mode ROM formulation relies on information exclusively from the single critical mode, it is clear why this type of behaviour is observed. In the transition period to a steady-state limit-cycle response, the dynamics of the system are influenced by contributions from the non-critical structural mode as well until it is damped out in time. Once the steady-state limit-cycle is reached, the dynamics are dominated by the single critical mode.

A point should also be noted about the discrepancy in the initial conditions between

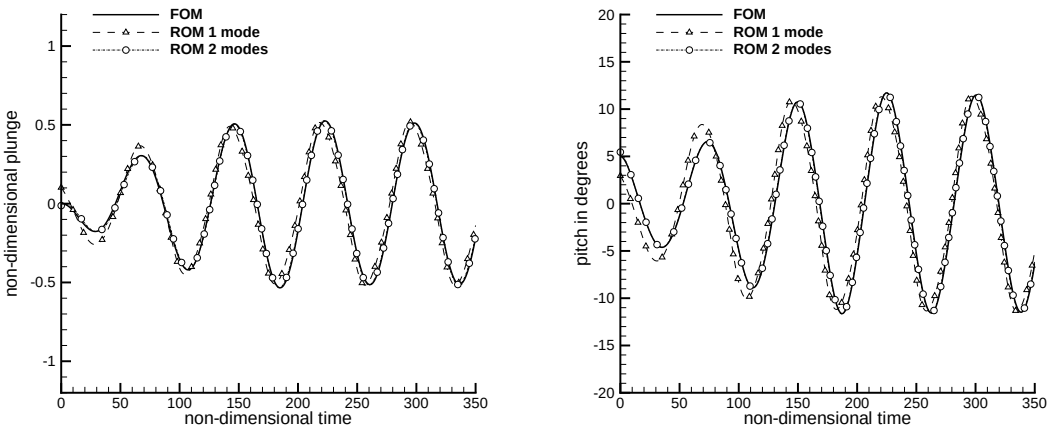

(a) plunge response

(b) pitch response

Figure 3.13: Transient leading to supercritical LCO due to initial pitch disturbance of five degrees, $\bar{u} = 6.599$

the solutions in Fig. 3.13. Specifically, in the full-order model solution the initial pitch is set to five degrees while after transformation to and from the reduced space the initial pitch obtained is about three degrees. Similar behaviour is found in the plunge degree-of-freedom. The critical mode ROM depends exclusively on the critical mode and the reduced space spanned by this single mode can not accurately represent the corresponding initial condition in physical space. Making the transformation to the reduced space with $\boldsymbol{z}(0) = \Psi^H \boldsymbol{w}(0)$ to obtain the initial condition of the reduced state variable $\boldsymbol{z}$ and back to physical space with $\boldsymbol{w}(0) = \Phi \boldsymbol{z}(0) + \bar{\Phi}\bar{\boldsymbol{z}}(0)$, information is lost and the significant difference in the initial condition is explained. If all the modes of the physical system are retained, the equation $\Phi\Psi^H + \bar{\Phi}\bar{\Psi}^H = I$ is satisfied otherwise. It is clear from Fig. 3.13 the multiple-modes ROM with two modes already provides accurate prediction of the full-order response and therefore justifies the choice of retaining just two modes.

Limit-cycle oscillation can also be induced by gust disturbance. Figure 3.14 shows the same system disturbed by a discrete 1-cosine gust as defined in Eq. (3.30) with the dimensionless parameters being gust intensity $W_0 = 0.1$, gust wavelength $L_g = 20$ and gust initial time $\tau_0 = 10$. For the construction of the multiple modes ROM the effect of including two additional modes has been assessed as only including the structural vibration modes is not sufficient for accuracy during the gust excitation. The first additional mode corresponds to the real-valued eigenvalue of $\lambda = -0.1393$ which as discussed previously, for the three degrees-of-freedom case, is the lower time constant used in the approximation of the Küssner function. This mode is demonstrated to be dominant in coupling the structural response to the gust input as discussed in Da Ronch et al. [48]. The multiple modes ROM constructed using these three modes shows good

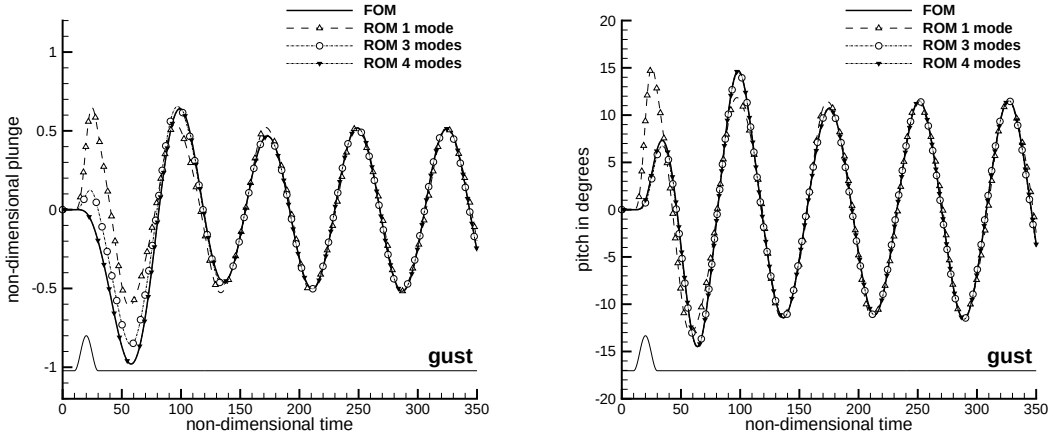

(a) plunge response (b) pitch response

Figure 3.14: Transient leading to supercritical LCO due to initial gust disturbance, $\bar{u} = 6.599$

agreement with the full-order solution. However, differences in the transient response up to 100 time units are still observed, particularly in the plunge response. It is found that this prediction is significantly improved by including an additional fourth mode of a real-valued eigenvalue $\lambda = -0.03178$ corresponding to the Wagner aerodynamic states. Its value changes with respect to the reduced velocity and can be identified as it is always close to the value of the lower time constant used in the approximation of the Wagner function. The critical mode ROM predicts the steady-state LCO well but fails during the gust disturbance. The consideration here is that the critical mode ROM lacks the gust mode and is thus unable to correctly capture the transition into the LCO.

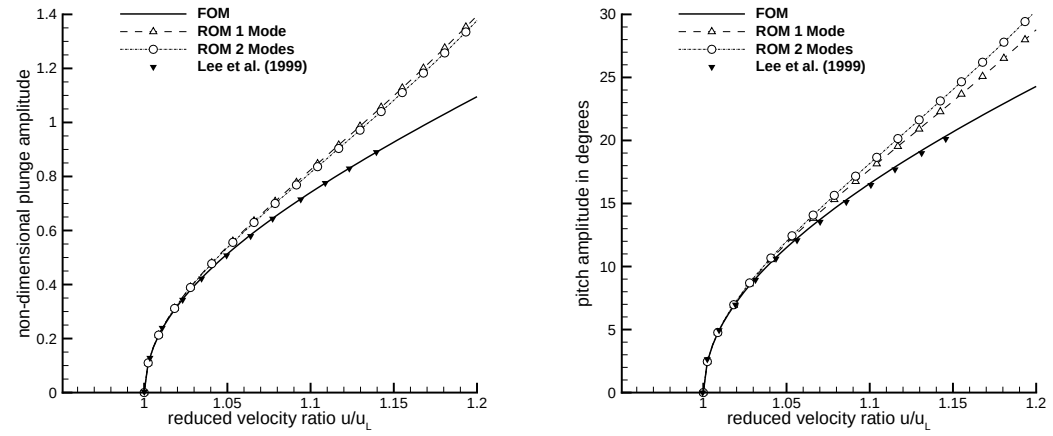

(a) plunge amplitude (b) pitch response

Figure 3.15: Supercritical LCO amplitude retaining first-order derivatives in $\bar{u}$

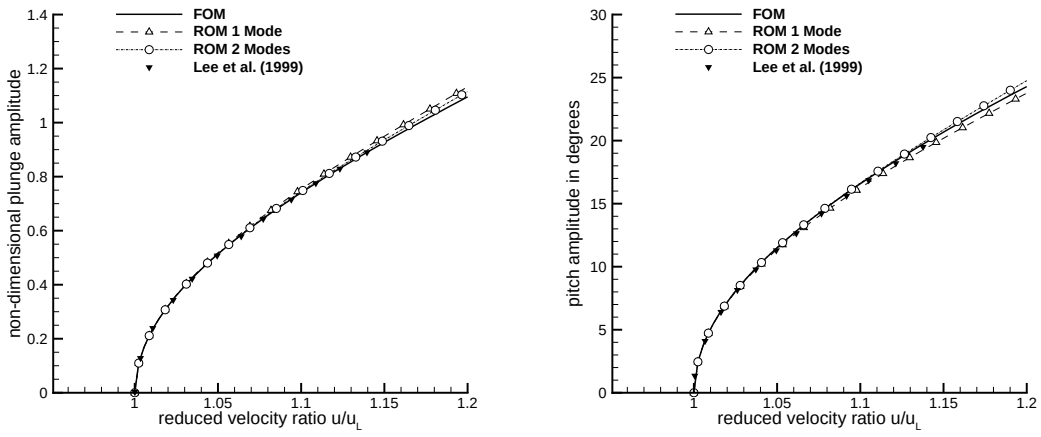

(a) plunge amplitude (b) pitch response

Figure 3.16: Supercritical LCO amplitude retaining derivatives up to third-order in $\bar{u}$

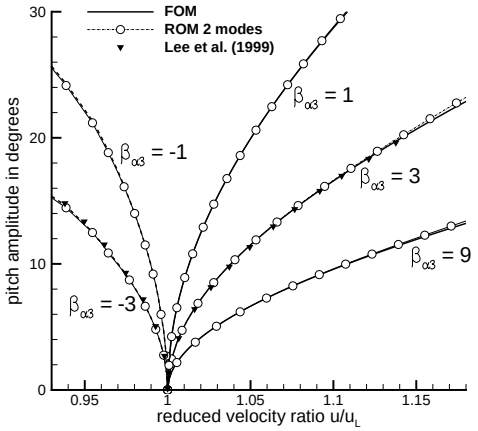

Figure 3.17: Supercritical LCO amplitudes ($\beta_{\alpha 3} > 0$) and subcritical flutter instability onset ($\beta_{\alpha 3} \leq 0$) for various values of cubic torsion coeffcient

By running a series of time histories, it is possible to trace the plots in Figs. 3.15 and 3.16 showing the evolution of the stable limit-cycle amplitude with respect to the reduced velocity. Results are compared with predictions presented in Lee et al. [47] which were obtained via full-order time domain simulation. In Fig. 3.15 the ROM construction retains only first-order derivatives in the Taylor expansion with respect to the reduced velocity, while in Fig. 3.16 every term up to third-order is included. Good agreement is observed between the different predictions of reduced models and the full-order model. In Fig. 3.15 the plunge and pitch amplitude predictions by the reduced models show generally good agreement with each other while larger amplitude discrepancies to the full-order model are observed at high flow velocities. In contrast, the amplitude predictions at high flow velocities as shown in Fig. 3.16 are in much

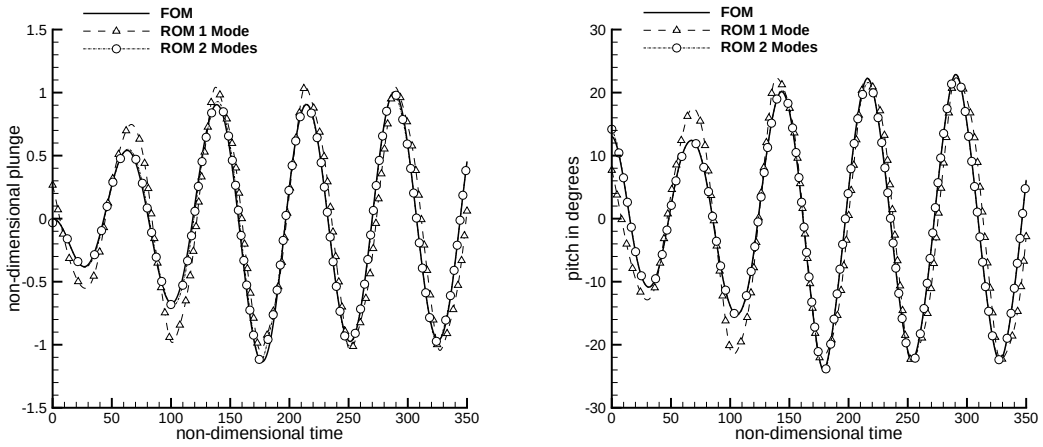

(a) plunge response

(b) pitch response

Figure 3.18: Transient leading to subcritical LCO due to initial pitch disturbance of 13 degrees, $\bar{u} = 6.097$

closer agreement with the full-order model. This demonstrates the improvement when including higher-order derivatives with respect to the reduced velocity.

As is shown by the results presented, a source of error in the reduced-order formulation is the truncation of the Taylor series expansion, while the overall quality of the prediction is improved by including higher-order derivatives with respect to the system parameter. The reduced model is also limited by the set of basis vectors used in its construction and any information lost with the excluded vectors is an inherent and necessary concession. Thus, identifying the dominant modes is critical for constructing an accurate and representative ROM.

It should also be noted that in the high velocity region the amplitudes in pitch and plunge are large, exceeding for instance 20 degrees in pitch angle. This is unrealistic in the context of the linear aerodynamic theory applied here due to the appearance of nonlinear aerodynamic phenomena such as massive boundary layer separation. However, the results presented herein are nevertheless solutions of the models used to approximate real physics.

To ensure the robustness of reduced-order modelling approach further simulations are run for additional values of the cubic coeffcient $\beta_{\alpha 3}$. Specifically negative values are considered which leads to subcritical flutter instabilities, rather than post-flutter supercritical limit-cycle responses. Figure 3.17 compares the full-order reference solutions with results from the reduced-order model based the only two structural modes and retaining derivatives up to third-order with respect to the reduced velocity. In Fig. 3.17 the subcritical flutter boundary is represented by the critical initial pitching angle $\alpha(0)$ which causes instability. All other remaining initial conditions are set to zero.

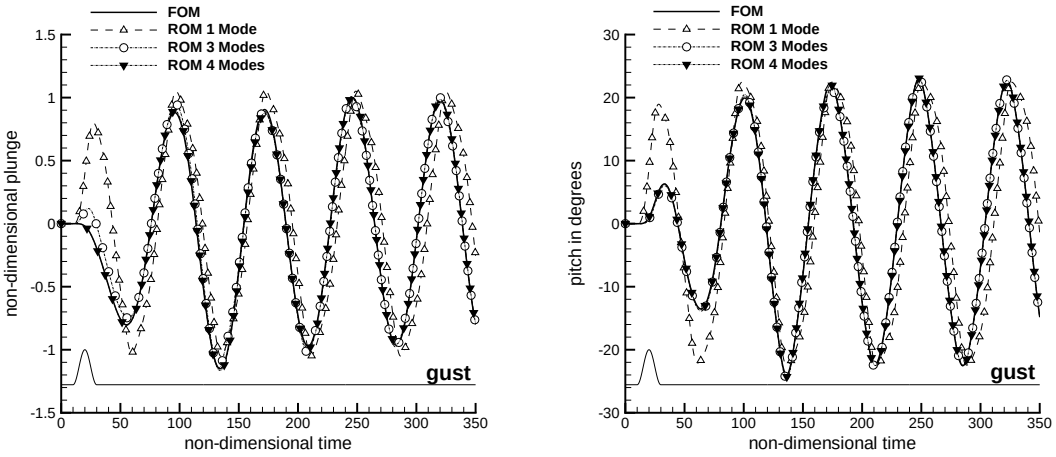

(a) plunge response

(b) pitch response

Figure 3.19: Transient leading to subcritical LCO due to initial gust disturbance, $\bar{u} = 6.097$

Subcritical limit-cycle responses corresponding to the case of a cubic softening combined with quintic hardening spring with $\beta_{\alpha 3} = -3$ and $\beta_{\alpha 5} = 20$ are considered next. The general mechanism is that the cubic softening nonlinearity contributes to a destabilizing effect, while at large amplitudes the quintic hardening nonlinearity acts to constrain the system response from diverging. In the presence of the softening nonlinearity, limit-cycle responses can occur at velocities below the linear flutter point. As above, the reduced models are constructed at the bifurcation point. Since the discrete nonlinearity now extends to quintic-order, terms up to $\boldsymbol{\mathcal{E}}$ must be evaluated. Note that functions $\boldsymbol{\mathcal{B}}$ and $\boldsymbol{\mathcal{D}}$ are zero as the equilibrum solution is trivial.

Most importantly, the reduced-order formulation is capable of predicting subcritical limit-cycle response as a consequence of extending the formulation to include up to fifth-order derivatives in the state variables. Figure 3.18 shows the transition to LCO at a reduced velocity three percent below the linear flutter point. The initial condition here is a disturbance in pitch of 13 degrees, the reason of which will be explained below. Similarly to the case of supercritical bifurcation, the modes used for the construction of the multiple modes ROM are the two complex-valued eigenmodes corresponding to the structural degrees-of-freedom. Excellent agreement with the full-order solution is found. The critical mode ROM predicts the steady-state limit-cycle response well but shows significant amplitude differences in the transition period. This is in line with the discussion for the case of supercritical bifurcation in Fig. 3.13 and due to the limited information contained in the critical mode.

As with the supercritical case, subcritical LCO can also be induced by a gust disturbance even below the flutter point. Figure 3.19 shows the system subjected to the discrete 1-Cosine gust profile with gust intensity $W_0 = 0.1$, wavelength $L_g = 20$ and

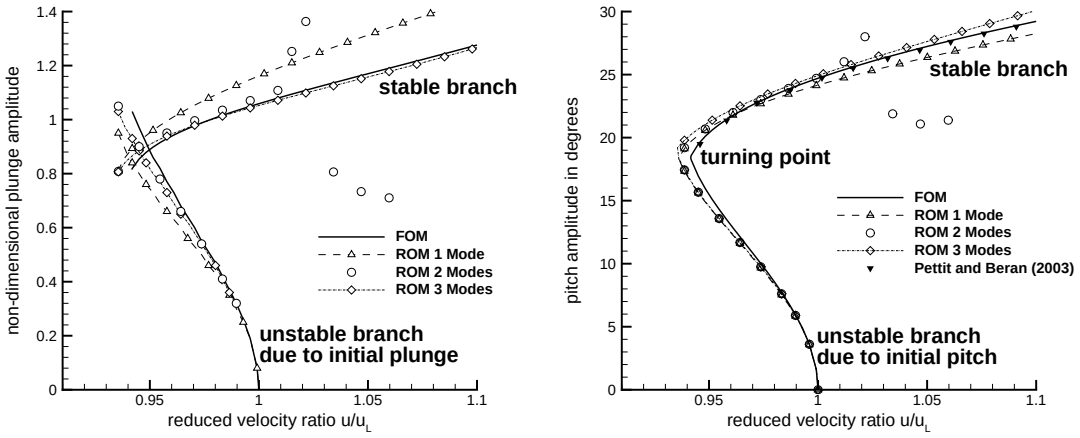

(a) plunge amplitude

(b) pitch amplitude

Figure 3.20: Subcritical LCO amplitude retaining first-order derivatives in $\bar{u}$

initial time $\tau_0 = 10$. Corresponding to the supercritical case, the same two additional modes are assessed in the prediction of the transient behaviour. The conclusion remains unchanged. The best prediction is obtained by including the fourth mode corresponding to the purely real-valued eigenvalue of $\lambda = -0.03178$. As expected, the critical mode ROM predicts the steady-state limit-cycle amplitude reasonably well but fails to accurately capture the response during the gust disturbance phase.

In the case of subcritical bifurcation the presence of the quintic hardening stiffness constrains the system at high amplitudes, and consequently, stable large amplitude LCO is observed in Figs. 3.20 and 3.21 as indicated by the characteristic stable branch. The stable limit-cycle pitch amplitude is confirmed with results presented in Pettite and Beran [64]. The stable branch extends to reduced velocities below the bifurcation point. In this region, if the system is subjected to large enough disturbances the response will jump into the stable branch. Accordingly, if the disturbances are not large enough to incite the jump, the response will decay to zero. The critical initial pitching angle and plunge deflection causing the transition to stable large amplitude LCO is highlighted by the respective, as referred to herein, unstable branch. Consequently, to obtain stable LCO response below the flutter point the initial condition required is dictated by the unstable branch. This justifies the choice of the initial pitch disturbance of 13 degrees stated above for the response obtained in Fig. 3.18. It is important to note that the stable branch is independent of the initial conditions applied.

In the following the evolution of the stable limit-cycle amplitude with respect to the reduced velocity is traced. In Fig. 3.20 the ROM construction retains first-order derivatives in the reduced velocity only, while Fig. 3.21 presents corresponding results for the ROM formulation up to third-order in the reduced velocity. The full-order solution is compared with results from three reduced models including the critical mode

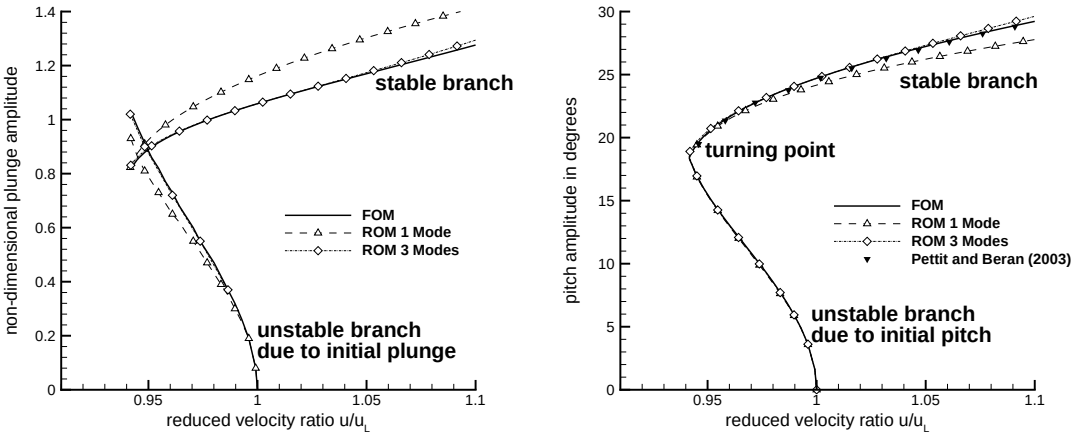

(a) plunge amplitude

(b) pitch amplitude

Figure 3.21: Subcritical LCO amplitude retaining third-order derivatives in $\bar{u}$

ROM as well as the multiple modes ROM based on two structural vibration modes only and the additional aerodynamic mode corresponding to the lower time constant in the Wagner function approximation with $\lambda = -0.03178$. This is the same mode mentioned above with its eigenvalue changing with respect to the reduced velocity. The figures permit some interesting observations.

First, the critical mode ROM does predict the subcritical limit-cycle response even though discrepancies are observed. Also the stable LCO amplitude as predicted by the multiple modes ROM, based on the two structural modes only, shows good agreement with the full-order solution except for higher values of reduced velocity. Here the multiple modes ROM based on two structural modes fails. This behaviour is not improved when including higher-order derivatives with respect to the reduced velocity and is thus not shown in Fig. 3.21. Since it is expected that the reduced model forms a better representation of the full-order system with increasing number of modes, excellent agreement with the full-order solution is found throughout when including the aerodynamic mode. Again, the importance of identifying the dominant modes is highlighted here.

Secondly, as is found for the supercritical case, including higher-order derivatives in the reduced velocity improves the ROM predictions. This can be seen clearly from the turning point where the unstable branch transitions into the stable branch. In Fig. 3.20 the turning point as predicted by the reduced models are clearly offset from the full-order solution, while in Fig. 3.21 excellent agreement between the solutions is observed. Note that for Fig. 3.21 the unstable branch in pitch as predicted by the critical mode ROM better agrees with the full-order solution compared to the unstable branch in plunge. As the critical mode originates in the pitch degree-of-freedom, it lacks information to fully represent the plunge response for the critical mode ROM. The

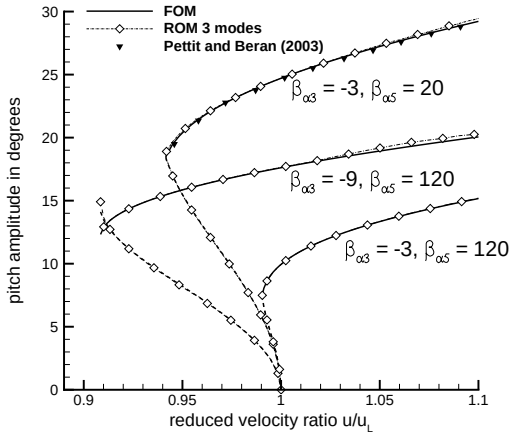

Figure 3.22: Subcritical LCO amplitudes for three sets of quintic-order stiffness

multiple modes ROM on the other hand includes both the pitch and plunge degrees-of-freedom giving an overall excellent agreement to the full-order solution.

A parameter investigation is carried out to illustrate the robustness of the modelling approach for completeness. Figure 3.22 shows two additional test cases of quintic-order nonlinearity in addition to the baseline configuration studied so far. The corresponding reduced-order model is based on the same three modes as mentioned previously and expands the residual with respect to the reduced velocity up to third-order. Good agreement with the full-order solution is found in all cases.

3.3 Summary of Typical Section Aerofoil Investigation

In this preceding section, a pitch-plunge typical aerofoil section with trailing edge flap has been formulated. The structural formulation takes into account the nonlinear spring stiffness in each structural degrees-of-freedom. The aerodynamics model utilised Wagner's function to represent the fluid forces arising from aerofoil motion due to both circulatory and non-circulatory origin. Küssner function is used to represent the aerodynamic loading arising from gust disturbances. The coupled model is recast into first-order semi-discrete form to allow for the application of nonlinear model order reduction as discussed in Chapter 2.

Numerical results first deals with linear stability analysis to determine the linear flutter point of the testcases discussed thereafter. This is achieved by solving for the eigensolution of the system's Jacobian matrix directly as the system is relatively small. The linear flutter speed is verified against established results in literature.

Further model verification is carried out by modifying the structural equations to include freeplay in the torsional degree-of-freedom. This is achieved by replacing the nonlinear spring polynomials in the original formulation by the corresponding condi-

tional form. The resulting equations of motion are integrated in time using standard second-order Runge-Kutta scheme with the inclusion of an if-condition placed in the time integration. The time domain simulations are performed based on the structural baseline model reported in established literature and excellent agreement is found.

Numerical simulations are then carried out to investigate the gust response characteristics of the linear system as well as the corresponding linear ROM. It is observed that choices of the ROM basis play an important role on the accuracy of the ROM results. Specifically, structural eigenmodes alone are not sufficient if transient behaviour during a gust encounter is to be accurately simulated by the ROM. To accurately capture the gust response, a specific fluid mode corresponding to the eigenvalue of -0.1393 is required as this arises as the lower time constant of the exponent of the approximation to the Küssner function.

In the investigation of limit-cycle oscillation arising from structural nonlinearity, the nonlinear model reduction approach illustrated in Chapter 2 is applied. The model reduction is formulated to include up to fifth-order derivatives in the Taylor expansion of the nonlinear full-order residual function. The underlying motivation is such that higher-order nonlinear behaviour of the full-order system can therefore be captured with the extended reduced model formulation. Stiffness nonlinearity is introduced into the pitch degree-of-freedom in polynomial form up to fifth order such that the system exhibits the desired limit-cycle behaviour. Including multiple modes in the basis, used for projection of the full-order system, is unnecessary in the case of a supercritical limit-cycle oscillation if interest lies in the amplitude prediction. Results using only the critical mode for model reduction are in excellent agreement with the reference solution. If transient behaviour is important however, as is the case when gust disturbance is discussed, multiple modes are required. The situation changes for subcritical limit-cycle behaviour. Even if the interest is in the amplitude only, the critical mode alone is not sufficient. While the reduced model based on the critical mode does predict the subcritical limit-cycle response, multiple modes are mandatory to resolve the discrepancy between the reduced model prediction and the full-order solution. If the gust-induced transient is important, the same conclusion as for the supercritical case can be reached. Finally, the order of expansion with respect to the parameters is important as well with higher-order formulations giving superior results.

Chapter 4

Nonlinear Beam Model

In Chapter 3 the modelling framework has been presented for an aerofoil testcase and a novel application to higher-order nonlinearity resulting in subcritical LCO has been discussed. In addition, in previous work model reduction has been applied to aerodynamics arising from computational fluid dynamics while structures were considered linear. In this work, the focus is on nonlinear structures instead, keeping the aerodynamics as simple as possible. In particular an understanding is established on how model reduction can be applied for a nonlinear structural formulation for large scale industrial aeroelastic models. The model reduction approach is of particular importance especially from an industrial perspective which deals with the cost of solving problems in large parameter spaces.

This chapter introduces a nonlinear beam model which accounts for geometrical nonlinearity associated with large deformations. The beam model is based on a geometrically exact kinematic description of a representative deformed reference line and the orientation of its corresponding cross-sections. The finite-element form of the resulting beam equations and its coupling with the unsteady strip aerodynamics model established in Chapter 3 is presented here. The exact derivation of the beam equations can be found in the indicated references.

A number of aeroelastic models are constructed using the beam code. The first is a flexible cantilever beam. This beam is coupled with unsteady potential strip aerodynamics by assigning aerofoil sections to each finite element nodal point along the beam and is representative of a slender aircraft wing. The second model is an unrestrained rigid beam which is coupled with the same unsteady aerodynamics model. This is to capture the flight-dynamic effect of a free-flying wing. The last two models are full scale large nonlinear aircraft structures based on the FFAST model. Gust response simulations are presented and the application of nonlinear model reduction for this system is demonstrated. In regards to the nonlinear model reduction, a structured guideline is presented such that the dominant modes can always be identified to construct an accuracte reduced-order model.

4.1 Formulation

Standard structural modelling in industry typically utilises the formulation in modal space given as

$$\ddot{\boldsymbol{\eta}} + C_\eta \dot{\boldsymbol{\eta}} + K_\eta \boldsymbol{\eta} = \Xi^T \boldsymbol{F}_A \tag{4.1}$$

where $\boldsymbol{\eta}$ contains a finite number of m modal amplitudes, Ξ is the matrix with 'mass normalised' structural mode shapes as columns, while K_η and C_η are the modal stiffness and damping matrices, respectively. The aerodynamic force vector is given by $\boldsymbol{F}_A$, while premultiplication with Ξ^T gives the generalised forces. This formulation is purely linear and the structural mode shapes are solved once only at the structure's reference equilibrium point with zero external forces assumed. The benefit of this procedure lies in its simplicity. The system is small in size and the size depends on the number of modes used in the modal transformation. Typically the structural model is coupled with CFD aerodynamics and the resulting system state vector takes the form of $\left[\boldsymbol{\phi}_f^T, \boldsymbol{\phi}_s^T\right]^T$ where subscripts f and s denote the fluid and structural degrees-of-freedom, respectively. Here, $\boldsymbol{\phi}_f$ has the size in the order of millions while $\boldsymbol{\phi}_s$ contains the structural modal amplitudes and has a size of less than a hundred unknowns.

In this section, the geometrically nonlinear beam formulation is used. As will be discussed in detail, the formulation is in general fully nonlinear and is given in physical space. The system is fully coupled and size is equal to the total physical degrees-of-freedom of the structural model. The benefit of this formulation is that it is fully geometrically exact. This means the formulation is more versatile and provides a more physically accurate represention of the structure. If CFD aerodynamics is used, $\boldsymbol{\phi}_f$ has the size in the order of millions while $\boldsymbol{\phi}_s$ will contain the physical degrees-of-freedom and has a size in the order of tens of thousands. Despite the large size in the nonlinear structural model, the method of model reduction presented in Chapter 2 is applied here based on identifying relevant dominant eigenmodes. This is presented in the results section hereafter.

The nonlinear beam code [42, 43] couples structural flexibility with unrestrained rigid-body motions. The descriptions of beam kinematics are geometrically exact. The equations of motion are formulated based on Hamilton's principle constructing a balance between variational expressions of internal kinetic energy density, the internal potential energy density, and the virtual work of externally applied forces. The finite-element discretised form of the equations of motion for a discrete unrestained beam is given as follows

$$M_t\left(\boldsymbol{X}_e\right)\begin{pmatrix}\ddot{\boldsymbol{X}}_e\\ \ddot{\boldsymbol{X}}_r\end{pmatrix} + \boldsymbol{Q}_{\text{gyr}}\left(\boldsymbol{X}_e, \dot{\boldsymbol{X}}_e, \dot{\boldsymbol{X}}_r\right) + \boldsymbol{Q}_{\text{stiff}}\left(\boldsymbol{X}_e\right) = \boldsymbol{Q}_{\text{ext}}\left(\boldsymbol{X}_e, \dot{\boldsymbol{X}}_e, \dot{\boldsymbol{X}}_r, \boldsymbol{\zeta}\right) \tag{4.2}$$

Here, the terms $\boldsymbol{X}_e$, $\boldsymbol{X}_r$ and $\boldsymbol{\zeta}$ denote the vector of nodal deformation displacements

and rotations, the vector of rigid-body displacements and rotations and the vector of quaternion states defining the beam element orientation, respectively. The tangent mass matrix couples structural flexibility and rigid-body degrees of freedom and is given by

$$M_t = \begin{pmatrix} M^{ee} & M^{er} \\ M^{re} & M^{rr} \end{pmatrix} \tag{4.3}$$

with superscripts e and r denoting the elastic and rigid-body properties, respectively. The exact evaluations of the matrix elements can be found in [43]. The gyroscopic, elastic and external forces are also partitioned into elastic and rigid-body contributions, expressed as

$$\boldsymbol{Q}_{\text{gyr}} = \begin{pmatrix} Q^e_{\text{gyr}} \\ Q^r_{\text{gyr}} \end{pmatrix}, \quad \boldsymbol{Q}_{\text{stiff}} = \begin{pmatrix} Q^e_{\text{stiff}} \\ 0 \end{pmatrix} \quad \text{and} \quad \boldsymbol{Q}_{\text{ext}} = \begin{pmatrix} Q^e_{\text{ext}} \\ Q^r_{\text{ext}} \end{pmatrix} \tag{4.4}$$

where the expression for the external forces are general and are typically functions of the system states. This is characteristic of, for example, aerodynamic forces or externally applied follower forces both of which are dependent on the structure's geometry.

This second order equation is extended by the first order quaternion dynamics of the attitude propagation describing the orientation of the beam in free space

$$\dot{\boldsymbol{\zeta}} = -\frac{1}{2}\Omega\boldsymbol{\zeta} \tag{4.5}$$

where

$$\boldsymbol{\zeta} = \begin{pmatrix} \zeta_0 \\ \zeta_1 \\ \zeta_2 \\ \zeta_3 \end{pmatrix} \text{ and } \quad \Omega = \begin{pmatrix} 0 & \omega_x & \omega_y & \omega_z \\ -\omega_x & 0 & -\omega_z & \omega_y \\ -\omega_y & \omega_z & 0 & -\omega_x \\ -\omega_z & -\omega_y & \omega_x & 0 \end{pmatrix} \tag{4.6}$$

Here ω_i for $i = x, y, z$ denotes the i-th component of the body's angular velocity vector.

Equation (4.2) is linearised in order to facilitate Newton-Raphson iterative solution for a Newmark-β integration scheme [65]. The Newmark method is suitable as the structure consist of a group of concentrated masses connected by flexible beam elements. Linearisation around the equilibrium gives the incremental form of the finite element equation of motion as

$$M_t\left(\boldsymbol{X}_e\right)\begin{pmatrix} \ddot{\boldsymbol{x}}_e \\ \ddot{\boldsymbol{x}}_r \end{pmatrix} + C\left(\boldsymbol{X}_e, \dot{\boldsymbol{X}}_e, \dot{\boldsymbol{X}}_r\right)\begin{pmatrix} \dot{\boldsymbol{x}}_e \\ \dot{\boldsymbol{x}}_r \end{pmatrix} + K\left(\boldsymbol{X}_e\right)\begin{pmatrix} \boldsymbol{x}_e \\ 0 \end{pmatrix} = \Delta\boldsymbol{Q}_{\text{ext}}\left(\boldsymbol{x}_e, \dot{\boldsymbol{x}}_e, \dot{\boldsymbol{x}}_r, \Delta\boldsymbol{\zeta}\right) \tag{4.7}$$

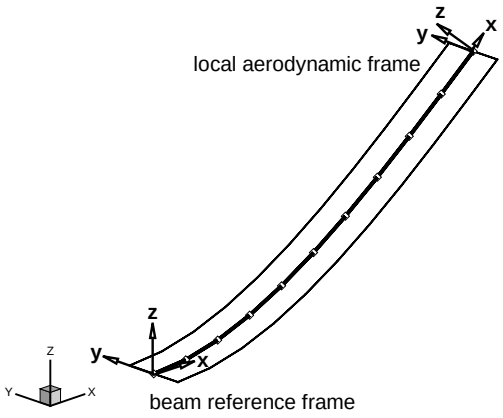

Figure 4.1: General reference frames on a typical beam

This leads to the nonlinear system mass, damping and stiffness matrices

$$M_t\left(\boldsymbol{X}_e\right) = \begin{pmatrix} M^{ee} & M^{er} \\ M^{re} & M^{rr} \end{pmatrix}, \quad C\left(\boldsymbol{X}_e, \dot{\boldsymbol{X}}_e, \dot{\boldsymbol{X}}_r\right) = \begin{pmatrix} C^{ee} & C^{er} \\ C^{re} & C^{rr} \end{pmatrix}, \quad K\left(\boldsymbol{X}_e\right) = \begin{pmatrix} K^{ee} & 0 \\ K^{re} & 0 \end{pmatrix} \tag{4.8}$$

the exact evaluations of which can be found in [43].

4.1.1 Flexible Cantilever Beam

The formulation of the beam code is general and independent of the type of external forcing. Therefore it can be extended to model slender wing structures. In this model construction, the beam code forms a cantilever representation of a slender wing. This structural model is then coupled with two-dimensional unsteady linear strip aerodynamics at each finite element nodal section along the span of the beam. The aerodynamic forces are given by the theory already presented in Chapter 3 using the functions of Wagner and Küssner to model aerodynamic forces due to motion and gust, respectively. The system is defined with respect to a fixed 'beam' reference frame located at the clamped root of the wing (shown in Fig. 4.1) with x-axis along the span of the wing, the z-axis pointing up and the y-axis aligned with the streamwise direction. Each node j in the finite element model corresponds to a 2D aerofoil section in the y-z plane and has corresponding sectional degrees-of-freedom defined with respect to the 'beam' frame as

$$\boldsymbol{x}_e^{(j)} = \left[v_{sx}, v_{sy}, v_{sz}, \theta_{sx}, \theta_{sy}, \theta_{sz}\right]^T \tag{4.9}$$

Here, v_{sx}, v_{sy} and v_{sz} denotes translational degrees-of-freedom, while, θ_{sx}, θ_{sy} and θ_{sz} are the rotational degrees-of-freedom. From Eq. (4.7) the global finite element equations

are obtained by using only the flexible dynamics,

$$M_s^{(j)}\left(\boldsymbol{x}_e\right)\ddot{\boldsymbol{x}}_e + C_s^{(j)}\left(\boldsymbol{x}_e, \dot{\boldsymbol{x}}_e, \dot{\boldsymbol{x}}_r\right)\dot{\boldsymbol{x}}_e + K_s^{(j)}\left(\boldsymbol{x}_e\right)\boldsymbol{x}_e = \boldsymbol{F}_A^{(j)} \tag{4.10}$$

where $M_s = M^{ee}$, $C_s = C^{ee}$, $K_s = K^{ee}$ and $\boldsymbol{F}_A = Q^e_{\text{ext}}$.

Based on the aerodynamic theory presented in Chapter 3 the aerodynamic force vector $\boldsymbol{F}_A$ depends on the sectional degrees-of-freedom v_{sz} and θ_{sx} for each node. Since each nodal section has variable sectional torsion there exists a local 'aerodynamic' frame corresponding to each aerofoil section along the beam span. The approach here is to rotate the aerodynamic forces from their respective frames to the 'beam' reference frame. The aerodynamic force acting on the j-th nodal section in this local aerodynamic frame is

$$\boldsymbol{F}_A^{(j)A} = \left[0, -L^{(j)}, 0, 0, 0, M^{(j)}\right]^T \tag{4.11}$$

where the superscript A indicates local aerodynamic frame. Equation (4.11) is now expressed in matrix-vector form

$$\boldsymbol{F}_A^{(j)A} = M_a^{(j)A}\ddot{\boldsymbol{x}}_e^{(j)A} + C_a^{(j)A}\dot{\boldsymbol{x}}_e^{(j)A} + K_a^{(j)A}\boldsymbol{x}_e^{(j)A} + D_a^{(j)A}\boldsymbol{w}_f^{(j)} + B_c^{(j)}\boldsymbol{u}_c^{(j)} + \boldsymbol{B}_g^{(j)}W_g \tag{4.12}$$

where $M_a^{(j)}$, $C_a^{(j)}$ and $K_a^{(j)}$ are the local aerodynamic mass, damping, and stiffness matrices, while the matrix $D_a^{(j)}$ relates the structural degrees-of-freedom to the local augmented aerodynamic states. The matrix $B_c^{(j)}$ is for any optional trailing-edge flap across beam elements for control and $\boldsymbol{B}_g^{(j)}$ is a vector relating to external gust disturbance which is assumed constant across the beam model. The non-zero components of these matrices are given in Appendix C.2. Furthermore, within the aerodynamic matrices of Eq. (4.12) are a large number of constant terms for a given structural geometry which only need to be computed once. These are given explicitly in Appendix C.2 as well.

While the approximation of localising the distributed aerodynamic force between two consecutive aerofoil sections, delimited between node $j-1$ and j into the j-th node is crude, it is assumed reasonable for increasing number of structural elements.

To complete the description of 2D unsteady potential strip aerodynamics the dynamics of the augmented aerodynamic states must be evaluated for every finite element nodal aerofoil section along the beam span. For the j-th node this is given in matrix-vector form, following Eq. (3.24) for the two-dimensional aerofoil,

$$\dot{\boldsymbol{w}}_f^{(j)} = A_{ff}^{(j)}\boldsymbol{w}_f^{(j)} + A_{fx}^{(j)}\boldsymbol{x}_e^{(j)A} + A_{fc}^{(j)}\boldsymbol{u}_c^{(j)} + A_{fg}^{(j)}W_g \tag{4.13}$$

The non-zero components of these terms are given in Appendix C.2.

The expressions given in Eqs. (4.12) and (4.13) are formulated based on a vector

of structural degrees-of-freedom defined in the 'aerodynamic' reference frame $\boldsymbol{x}_e^{(j)A}$. In order to form the global system equations of motion, a coordinate transformation has to be performed to transfer the structural flexible degrees-of-freedom in the fixed 'beam' reference frame. This is accomplished by the transformation

$$\boldsymbol{x}_e^{(j)A} = T\boldsymbol{x}_e^{(j)B} \tag{4.14}$$

where superscript B indicates the beam reference frame. The transformation matrix T is a function of the local sectional torsional rotation θ_x and is given by

$$T = \begin{pmatrix} R & 0 \\ 0 & R \end{pmatrix} \tag{4.15}$$

where

$$R = \begin{pmatrix} 0 & -\cos(\alpha_{\text{att}}) & -\sin(\alpha_{\text{att}}) \\ 0 & +\sin(\alpha_{\text{att}}) & -\cos(\alpha_{\text{att}}) \\ 1 & 0 & 0 \end{pmatrix} \tag{4.16}$$

and the angle of attack of the nodal aerofoil section is evaluated as $\alpha_{\text{att}} = \alpha_0 + \theta_x$, which is the sum of pre-twist α_0 and the sectional deformation in torsion θ_x.

Equation (4.12) can now be entirely expressed with respect to the fixed beam frame by substituting Eq. (4.14) and premultiplying by T^T.

$$\boldsymbol{F}_A^{(j)} = \tilde{M}_a^{(j)}\ddot{\boldsymbol{x}}_e^{(j)B} + \tilde{C}_a^{(j)}\dot{\boldsymbol{x}}_e^{(j)B} + \tilde{K}_a^{(j)}\boldsymbol{x}_e^{(j)B} + \tilde{D}_a^{(j)}\boldsymbol{w}_f^{(j)} + \tilde{B}_c^{(j)}\boldsymbol{u}_c^{(j)} + \tilde{B}_g^{(j)}W_g \tag{4.17}$$

where

$$\begin{aligned} \tilde{M}_a^{(j)} &= T^T M_a^{(j)} T & \tilde{C}_a^{(j)} &= T^T C_a^{(j)} T & \tilde{K}_a^{(j)} &= T^T K_a^{(j)} T \\ \tilde{D}_a^{(j)} &= T^T D_a^{(j)} T & \tilde{B}_c^{(j)} &= T^T B_c^{(j)} & \tilde{B}_g^{(j)} &= T^T B_g^{(j)} \end{aligned} \tag{4.18}$$

This transformation must also be made to the vector of structural unknowns in Eq. (4.13), leading to

$$\dot{\boldsymbol{w}}_f^{(j)} = A_{ff}^{(j)}\boldsymbol{w}_f^{(j)} + \tilde{A}_{fx}^{(j)}\boldsymbol{x}_e^{(j)B} + A_{fc}^{(j)}\boldsymbol{u}_c^{(j)} + A_{fg}^{(j)}W_g \tag{4.19}$$

where

$$\tilde{A}_{fx}^{(j)} = A_{fx}^{(j)}T \tag{4.20}$$

Equation (4.17) gives the nodal aerodynamic force in the fixed beam frame in matrix-vector format and is assembled for all the nodal points into a global matrix-vector form. This is then substituted as $\boldsymbol{F}_A$ in Eq. (4.10) to form the global equations

of motion

$$\tilde{M}\ddot{\boldsymbol{x}}_e^B + \tilde{C}\dot{\boldsymbol{x}}_e^B + \tilde{K}\boldsymbol{x}_e^B = \tilde{D}_a\boldsymbol{w}_f + \tilde{B}_c\boldsymbol{u}_c + \tilde{B}_g W_g \tag{4.21}$$

The matrices $\tilde{M}$, $\tilde{C}$ and $\tilde{K}$ are the total system mass, damping and stiffness matrices which combine both structural dynamics and aerodynamic contributions

$$\begin{aligned}\tilde{M} &= M_s - \tilde{M}_a \\ \tilde{C} &= C_s - \tilde{C}_a \\ \tilde{K} &= K_s - \tilde{K}_a\end{aligned} \tag{4.22}$$

Equations (4.19) and (4.21) form the final coupled second and first order equations governing the dynamics of the nonlinear aeroelastic system. This system of equations can be solved by various time integration schemes. Here an implicit nonlinear Newmark-β scheme [66] is implemented. As discussed previously, the Newmark-β method is suitable as the structure consist of a group of concentrated masses connected by flexible beam elements. Here, the Newmark-β method allows Eqs. (4.19) and (4.21) to be solved directly.

For the purpose of model reduction the equations of motion must be recast into first-order ordinary differential equation form. This is done by introducing the new state vector $\boldsymbol{V} = \left[\boldsymbol{x}_e^{BT}, \dot{\boldsymbol{x}}_e^{BT}, \boldsymbol{w}_f^T\right]^T$ to obtain the corresponding nonlinear residual $\boldsymbol{R}$ as

$$\boldsymbol{R}(\boldsymbol{V}, U, W_g) = A_N(U)\,\boldsymbol{V} + \boldsymbol{b}_g W_g + \boldsymbol{b}_c\boldsymbol{u}_c \tag{4.23}$$

The matrix A_N is defined as

$$A_N = \begin{pmatrix} 0 & I & 0 \\ -\tilde{M}^{-1}\tilde{K} & -\tilde{M}^{-1}\tilde{C} & A_{\dot{x}f} \\ \tilde{A}_{fx} & 0 & A_{ff} \end{pmatrix} \tag{4.24}$$

where the matrix block A_{ff} is the Jacobian matrix of the equations in Eq. (4.13) with respect to the fluid unknowns, while the blocks $A_{\dot{x}f} = \tilde{M}^{-1}\tilde{D}_a$ and A_{fx} couple the structural equation to the fluid dynamics. The vectors $\boldsymbol{b}_g$ and $\boldsymbol{b}_c$ are given by

$$\boldsymbol{b}_g = \begin{pmatrix} 0 \\ -M^{-1}\tilde{B}_g \\ A_{fg} \end{pmatrix} \quad \text{and} \quad \boldsymbol{b}_c = \begin{pmatrix} 0 \\ -M^{-1}\tilde{B}_c \\ A_{fc} \end{pmatrix} \tag{4.25}$$

and denote contributions from gust disturbance and control inputs, respectively. Equation (4.23) takes the form of Eq. (2.2) in Chapter 2 and is the starting point for model reduction.

4.1.2 Rigid Free-Flight Beam

The beam code allows for the modelling of rigid-body dynamics and this enables the model construction for a free-flying wing. This model formulation forms the starting point to the inclusion of flight dynamic effects using the nonlinear beam code. In the model presented here, a rigid beam is created and is unrestrained in free space. The finite element beam equation given in Eq. (4.7) is reduced to purely the rigid-body dynamics part

$$M_s \ddot{\boldsymbol{x}}_r + C_s \dot{\boldsymbol{x}}_r = \boldsymbol{F}_A \tag{4.26}$$

where the mass and damping matrices become the rigid-body dynamic contributions

$$M_s = M^{rr} \quad \text{and} \quad C_s = C^{rr} \tag{4.27}$$

Since the beam is unrestrained and rigid-body dynamics apply, this second order equation must be extended by the linear dynamics of the quaternion states describing the orientation of the beam given in Eq. (4.5).

The unsteady aerodynamic model described in the previous section is dependent purely on the motion of the nodal aerofoil sections and makes no distinction between whether this motion is due to structural deformation or, in this case, rigid-body displacements and rotations. This means that the formulation of the aerodynamics is identical to the previous case in Eq. (4.12) with the only exception that the sectional deformation degrees-of-freedom are replaced by equivalent rigid-body ones. One needs to replace the state vector $\boldsymbol{x}_e^{(j)}$ with the vector of rigid-body degrees-of-freedom associated with the j-th nodal aerofoil section.

$$\boldsymbol{x}_r^{(j)} = (v_{rx}, v_{ry}, v_{rz}, \theta_{rx}, \theta_{ry}, \theta_{rz})^T \tag{4.28}$$

The identical formulation steps follow. The resulting nodal aerodynamic force vector defined with respect to the beam frame is given by

$$\boldsymbol{F}_A^{(j)} = \tilde{M}_a^{(j)} \ddot{\boldsymbol{x}}_r^{(j)} + \tilde{C}_a^{(j)} \dot{\boldsymbol{x}}_r^{(j)} + \tilde{K}_a^{(j)} \boldsymbol{x}_r^{(j)} + \tilde{D}_a^{(j)} \boldsymbol{w}_f^{(j)} + \tilde{B}_c^{(j)} \boldsymbol{u}_c^{(j)} + \tilde{B}_g^{(j)} W_g \tag{4.29}$$

This equation is analogous to Eq. (4.17) with $\boldsymbol{x}_e$ replaced by corresponding $\boldsymbol{x}_r$. It is important to note that the beam is rigid without elastic deformation, and therefore, no local 'aerodynamic' frame of reference is defined. In the evaluation of the matrices in Eq. (4.29) the R sub-matrix block of the transformation matrix T in Eqs. (4.15) and (4.16) becomes an identity matrix.

The augmented aerodynamic states are now defined with respect to the rigid-body degrees-of-freedom

$$\dot{\boldsymbol{w}}_f^{(j)} = A_{ff}^{(j)}\boldsymbol{w}_f^{(j)} + \tilde{A}_{fx}^{(j)}\boldsymbol{x}_r^{(j)} + A_{fc}^{(j)}\boldsymbol{u}_c^{(j)} + A_{fg}^{(j)}W_g \tag{4.30}$$

The global equations of motion are

$$\tilde{M}\ddot{\boldsymbol{x}}_r^B + \tilde{C}\dot{\boldsymbol{x}}_r^B + \tilde{K}\boldsymbol{x}_r^B = \tilde{D}_a\boldsymbol{w}_f + \tilde{B}_c\boldsymbol{u}_c + \tilde{B}_g W_g \tag{4.31}$$

The matrices $\tilde{M}$, $\tilde{C}$ and $\tilde{K}$ now take the following form with no structural stiffness or damping

$$\begin{aligned}\tilde{M} &= M_s - \tilde{M}_a \\ \tilde{C} &= -\tilde{C}_a \\ \tilde{K} &= -\tilde{K}_a\end{aligned} \tag{4.32}$$

Finally, the equations of motion is recast into first-order ordinary differential form by introducing the new state vector $\boldsymbol{V} = \left[\boldsymbol{x}_r^T, \dot{\boldsymbol{x}}_r^T, \boldsymbol{w}_f^T\right]^T$ similar to Eqs. (4.23) to (4.25). The corresponding nonlinear residual takes the exact form of Eq. (4.23).

4.2 Results

This section presents the numerical results for a series of investigations on various large scale structural models constructed using the nonlinear beam framework. First, a fully static cantilever problem is solved and comparison is made with results from NASTRAN for numerical validation. Then a restrained aeroelastic problem is solved for the cantilever beam coupled with linear aerodynamics for gust response. This model is based on the formulation given in Section 4.1.1. Next, a rigid-body dynamic problems is modelled for an unrestrained rigid beam coupled with linear aerodynamics. This is based on the formulation detailed in Section 4.1.2. Finally, the cantilever model approach is extended to the full scale FFAST aircraft and its isolated wing as described in Section 4.2.4. Gust response simulations are investigated with the aim of studying the capability of the reduced-order model constructed for a large full scale civil aircraft. The wing bending moment calculations are presented in Section 4.2.5.

4.2.1 Static Flexible Structure-Only Problem

The beam code has been tested and validated extensively, in particular, against the well established commercial finite element code SAMCEF details of which can be found in [43]. Another test case is presented here to build confidence in the formulation and for the sake of completeness.

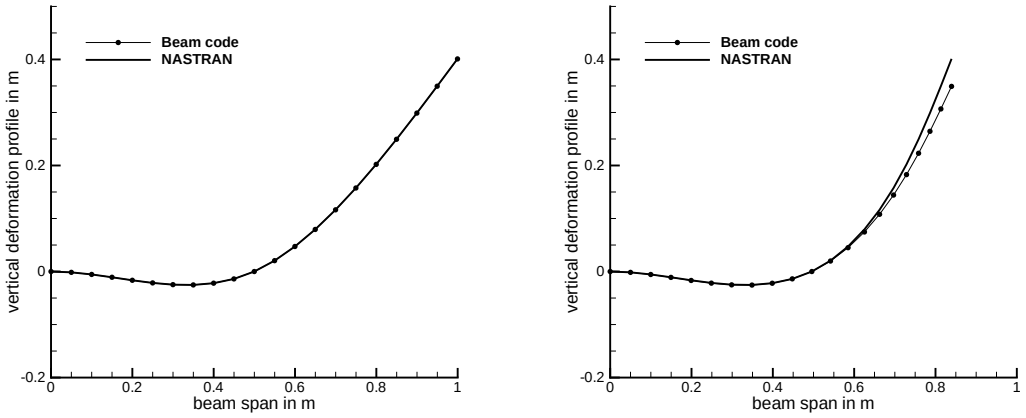

(a) linear (b) nonlinear

Figure 4.2: Static cantilever deflection comparison against NASTRAN

A simple static cantilever model test case is presented here for comparison against NASTRAN in a purely structural problem. The cantilever beam is constructed in the beam code using 20 beam two-noded elements enforcing a standard cantilever clamped boundary condition at the root structural node.

In this purely static problem, the governing equations given by Eq. (4.10) simplifies to the following form where $\boldsymbol{F}_S$ is a constant dead load

$$K_s\left(\boldsymbol{x}_e\right)\boldsymbol{x}_e = \boldsymbol{F}_S \tag{4.33}$$

The comparative NASTRAN model is constructed with 20 CBAR elements enforcing the same cantilever boundary condition. The beam length is 1 m with constant square cross-section of 0.028 m^2. The material's Young's Modulus is 7.1E+08 Nm^{-2}, the Poisson's ratio is 0.33 and the material density is 2.703E+04 kgm^{-3}.

The central node of the beam model at 50% span is restrained by a support by enforcing a large stiffness value in the specific element of the stiffness matrices in both the beam code and NASTRAN. The value is a hundred times larger than the homogeneous Young's Modulus generating a very large stiffness specifically for the central node. A direct loading of 200 N is applied vertically up at the free end of the beam. Results are calculated for the static deformation of the beam comparing both linear structural models between the beam code and NASTRAN as well as nonlinear models. For the linear structural model K_s is evaluated once based on the original undeformed configuration and assumed constant throughout the static deformation process. While, for the nonlinear case, a Newton iterative process re-evaluates the stiffness matrix until convergence.

Figure 4.2 shows the comparison of the deformation profile obtained. In the linear

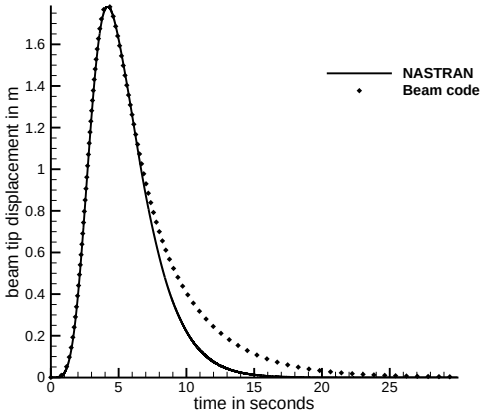

Figure 4.3: Cantilever wing tip gust response

case, the solution form an accurate match. In the nonlinear case, minor deviations between the solutions occur towards the free-end of the beam where relatively larger displacements occur for the NASTRAN results. This difference is attributed to difference in the nonlinear structural models implemented in the beam code and NASTRAN. The nonlinear structural model in NASTRAN is specified using the large displacement option.

4.2.2 Restrained Flexible Aeroelastic Problem

An aeroelastic system for a slender cantilever wing model is constructed for the calculation of gust response. This model is based on the formulation described by Eqs. (4.19) and (4.21).

The model is compared with an equivalent one in NASTRAN. The beam has a length of 16 m with a square cross-section of 0.28 m. The homogeneous Young's Modulus and Poisson's ratio are $7.1\text{E}+08$ Nm^{-2} and 0.33, respectively. The material density is $2.703\text{E}+03$ Nm^{-3}. In terms of the finite element discretization, 16 beam elements are used in the beam code and correspondingly 16 CBAR elements in NASTRAN.

The flow speed is 10 ms^{-1} and the gust model is the standardised 1-cos profile defined now in dimensional form

$$W_g(t) = \frac{W_0}{2}\left(1 - \cos\left(2\pi {L_g}^{-1}(t - t_0)\right)\right) \tag{4.34}$$

with intensity $W_0 = 0.08$ ms^{-1}, length $L_g = 40$ m and initial time $t_0 = 0$ s. Since NASTRAN does not feature a strip aerodynamics model for transient response analysis in its aeroelastic solution sequences, the aerodynamic model in NASTRAN is formed by doublet-lattice method (DLM).

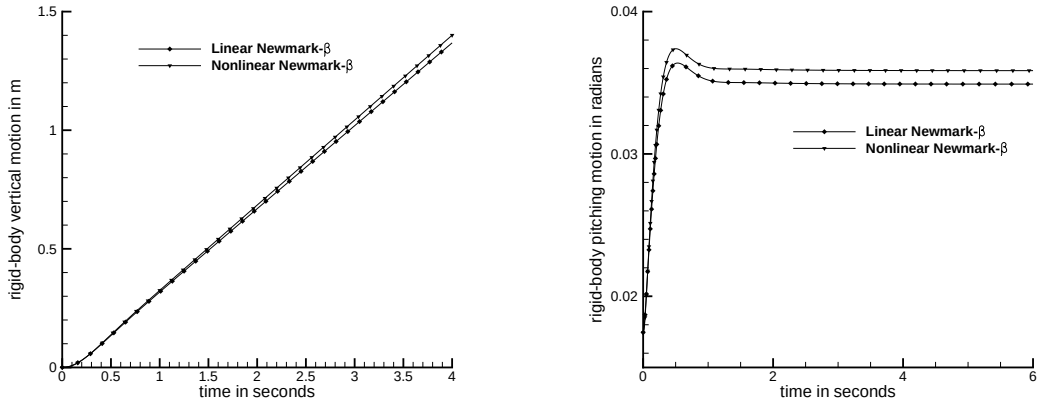

(a) rigid-body vertical motion

(b) rigid-body pitching motion

Figure 4.4: Dynamic response to initial one degree rigid-body pitch

Figure 4.3 shows the dynamic history comparison of the beam tip during the gust interaction. The solution shows an accurate match within the interval of the gust disturbance and the maximum amplitude of the deflection shows exact agreement with NASTRAN. Minor deviations occur in the transients after the gust disturbance, and this can be attributed to different wake models in the two aerodynamic models.

4.2.3 Unrestrained Rigid Free-Flight Problem

In this section, a rigid flying wing modelled based on the rigid-body dynamics formulation presented in Section 4.1.2, is investigated. The coupled Eqs. (4.5), (4.26) and (4.30) are integrated in time using both linear and nonlinear Newmark-β scheme [66]. The rigid flying wing is simulated in dynamic response to an initial perturbation in rigid-body pitching and also to a discrete 1-cos gust disturbance.

Figure 4.4 shows the response history of the rigid beam's reference point at the centre of the beam in vertical motion as well as pitching about the span-wise axis. After the initial disturbance the wing settles into a steady state of constant velocity in the vertical motion and a constant pitching angle of approximately 2 degrees. Both motions contribute to the effective angle of attack in the unsteady aerodynamic formulation and the sum of the two at steady state amounts to zero; the effective lift is zero at steady state.

Figure 4.5 shows the dynamic response of the wing to a discrete 1-cos gust disturbance from Eq. (4.34). The gust input is specified with $W_0 = 0.08$ ms^{-1}, $L_g = 40$ m, and $t_0 = 0$ s. The vertical displacement of the rigid wings shows an effective step change at steady state after the disturbance period of the gust while the rigid-body pitching returns to zero at steady-state. Once again, at the steady-state the effective angle of attack is zero meaning no lift force.

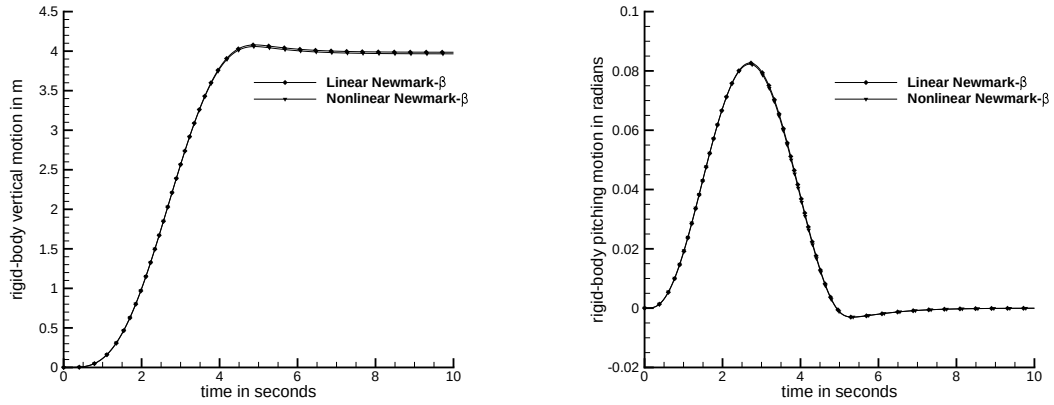

(a) rigid-body vertical motion

(b) rigid-body pitching motion

Figure 4.5: Dynamic response to initial 1-cosine gust

4.2.4 FFAST Wing and Aircraft

Based on the approach presented in Section 4.1.1, the beam code is used to construct the beam-stick model of the full scale FFAST aircraft shown in Fig. 4.6. The aircraft here is restrained at the wing root connection to the fuselage and so Eq. (4.10) is used to represent the full-order structural model. The nonlinear beam elements are utilised to represent the wings, fuselage and tail plane of the aircraft. This model is constructed by hand by extracting the relevant structural properties of each beam elements from the FFAST aircraft's original NASTRAN input deck. The beam-stick model consists of 11 elements along the fuselage centre-line, 11 elements for each main wing, and 8 elements per lifting surface at the tail. Both the fuselage and wings vary in geometric properties along their respective lengths. The entire structure consists of 59 unconstrained nodes and has a total of 1180 degrees-of-freedom when coupled with the linear aerodynamc theory as presented in Chapter 3. Based on the full aircraft structural model, the isolated FFAST wing model (shown in Fig. 4.7) is obtained by taking one of the wings and clamping the structure at the wing root. The isolated wing consists of 11 structural nodes with a total of 220 degrees-of-freedom. The important structural parameters of the FFAST aircraft model are summarised in Tab. 4.1

Similarly to what is accomplished in the cantilever wing model, linear aerodynamic strip theory is coupled with the FFAST aircraft structural model. Here specifically, each structural node along the wings is assumed to coincide with a 2D aerofoil section. Therefore, the aerodynamic forces acting on each aerofoil directly translate to the structural nodes.

The aerodynamic strip system is defined with respect to the 'beam' reference frame located at the wing root with the x-axis pointing along the span of the wing, the y-axis along the streamwise direction and the z-axis perpendicular up. Each structural node

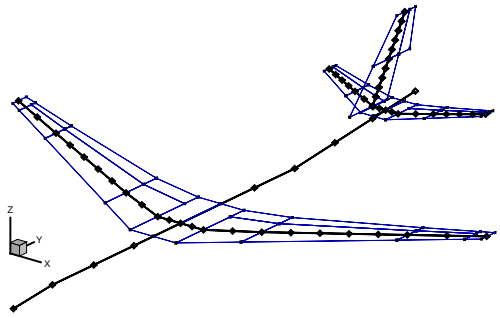

Figure 4.6: Finite element beam-stick model of FFAST aircraft

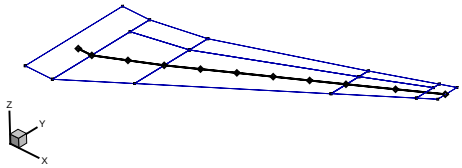

Figure 4.7: Finite element beam model of isolated FFAST wing

Table 4.1: FFAST Aircraft Structural Parameters

(Wing) Young's Modulus E in Nm^{-2}	1.8E+11
(Fuselage) Young's Modulus E in Nm^{-2}	1.5E+11
(Tail Plane) Young's Modulus E in Nm^{-2}	1.8E+11
Poisson's Ratio ν	0.3
Material Density ρ kgm^{-3}	2.0E+03

j in the nonlinear finite element beam model coincides with a 2D aerofoil section in the y-z plane. The remaining structural nodes along the fuselage and vertical tail plane are assumed to experience no aerodynamic loading. The aerodynamic forces acting on each aerofoil section are treated as follower forces that depend on the motion of the structural nodes.

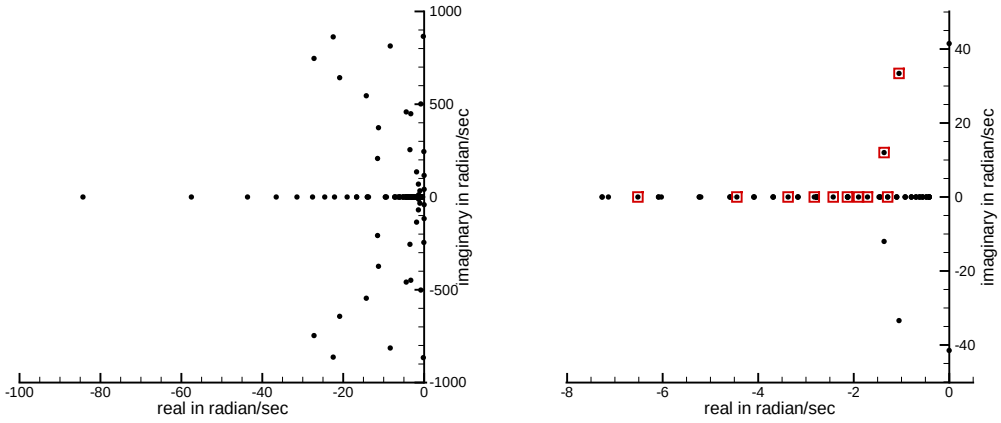

(a) Full view of eigenspectrum (b) Zoom-in at origin

Figure 4.8: Eigenvalue spectrum of FFAST wing

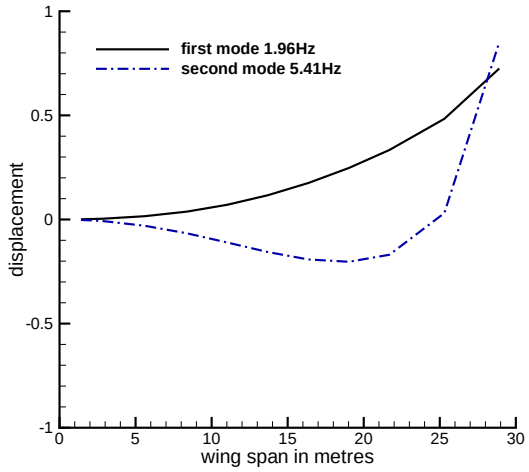

Figure 4.9: First two bending modes for the isolated wing

The structural models illustrated here include the FFAST aircraft and corresponding isolated wing. These are large structural models where each structural node corresponds to a two-dimensional aerofoil modelled by the linear aerodynamic strip theory. To form the reduced-order model for such a system, it is important to identify the eigenmode basis which capture the dominant physics of the system dynamics. The eigensolution of this type of aeroelastic system consists of a large number of purely real-valued eigenvalues arising from the aerodynamic and gust degrees-of-freedom, referred to as the fluid unknowns. There also exists complex-conjugate pairs of eigenvalues arising from the structural degrees-of-freedom referred to as the structural unknowns. This is can be recognised as a system extension to the sectional aerofoil test case as described in Section 3.2.1. Figure 4.8 illustrates the eigenspectrum.

To construct an accurate reduced-order model it is crucial to retain the first few lower-frequency, weakly-damped structural modes which are associated with dominant large amplitudes. These take the form of complex-conjugate pairs in the eigensolution. The number of modes depends on the type of structure. In the case of the isolated FFAST wing, the first two lower-frequency structural bending modes (Fig. 4.9) are found to be sufficient and any additional structural mode give negligible improvement to the reduced-order solution. In the case of the full FFAST aircraft, two additional structural modes associated with the fuselage are needed.

In addition, there exists a number of purely real-valued 'gust eigenmodes' which contributes to the accuracy of the structural response during the gust disturbance phase and should be included. These gust eigenmodes can always be determined analytically by the expression $\lambda = -\epsilon_3 U/b$, where U is the freestream velocity, b is the local semi-chord length corresponding to the aerofoil sections and $\epsilon_3 = 0.1393$ is the lower time constant used in the exponent in the approximation of the Küssner function [55]. This mode is demonstrated to be dominant in coupling the structural response to the gust input as discussed for the pitch-plunge aerofoil model in Chapter 3. The accuracy of the solution will improve with increasing number of gust modes starting with the one of the lowest value. This relates to the aerofoil section at the furthermost outboard position at the wing tip. The number of gust modes required to achieve a good prediction varies with the total number of aerodynamic strips of the model and it useful to choose a large number of gust modes. In practice it is conservative to calculate and include this lower-valued gust mode arising from more than half of all the wing nodes as this is still a minimal fraction of the total system size as will be illustrated in the results discussion hereafter (Section 4.2.4). For clarity, in Fig. 4.8 some of these important eigenmodes are highlighted in squares.

Similar to gust eigenmodes, there exist, corresponding to the time constants of the Wagner function, purely real-valued 'aerodynamic eigenmodes' which make up the dominant portion of all eigenvalues on the real axis. The inclusion of these modes were found to have minimal impact on the reduced-order solution for the gust response simulations examined.

The nonlinear reduced-order model is retained up to second order with respect to the system states. Furthermore, since the analytical expression for the system matrices are not possible, the matrix-free approach using finite differences is used.

The FFAST wing is simulated for gust response calculation with the aim to analyse the effect of geometric structural nonlinearity and the reduced-order model. The FFAST wing is placed in a freestream flow of 50 ms^{-1} at sea-level and subjected to discrete 1-cos gust disturbance acting in the vertical direction with intensity of 14% of the freestream speed. The amplitude of this gust intensity is chosen high to induce the nonlinear effects. A range of standard gust lengths are evaluated ranging from 9 m to 107 m. Figure 4.10 (a) shows the response histories of the wing tip to the range of

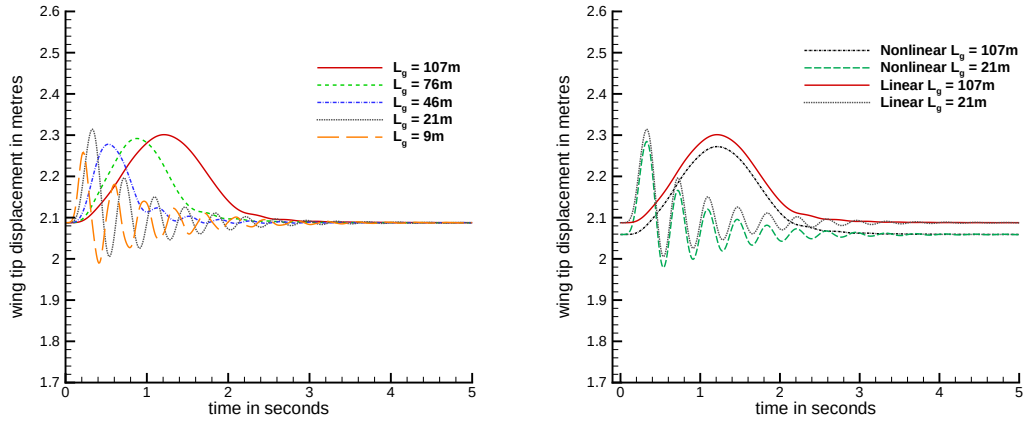

(a) Linear model (b) Linear compared with nonlinear model

Figure 4.10: Linear and nonlinear wing tip response to various gust lengths at 50 ms^{-1} freestream speed

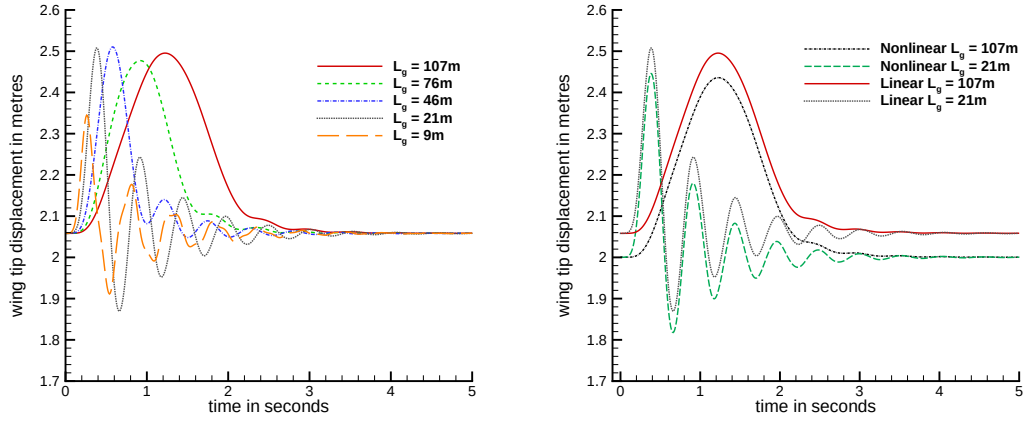

(a) Linear model (b) Linear compared with nonlinear model

Figure 4.11: Linear and nonlinear wing tip response at reduced stiffness to various gust lengths at 50 ms^{-1} freestream speed

gust lengths with the short length gusts producing highly oscillatory responses while the longer gusts give a smooth damped dynamic response. Since the largest amplitudes are found for gust lengths of 21 m and 107 m, these will be discussed in more detail below. Figure 4.10 (b) shows the geometrically nonlinear solution at these two specific gust lengths of 21 m and 107 m. The numerical approach here is to first perform a linearised and nonlinear static solution for the linear and nonlinear structural models, respectively. From this static solution, the linearised and nonlinear time-integration is performed based on the Newmark scheme previously discussed. In general, the geometrically nonlinear solution differs moderately from the linear solution and has overall

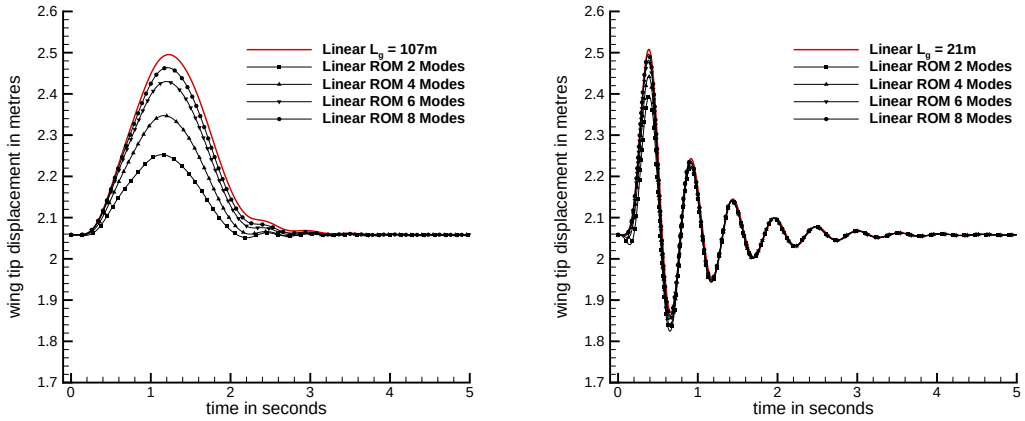

(a) Linear ROM $L_g = 107$ m (b) Linear ROM $L_g = 21$ m

Figure 4.12: FFAST wing linear reduced-order model at two distinct gust lengths

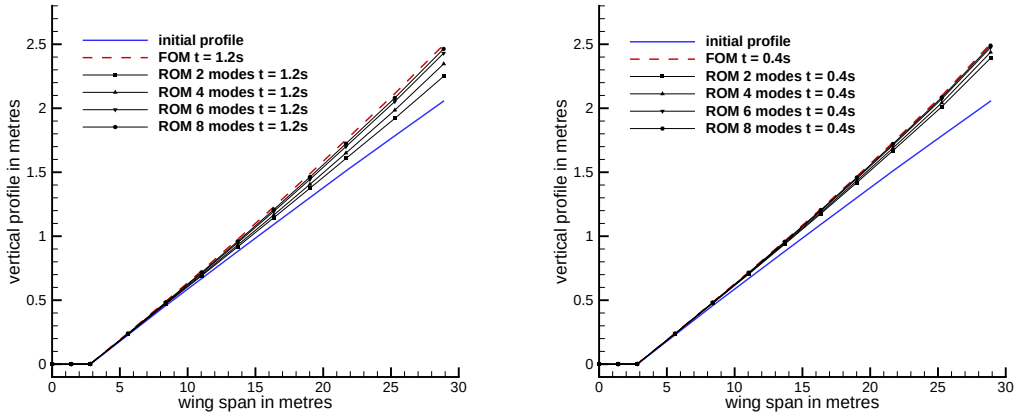

(a) Linear ROM $L_g = 107$ m (b) Linear ROM $L_g = 21$ m

Figure 4.13: Linear wing profile at maximum amplitude for two distinct gust lengths

reduced amplitudes in the peak dynamic response as well as the initial steady-state solution. However, the effect of the geometric nonlinearity is minimal, this is due to the high structural stiffness of the FFAST wing with $E = 1.8\text{E}+11$ Pa. For the purpose of emphasising the geometric nonlinear effects, all the subsequent results have a reduced material stiffness of $E = 9.0\text{E}+10$ Pa. From a civil aircraft design perspective, this is a significant reduction. Figure 4.11 shows equivalent results, compared with Fig. 4.10, at this reduced structural stiffness. Higher wing tip deflections are observed as expected for the softened wing. However, the differences between the nonlinear and linear response, in both the steady-state solution and the peak gust response, for the softened case is more pronounced.

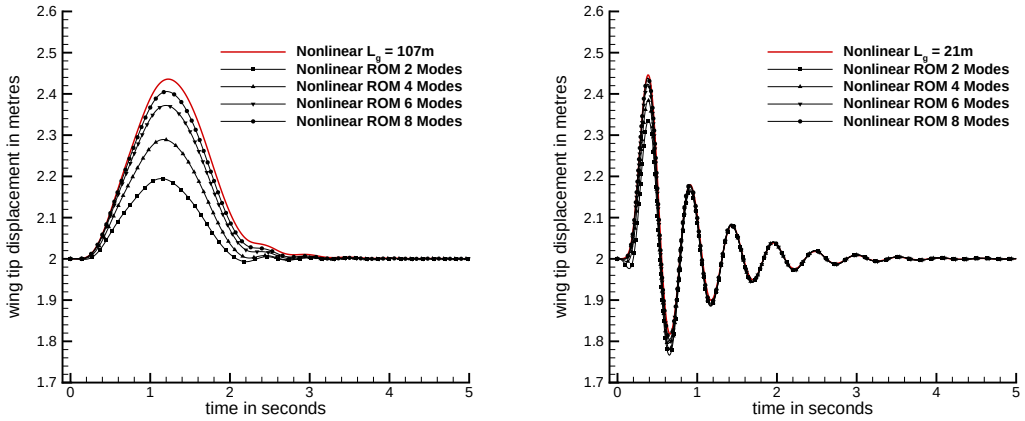

(a) Nonlinear ROM $L_g = 107$ m (b) Nonlinear ROM $L_g = 21$ m

Figure 4.14: FFAST wing nonlinear reduced-order model at two distinct gust lengths

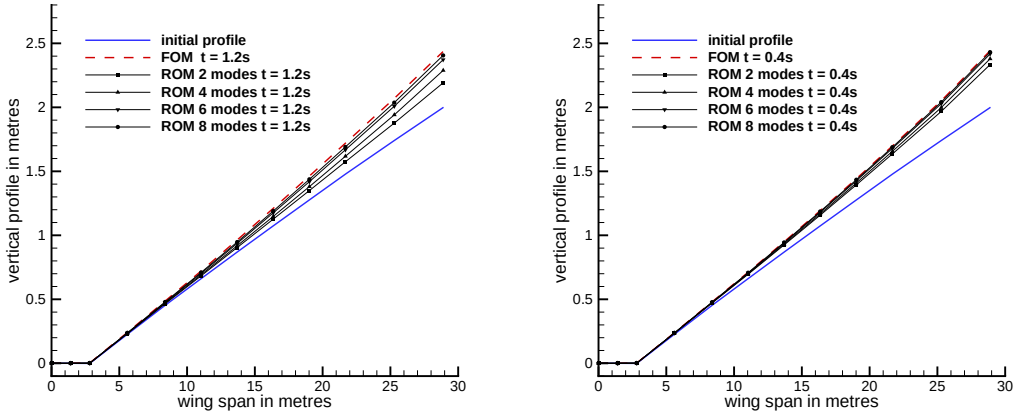

(a) Nonlinear ROM $L_g = 107$ m (b) Nonlinear ROM $L_g = 21$ m

Figure 4.15: Nonlinear wing profile at maximum amplitude for two distinct gust lengths

Next, the application of the linear reduced-order model is considered. It has been previously discussed that the structural model is large in size and fully nonlinear and it is important to establish an understanding of how model reduction can be applied to a large full scale industrial aircraft model. In this current approach the term $\boldsymbol{\mathcal{B}}$ is neglected in Eq. (2.12). Several reduced-order models are constructed based on various numbers of basis eigenmodes. The selection of such eigenmodes follows the method described previously this section. First, the two lowest-frequency structural modes are used. Then, additional gust modes are included in the reduced-order model basis. The system is simulated under the same two critical gust lengths as previously. Figure 4.12

shows the results produced by the linear reduced-order models for the wing tip motion history. It is clear that by including additional gust modes the reduced-order model produces incrementally better representations of the full-order solution. The spanwise displacement profile at the maximum amplitude point as produced by the full-order simulation as well as the reduced-order models is shown in Fig. 4.13. For the long length gust at $L_g = 107$ m this occurs at 1.2 s, and for the short length gust at 0.4 s. It can be observed that by including additional gust modes the solution is improved for all structural nodes. A satisfactory reduced-order model solution is obtained using eight modes reducing a full-order system of 220 degrees-of-freedom. In general, adding more gust modes improves overall approximation in the solution.

The application of the nonlinear reduced-order model includes the symmetric multilinear vector function of second-order derivatives, $\boldsymbol{\mathcal{B}}$, in Eq. (2.12). Figures 4.14 and 4.15 show the same set of results for those simulations. The results follow a similar trend compared with the linear case, with the additional feature that the nonlinear reduced-order model is able to capture the lower amplitude of the nonlinear response.

The same set of simulations are performed for the full scale FFAST aircraft with reduced stiffness for the wings ($E = 9.0\text{E} + 10$ Pa) and unaltered stiffness for the fuselage section ($E = 1.5 \times 10^{11}$ Pa). For the linear reduced-order model construction additional basis eigenmodes are required to achieve an accurate prediction of the full-order solution. Initially the first four structural eigenmodes are included. Additional gust modes are added to obtain improving representations of the full-order solution. A satisfactory result (a discrepancy of less than 1% in the peak response amplitude) is achieved with 16 basis eigenmodes in total. This is a reduction of a 1180 degrees-of-freedom system. Figure 4.16 shows the performance of the linear reduced-order model at the same two gust lengths: $L_g = 107$ m and $L_g = 21$ m. Similar results are obtained by the nonlinear reduced-order model presented in Fig. 4.17

4.2.5 Bending Moment Calculations

This section extends the investigations on the FFAST wing to the evaluation of bending moment for gust response. The modelling of geometric structural nonlinearity can provide better loads prediction than the corresponding linear model and lower bending moment loads are expected based on the reduced dynamic response amplitudes already demonstrated. The studies presented here are based on the model at two structural stiffness values; one at 100% of the Young's Modulus and one at 10%. As already mentioned, it is important to study the lower structural stiffness to highlight the geometrical nonlinear effect which becomes prominent with large structural deformations. The previous investigation dealt with the dynamic motion response of the FFAST wing where a reduction in the structural stiffness by a factor of 2 was introduced. Here, the stiffness reduction by the factor of 10 is aimed to further differentiate specifically the

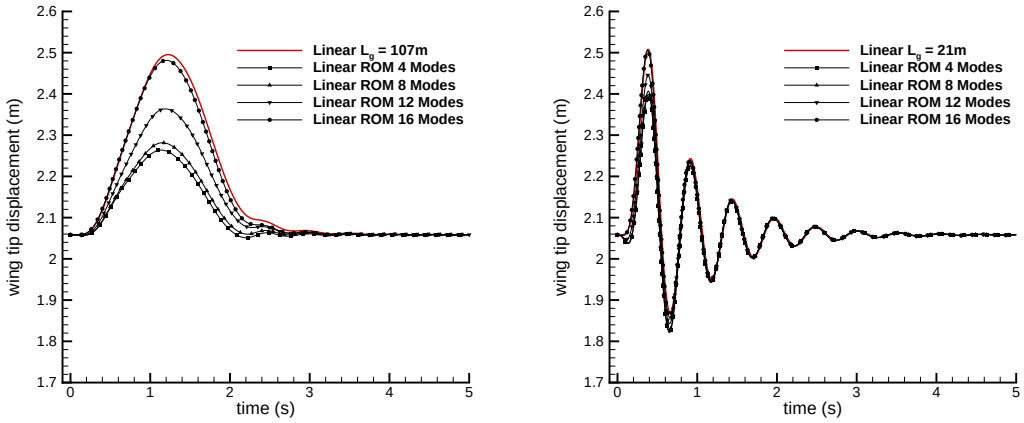

(a) Linear ROM $L_g = 107$ m (b) Linear ROM $L_g = 21$ m

Figure 4.16: FFAST aircraft linear reduced-order model at two distinct gust lengths

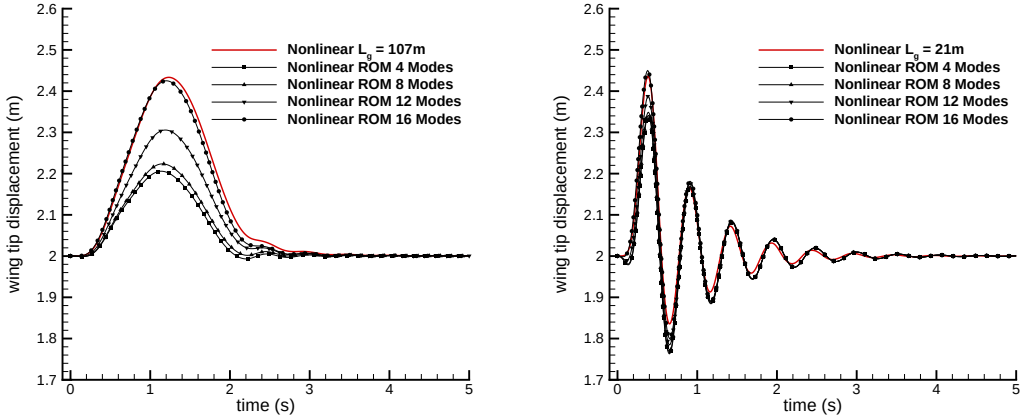

(a) Nonlinear ROM $L_g = 107$ m (b) Nonlinear ROM $L_g = 21$ m

Figure 4.17: FFAST aircraft nonlinear reduced-order model at two distinct gust lengths

response of the wing bending moments during gust disturbances. The interest here is the influence of the geometrical nonlinearity on the bending moment distribution in response to gust disturbances.

The test cases herein are based on a flow condition of 50 ms^{-1} at sea-level density. A range of standard gust lengths of the 1-cos profile are simulated. The gust intensity is set to 14% of the freestream velocity to induce large deformations and promote the nonlinear effect.

Figure 4.18 shows the dynamic response histories of the wing tip to the range of gust lengths. The corresponding peak bending moment distributions are shown which are evaluated at the maximum deflection point during each of the time history. It is

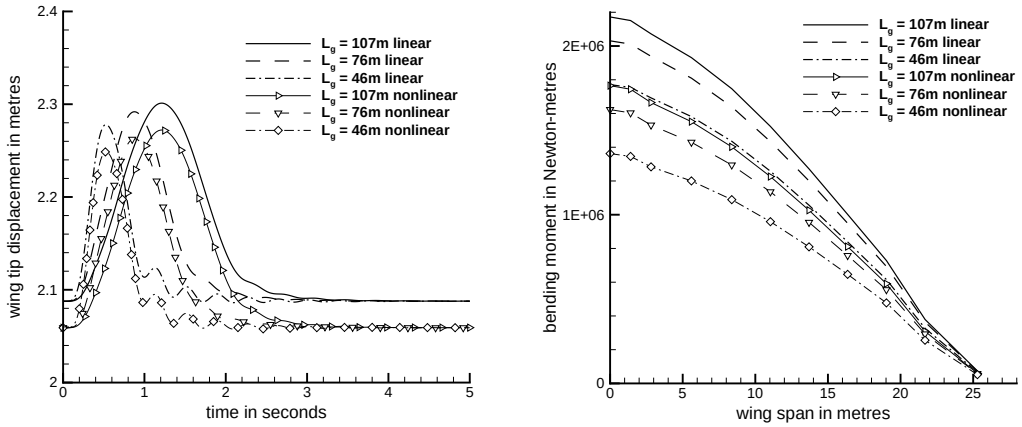

(a) dynamic response history (b) peak bending moment

Figure 4.18: Linear and nonlinear peak bending moment response at 100%E

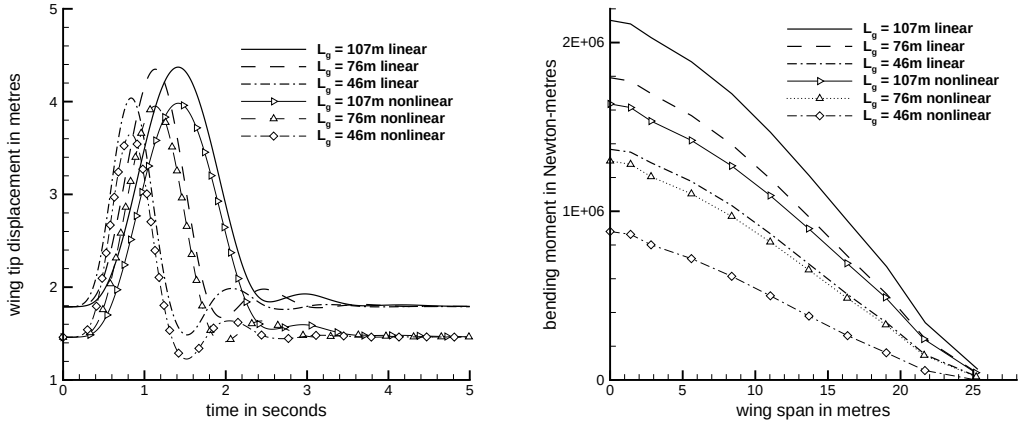

(a) dynamic response history (b) peak bending moment

Figure 4.19: Linear and nonlinear peak bending moment response at 10%E

important to note the comparison between the fully linear structural model and the geometrically nonlinear model. Similar to the previous sections the reduced peak amplitudes wing tip responses are observed in the nonlinear case. In addition, there are clear reductions in the bending moment distributions of the nonlinear case. Figure 4.19 shows the same set of results with the structural stiffness lessened to 10% its default value. An identical trend is observed, but most importantly, larger reductions in bending moment of the nonlinear case is shown arising from greater geometrical nonlinear effect.

Next, the application of the linear reduced-order model is considered. To calculate the bending moment from the reduced-order model, the full-order solution is reconstructed from the reduced space at every time step. It is important to point out here

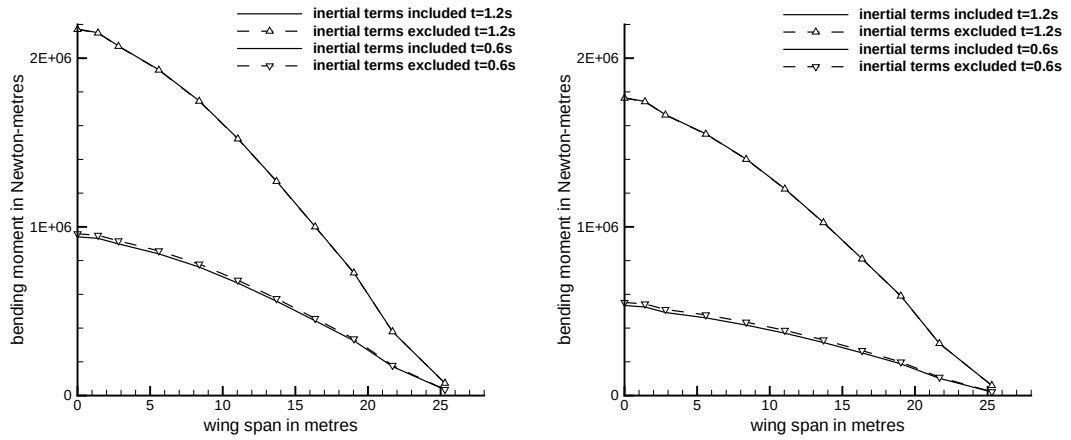

(a) linear, $L_g = 107$m

(b) nonlinear, $L_g = 107$m

Figure 4.20: Comparison of inertial contribution in the evaluation of peak bending moment distribution

that the bending moment arising from the inertial contributions are negligible; a direct comparison shown in Fig. 4.20 demonstrates this clearly. Here it is observed that the bending moment calculation, including and excluding inertial terms, for both the linear and nonlinear structural models show almost exact agreement indicating that the internal forces arise from structural deformations only. Conveniently for the reduced-order model only the global stiffness matrix $\tilde{K}$ and the physical space states are required to be reconstructed at every time step, while no inertial states are necessary. For the linear reduced-order model the same set of modes are used from Section 4.2.4. That is the first two lowest-frequency structural modes and six gust modes. The corresponding results are shown in Figs. 4.21 and 4.22. Good agreement is obtained throughout.

4.3 Summary of Nonlinear Beam Model Investigation

In this section large scale aeroelastic models are considered with the focus on geometric structural nonlinearity. The modelling framework is based on geometric exact description of large beam deformations and is used to model slender wing structures. This finite-element structural model is coupled with the linear aerodynamics model established in Chapter 3 by assuming each structural node along the wing corresponds to a typical sectional aerofoil. The novelty here is the representation of a typical civil aircraft using the geometrically nonlinear structural model.

Based on this general formulation a number of structural model test cases are constructed. The first model is a simple restrained flexible cantilever wing. The main focus of building this model is to establish the extended sectional aerofoil aerodynamic formulation to the three-dimensional wing. Simple linear static results comparison

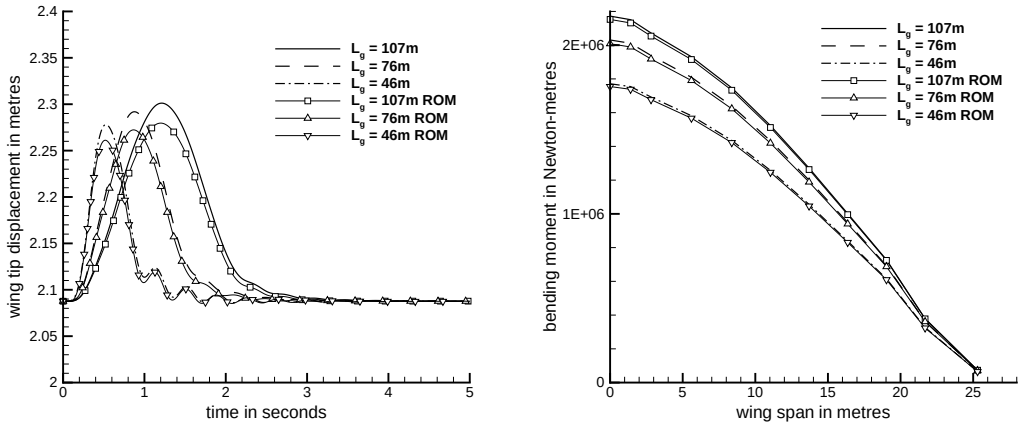

(a) dynamic response history (b) peak bending moment

Figure 4.21: Linear ROM peak bending moment response at 100%E

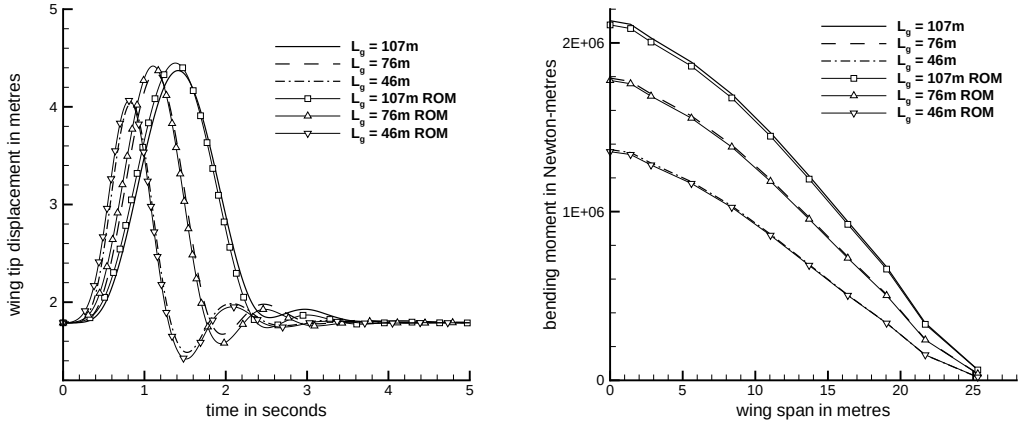

(a) dynamic response history (b) peak bending moment

Figure 4.22: Linear ROM peak bending moment response at 10%E

show excellent agreement with NASTRAN and nonlinear results highlights the beam shortening effect due to accounting for geometric nonlinearity. Lastly, a direct gust response analysis shows excellent agreement in the peak deformation compared with an equivalent NASTRAN model based on DLM aerodynamics.

The model is then modified to a rigid unrestrained free-flying beam. The aim is to investigate the rigid-body dynamics simulation. One key change here to the aerodynamic formulation is that the aerodynamic dependence on the structural flexible degrees-of-freedom are replaced with analogous rigid-body ones. Free response and gust response results are presented for this test case.

The next study extends the modelling approach to full scale nonlinear aircraft structures for gust response calculations and reduced-order modelling. The novel idea is

establishing an accurate reduced-order model for a fully geometrically nonlinear large scale civil aircraft. The test cases herein are based on the FFAST aircraft model and is constructed by hand. The nonlinear model reduction approach is based on the formulation established in Chapter 2. An approach to identify the important eigenmodes, used as basis in the model reduction, is discussed. Besides the lowest-frequency structural modes, also gust modes should be included if the initial transient response during the gust is to be accurately represented. These gust eigenmodes can always be identifed as their corresponding eigenvalues can be calculated by hand. In general, both the linear and nonlinear (up to second order) reduced models show accurate predictions with respect to their corresponding linear and geometrically nonlinear full-order solutions when simulating gust encounter at a range of gust lengths. It is important to note that the peak deflection for the structural response is accurately reproduced in the reduced models. For the largest test case, the full aircraft, a reduction in system size from 1180 to 16 is achieved. This reduction would be much more significant if nonlinear aerodynamics were included as well.

The last study investigates the effect of nonlinearity on the internal structural forces during gust encounters. For the full-order geometrically nonlinear model, this process involves reconstructing the global stiffness matrix $\tilde{K}$ at every time step and evaluating the instantaneous deformed configuration. For the linear reduced-order model reconstructing the full-order state in physical space at every time step is required. In general, modelling geometric nonlinearity reduces bending moment loads in dynamic gust calculations. However significant reduction in stiffness is required to lower the wing root bending moment. The linear reduced-order model shows accurate representation of the full-order solution in bending moment distributions.

Chapter 5

Conclusions and Outlook

The investigation of structural nonlinearity and its gust load alleviating effects have been the objective of this thesis. The specific task addressed here is first to introduce structural nonlinearity into the aeroelastic models and then to efficiently and rapidly predict the stability properties and dynamic response of the resulting nonlinear system. To target the task of efficiently simulating the dynamic response, the modelling of these structural nonlinearities are encapsulated within the central framework of nonlinear model order reduction by eigenmode decomposition. The approach here is to extract the dominant dynamics of an aeroelastic system to form a lower-dimensional model which is computationally cheaper to simulate while preserving accurate prediction of the full-order model.

Two distinct types of structural nonlinearity which are inherent in aeroelastic structures possible in the civil domain are studied over several numerical models. First, concentrated nonlinearities occur, for example, in aeroelastic systems in the forms of freeplay and cubic stiffness. The second type is known as distributed nonlinearity, specifically in this case, the geometrical nonlinearity associated with the exact modelling of large structural deformations. Such nonlinearity modelling assumptions are typically used to represent very flexible aircraft structures. Here it is introduced into large civil aircraft type models.

In Chapter 2 the derivation of the nonlinear model reduction framework based on eigenmode decomposition is presented. The model reduction is formulated with the novel extension to include up to fifth order derivatives in the Taylor expansion of the nonlinear full order residual function while previously only up to third order derivatives were considered. The underlying aim is such that higher order nonlinear behaviour of the full-order system can therefore be captured with the extended reduced model formulation.

In Chapter 3 the three degree-of-freedom aerofoil featuring concentrated discrete stiffness nonlinearity is investigated. The structural formulation takes into account the nonlinear spring stiffness in each structural degrees-of-freedom. The aerodynamics

model is linear and uses Wagner's function to represent the fluid forces arising from aerofoil motion and Küssner function to represent the loading arising from gust disturbances. The coupled model is recast into first-order semi-discrete form to allow for the application of nonlinear model order reduction as discussed in Chapter 2. First, linear stability analysis to determine the flutter point of the various aerofoil configurations is achieved by solving for the eigensolution of the system's Jacobian matrix directly. Then, the model is modified in the structural equations to include freeplay in the torsional degree-of-freedom to further verify the model. The time domain simulations are performed based on the structural baseline model reported in established literature and excellent agreement is found. Gust response characteristics are investigated for the linear system as well as the corresponding linear reduced-order model. The reduced-order model basis play an important role on the accuracy of the reduced-order model results. Structural eigenmodes alone are not sufficient if transient behaviour during a gust encounter is to be accurately simulated by the reduced-order model. A specific gust mode is required with the eigenvalue corresponding to the lower time constant of the exponent in the approximation to the Küssner function.

In the investigation of limit-cycle oscillation arising from structural nonlinearity, stiffness nonlinearity is introduced into the pitch degree-of-freedom in polynomial form up to fifth order such that the system exhibits the desired limit-cycle behaviour. Including multiple eigenmodes in the basis for the reduced-order model is unnecessary in the case of a supercritical limit-cycle oscillation if only the steady-state amplitude is required. Results using only the critical mode for model reduction are in excellent agreement with the full-order response. Multiple modes are necessary however, to capture the transient behaviour. For the case of subcritical limit-cycle behaviour, even if the interest is in the amplitude only, the critical mode alone is not sufficient. Multiple modes are mandatory to resolve the discrepancy between the reduced model prediction and the full-order solution. This is the first application, to the author's best knowledge, of a projection reduced order model based on eigenmodes, to subcritical limit-cycle oscillation.

In Chapter 4 large scale civil aeroelastic models are considered with the focus on geometric structural nonlinearity. The modelling approach is based on geometric exact description of large beam deformations. This finite-element structural model is coupled with the linear strip aerodynamics model by assuming each structural node along the wing coincides to a sectional aerofoil. The interest here is the modelling of a typical civil aircraft in a geometrically nonlinear structural framework. The first model is a simple restrained flexible cantilever wing to extend sectional aerofoil aerodynamic formulation to the three-dimensional wing. A direct gust response analysis shows excellent agreement in the peak deformation with an equivalent NASTRAN model. Next, a rigid unrestrained free-flying beam is considered to investigate the rigid-body dynamics simulation. The key change here to the aerodynamic formulation is that the aerodynamic

dependence on the structural flexible degrees-of-freedom are replaced with analogous rigid-body ones.

The modelling approach is then extended to full scale nonlinear aircraft structures for gust response calculations and reduced-order modelling. The novelty is constructing a reliable reduced-order model for a fully geometrically nonlinear large scale civil aircraft. The structural model here is based on the FFAST aircraft. An approach to identify the important eigenmodes, used as basis in the model reduction, is discussed. First, the lowest-frequency structural modes are necessary. Second, gust modes should be included to accurately reproduce the initial transient response during a gust disturbance. These key gust eigenmodes can always be found as their corresponding eigenvalues can be calculated directly. Both the linear and nonlinear reduced models show accurate prediction with respect to their corresponding linear and nonlinear full-order solutions over a range of standard gust lengths encountered in the civil domain. Most importantly, the peak deflection for the structural response is accurately captured by the reduced models. For the largest structural model of the full aircraft, a reduction in system size from 1180 to 16 is achieved.

In summary, two types of structural nonlinear behaviour have been investigated in this work within an extended nonlinear model reduction framework. Regarding the discrete nonlinearity modelled in the three degree-of-freedom aerofoil, the extension of nonlinear model reduction to quintic order is able to accurately predict the resulting limit-cycle behaviour of the full-order system. Extension of this formulation to a full-scale geometrically nonlinear FFAST civil aircraft model demonstrated a reliable model reduction approach of the aeroelastic system for gust response simulations. Furthermore, reductions in the wing root bending moment, a key structural design criteria, is achieved with the nonlinear structural model.

5.1 Future Work

There are a number important directions which can be taken in future studies. With respect to the current formulation, the model reduction applied to the full scale nonlinear FFAST model can be extended beyond the second order derivative in the Taylor series expansion of the nonlinear residual function. The purpose of this development is to investigate the reduced order modelling capability when dealing with higher-order structural nonlinearity as was achieved for the simple aerofoil model in Chapter 3. This will in particular allow for combined structural nonlinearities such that both discrete polynomial and distributed geometrically exact form is representable in the reduced order model. The importance here is being able to investigate more structurally nonlinear configurations with respect to the gust load alleviating capability.

As is noted in Chapter 4, previous work in model reduction has been applied to aerodynamics modelled using computational fluid dynamics while the structural model

was considered linear. The work here has focused on structural nonlinearity while keeping the aerodynamics simple. A desired goal is to combine both nonlinear structural modelling with computational fluid dynamics within the reduced order modelling framework. This aims to achieve rapid solutions to fully coupled nonlinear aeroelastic models which will be of particular interest in the civil domain and enabling rapid investigations close to real time in future digital aircraft design in a multidisciplinary context.

Bibliography

[1] Hoblit, F. M., *Gust Load on Aircraft: Concept and Applications*, American Institute of Aeronautics and Astronautics Educations Series, 1988.

[2] Sousa, V. C., Anicézio1, M., De Marqui Jr., C., and Erturk, A., "Enhanced Aeroelastic Energy Harvesting by Exploiting Combined Nonlinearities: Theory and Experiment," *Smart Materials and Structures*, Vol. 20, No. 9, 2011.

[3] Kota, S., "Design of a Variable Stiffness Spar," Tech. Rep. TR–97–01, Aerospace Structures Information and Analysis Center, Palo Alto, CA, 1997.

[4] Chen, P., Sarhaddi, D., Jha, R., Liu, D., Griffin, K., and Yurkovich, R., "Variable Stiffness Spar Approach for Aircraft Maneuver Enhancement Using ASTROS," *Journal of Aircraft*, Vol. 37, No. 5, 2000, pp. 865–871.

[5] Cooper, J. E., "Adaptive Stiffness Structures for Air Vehicle Drag Reduction," Tech. Rep. RTO-MP-AVT-141 Paper 15, 2006.

[6] Livne, E. and Weisshaar, T. A., "Aeroelasticity of Nonconventional Airplane ConfigurationsPast and Future," *Journal of Aircraft*, Vol. 40, No. 6, 2003, pp. 1047–1065.

[7] Dowell, E. H. and Tang, D., "Nonlinear Aeroelasticity and Unsteady Aerodynamics," *AIAA Journal*, Vol. 40, No. 9, 2002, pp. 1697–1707.

[8] Lee, B. H. K., Price, S. J., and Wong, Y. S., "Nonlinear aeroelastic analysis of airfoils: bifurcation and chaos," *Progress in Aerospace Sciences*, Vol. 35, No. 3, 1999, pp. 205–334.

[9] van Schoor, M. C. and von Flotow, A. H., "Aeroelastic Characteristics of a Highly Flexible Aircraft," *Journal of Aircraft*, Vol. 27, No. 10, 1990, pp. 901–908.

[10] Patil, M. J., Hodges, D. H., and Cesnik, C. E. S., "Nonlinear Aeroelastic Analysis of Complete Aircraft in Subsonic Flow," *Journal of Aircraft*, Vol. 37, No. 5, 2000, pp. 753–760.

[11] Hodges, D. H., "A Mixed Variational Formulation Based on Exact Intrinsic Equations for Dynamics of Moving Beams," *International Journal of Solids and Structures*, Vol. 26, No. 11, 1990, pp. 1253–1273.

[12] Goland, M., "The Flutter of a Uniform Cantilever Wing," *Journal of Applied Mechanics*, Vol. 12, No. 4, 1945, pp. A197–A208.

[13] Drela, M., "Integrated Simulation Model for Preliminary Aerodynamic, Structural, and Control-Law Design of Aircraft," *AIAA Paper 1999-1394*, 1999, pp. 1644–1656.

[14] Cesnik, C. E. S. and Brown, E. L., "Modeling of High Aspect Ratio Active Flexible Wings for Roll Control," *AIAA Paper 2002-1719*, 2002.

[15] Peters, D. A. and Cao, W., "Finite State Induced Flow Models Part I: Two-Dimensional Thin Airfoil," *Journal of Aircraft*, Vol. 32, No. 2, 1995, pp. 313–322.

[16] Cesnik, C. E. S. and Su, W., "Nonlinear Aeroelastic Modeling and Analysis of Fully Flexible Aircraft," *AIAA Paper 2005-2169*, 2005.

[17] Su, W. and Cesnik, C. E. S., "Dynamic Response of Highly Flexible Flying Wing," *AIAA Paper 2006-1636*, 2006.

[18] Patil, M. J. and Hodges, D. H., "Flight Dynamics of Highly Flexible Flying Wings," *Journal of Aircraft*, Vol. 43, No. 6, 2006, pp. 1790–1799.

[19] Patil, M. J. and Taylor, D. J., "Gust Response of Highly Flexible Aircraft," *AIAA Paper 2006-1638*, 2006.

[20] Palacios, R. and Cesnik, C. E. S., "Static Nonlinear Aeroelasticity of Flexible Slender Wings in Compressible Flow," *AIAA Paper 2005-1945*, 2005.

[21] Garcia, J. A., "Numerical Investigation of Nonlinear Aeroelastic Effects on Flexible High-Aspect-Ratio Wings," *Journal of Aircraft*, Vol. 42, No. 4, 2005, pp. 1025–1036.

[22] Shearer, C. M. and Cesnik, C. E. S., "Nonlinear Flight Dynamics of Very Flexible Aircraft," *Journal of Aircraft*, Vol. 44, No. 5, 2007, pp. 1528–1545.

[23] Shearer, C. M. and Cesnik, C. E. S., "Modified Generalised-Alpha Method for Integrating Governing Equations of Very Flexible Aircraft," *AIAA Paper 2006-1747*, 2006.

[24] Murua, J., Hesse, H., Palacios, R., and Graham, J. M. R., "Stability and Open-Loop Dynamics of Very Flexible Aircraft Including Free-Wake Effects," *AIAA Paper 2011-1915*, Vol. 52, 2011.

[25] Cook, R. G., Palacios, R., and Goulart, P., "Robust Gust Alleviation and Stabilization of Very Flexible Aircraft," *AIAA Journal*, Vol. 51, No. 2, 2013, pp. 330–340.

[26] Leishman, J. G., "Unsteady Lift of a Flapped Airfoil by Indicial Concepts," *Journal of Aircraft*, Vol. 31, No. 2, 1994, pp. 288–297.

[27] Rodden, W. P. and Johnson, E. H., *MSC.Nastran aeroelastic analysis user's guide*, MSC.Software Corporation, Santa Ana, CA, 2004.

[28] Morton, S. A. and Beran, P. S., "Hopf-Bifurcation Analysis of Airfoil Flutter at Transonic Speeds," *Journal of Aircraft*, Vol. 36, No. 2, 1999, pp. 421–429.

[29] Badcock, K. J., Woodgate, M. A., and Richards, B. E., "Hopf Bifurcation Calculations for a Symmetric Airfoil in Transonic Flow," *AIAA Journal*, Vol. 42, No. 5, 2004, pp. 883–892.

[30] Badcock, K. J., Woodgate, M. A., and Richards, B. E., "Direct Aeroelastic Bifurcation Analysis of a Symmetric Wing Based on Euler Equations," *AIAA Journal*, Vol. 42, No. 3, 2005, pp. 731–737.

[31] Badcock, K. J., Allan, M. R., and Beran, P. S., "Fast Prediction of Wing Rock Onset Based on Computational Fluid Dynamics," *International Forum for Aeroelasticity and Structural Dynamics*, 2005.

[32] Badcock, K. J. and Woodgate, M. A., "Bifurcation Prediction of Large-Order Aeroelastic Models," *AIAA Journal*, Vol. 48, No. 6, 2010, pp. 1037–1046.

[33] Timme, S., Badcock, K. J., Wu, M., and Spence, A., "Lyapunov Inverse Iteration for Stability Analysis using Computational Fluid Dynamics," *AIAA Paper 2012-1563*, 2012.

[34] Silva, W., "Identification of Nonlinear Aeroelastic Systems Based on the Volterra Theory: Progress and Opportunities," *Nonlinear Dynamics*, Vol. 39, No. 1–2, 2005, pp. 25–62.

[35] Lucia, D. J., Beran, P. S., and Silva, W. A., "Reduced-order modeling: new approaches for computational physics," *Progress in Aerospace Sciences*, Vol. 40, No. 1–2, 2004, pp. 51–117.

[36] Hall, K. C., Thomas, J. P., and Dowell, E. H., "Proper orthogonal Decomposition Technique for Transonic Unsteady Aerodynamic Flows," *AIAA Journal*, Vol. 38, No. 10, 2000, pp. 1853–1862.

[37] Woodgate, M. A. and Badcock, K. J., "Fast Prediction of Transonic Aeroelastic Stability and Limit Cycles," *AIAA Journal*, Vol. 45, No. 6, 2007, pp. 1370–1381.

[38] Badcock, K. J., Khodaparast, H. H., Timme, S., and Mottershead, J. E., "Calculating the Influence of Structural Uncertainty on Aeroelastic Limit Cycle Response," *AIAA Paper 2011-1741*, 2011.

[39] Da Ronch, A., Tantaroudas, N. D., and Badcock, K. J., "Reduction of Nonlinear Models for Control Applications," *AIAA Paper 2013-1491*, 2013.

[40] Da Ronch, A., Tantaroudas, N. D., Timme, S., and Badcock, K. J., "Model Reduction for Linear and Nonlinear Gust Loads Analysis," *AIAA Paper 2013-1492*, 2013.

[41] Timme, S., Badcock, K. J., and Da Ronch, A., "Linear Reduced Order Modelling for Gust Response Analysis using the DLR-TAU Code," *International Forum for Aeroelasticity and Structural Dynamics*, 2013.

[42] Palacios, R., Murua, J., and Cook, R., "Structural and Aerodynamic Models in Nonlinear Flight Dynamics of Very Flexible Aircraft," *AIAA Journal*, Vol. 48, No. 0, 2010, pp. 2648–2659.

[43] Hesse, H. and Palacios, R., "Consistent Structural Linearisation in Flexible-Body Dynamics with Large Rigid-Body Motion," *Computers & Structures*, Vol. 110–111, No. 11, 2012, pp. 1–14.

[44] Kuznetsov, Y. A., *Elements of Applied Bifurcation Theory*, Springer-Verlag New York, 2nd ed., 1998.

[45] Carr, J., *Applications of Centre Manifold Theory*, Springer-Verlag New York, 1982.

[46] Lee, B. H. K., Gong, L., and Wong, Y. S., "Analysis and Computation of Nonlinear Dynamic Response of a Two-Degree-of-Freedom System and Its Applications in Aeroelasticity," *Journal of Fluids and Structures*, Vol. 11, No. 3, 1997, pp. 225–246.

[47] Lee, B. H. K., Jiang, L. Y., and Wong, Y. S., "Flutter of an Airfoil with a Cubic Restoring Force," *Journal of Fluids and Structures*, Vol. 13, No. 1, 1999, pp. 75–101.

[48] Da Ronch, A., Badcock, K. J., Wang, Y., Wynn, A., and Palacios, R., "Nonlinear Model Reduction for Flexible Aircraft Control Design," *AIAA Paper 2012-4044*, 2012.

[49] Kanda, A. and Dowell, E. H., "Worst-Case Gust-Response Analysis for typical Airfoil Section with Control Surface," *Journal of Aircraft*, Vol. 42, No. 4, 2005, pp. 956–962.

[50] Conner, M. D., Tang, D. M., Dowell, E. H., and Virgin, L. N., "Nonlinear Behaviour of a Typical Airfoil Section with Control Surface Freeplay: A Numerical and Experimental Study," *Journal of Fluids and Structures*, Vol. 11, No. 1, 1997, pp. 89–109.

[51] Trickey, S. T., Virgin, L. N., and Dowell, E. H., "The Stability of Limit-Cycle Oscillations in a Nonlinear Aeroelastic System," *Mathematical, Physical and Engineering Sciences*, Vol. 458, No. 2025, 2002, pp. 2203–2226.

[52] L.Liu, Wong, Y. S., and Lee, B. H. K., "Non-Linear Aeroelastic Analysis Using The Point Transformation Method Part 1 Freeplay Model," *Journal of Sound and Vibrations*, Vol. 253, No. 2, 2002, pp. 447–469.

[53] Conner, M. D., Virgin, L. N., and Dowell, E. H., "Accurate numerical integration of state-space models for aeroelastic systems with freeplay," *AIAA Journal*, Vol. 34, No. 10, 1996, pp. 2202–2205.

[54] Tang, D. and Dowell, E. H., "Aeroelastic Airfoil with Free Play at Angle of Attack with Gust Excitation," *AIAA Journal*, Vol. 48, No. 2, 2010, pp. 427–442.

[55] Fung, Y. C., *An Introduction to the Theory of Aeroelasticity*, Dover Publications, 1952.

[56] Theodorsen, T., "General Theory of Aerodynamic Instability and the Mechanism of Flutter," *NACA Report Nr. 496*, 1935.

[57] Jones, W. P., "Aerodynamic Forces on Wings in Non-uniform Motion," *Aeronaut. Research Council R.&M.*, 1945.

[58] Dessi, D. and Mastroddi, F., "A Nonlinear Analysis of Stability and Gust Response of Aeroelastic Systems," *Journal of Fluids and Structures*, Vol. 24, No. 3, 2008, pp. 436–445.

[59] Saad, Y., *Iterative Methods for Sparse Linear Systems*, 2nd ed., 2003.

[60] Alighanbari, H. and Price, S. J., "The Post-Hopf-Bifurcation Response of an Airfoil in Incompressible Two-Dimensional Flow," *Nonlinear Dynamics*, Vol. 10, No. 4, 1996, pp. 381–400.

[61] Irani, S., Sarrafzadeh, H., and Amoozgar, M. R., "Bifurcation of a 3-DOF Airfoil with Cubic Structural Nonlinearity," *Chinese Journal of Aeronautics*, Vol. 24, No. 3, 2011, pp. 265–278.

[62] Price, S. J., Alighanbari, H., and Lee, B. H. K., "The aeroelastic response of a two-dimensional airfoil with bilinear and cubic structural nonlinearities," *Journal of Fluids and Structures*, Vol. 9, No. 2, 1995, pp. 175–193.

[63] Liu, L., Wong, Y. S., and Lee, B. H. K., "Application of the Centre Manifold Theory in Non-linear Aeroelasiticity," *Journal of Sound and Vibration*, Vol. 234, No. 4, 2000, pp. 641–659.

[64] Pettit, C. L. and Beran, P. S., "Effect of Parametric Uncertainity on Airfoil Limit Cycle Oscillation," *Journal of Aircraft*, Vol. 40, No. 5, 2003, pp. 1004–1006.

[65] Newmark, N. M., "A Method of Computation for Structural Dynamics," *Journal of the Engineering Mechanics Division*, Vol. 85, No. 3, 1959, pp. 67–94.

[66] Géradin, M. and Rixen., D., *Mechanical Vibrations: Theory and Applications to Structural Dynamics*, Wiley, Chichester, England, 2nd ed., 1997.

Appendix A

Multilinear Vector Functions of Higher Order Derivatives

Following the transformation of variables, functions of the second to fifth order derivatives of the nonlinear full order residual vector consist of $(2m)^K$ individual terms when computed directly where superscript K denotes the order of the derivative (see Table A.1). However, symmetries exist in these functions with respect to their arguments, such as $\boldsymbol{\mathcal{B}}(\boldsymbol{x},\boldsymbol{y}) = \boldsymbol{\mathcal{B}}(\boldsymbol{y},\boldsymbol{x})$ and $\boldsymbol{\mathcal{C}}(\boldsymbol{x},\boldsymbol{y},\boldsymbol{y}) = \boldsymbol{\mathcal{C}}(\boldsymbol{y},\boldsymbol{x},\boldsymbol{y}) = \boldsymbol{\mathcal{C}}(\boldsymbol{y},\boldsymbol{y},\boldsymbol{x})$ and so on. These symmetry properties can be exploited to reduce the total number of individual terms required.

For convenience, define the following auxiliary terms for the second and third order functions

$$
\begin{aligned}
b_{rr} &= \boldsymbol{\mathcal{B}}\big(\boldsymbol{\phi}_r,\boldsymbol{\phi}_r\big)z_r z_r + 2\boldsymbol{\mathcal{B}}\big(\boldsymbol{\phi}_r,\bar{\boldsymbol{\phi}}_r\big)z_r\bar{z}_r + \boldsymbol{\mathcal{B}}\big(\bar{\boldsymbol{\phi}}_r,\bar{\boldsymbol{\phi}}_r\big)\bar{z}_r\bar{z}_r \\
b_{rs} &= \boldsymbol{\mathcal{B}}\big(\boldsymbol{\phi}_r,\boldsymbol{\phi}_s\big)z_r z_s + \boldsymbol{\mathcal{B}}\big(\boldsymbol{\phi}_r,\bar{\boldsymbol{\phi}}_s\big)z_r\bar{z}_s + \boldsymbol{\mathcal{B}}\big(\bar{\boldsymbol{\phi}}_r,\boldsymbol{\phi}_s\big)\bar{z}_r z_s + \boldsymbol{\mathcal{B}}\big(\bar{\boldsymbol{\phi}}_r,\bar{\boldsymbol{\phi}}_s\big)\bar{z}_r\bar{z}_s
\end{aligned}
\tag{A.1}
$$

$$
\begin{aligned}
c_{rrr} &= \boldsymbol{\mathcal{C}}\big(\boldsymbol{\phi}_r,\boldsymbol{\phi}_r,\boldsymbol{\phi}_r\big)z_r z_r z_r + 3\boldsymbol{\mathcal{C}}\big(\boldsymbol{\phi}_r,\boldsymbol{\phi}_r,\bar{\boldsymbol{\phi}}_r\big)z_r z_r\bar{z}_r + 3\boldsymbol{\mathcal{C}}\big(\boldsymbol{\phi}_r,\bar{\boldsymbol{\phi}}_r,\bar{\boldsymbol{\phi}}_r\big)z_r\bar{z}_r\bar{z}_r \\
&\quad + \boldsymbol{\mathcal{C}}\big(\bar{\boldsymbol{\phi}}_r,\bar{\boldsymbol{\phi}}_r,\bar{\boldsymbol{\phi}}_r\big)\bar{z}_r\bar{z}_r\bar{z}_r \\
c_{rrs} &= \boldsymbol{\mathcal{C}}\big(\boldsymbol{\phi}_r,\boldsymbol{\phi}_r,\boldsymbol{\phi}_s\big)z_r z_r z_s + \boldsymbol{\mathcal{C}}\big(\boldsymbol{\phi}_r,\boldsymbol{\phi}_r,\bar{\boldsymbol{\phi}}_s\big)z_r z_r\bar{z}_s + 2\boldsymbol{\mathcal{C}}\big(\boldsymbol{\phi}_r,\bar{\boldsymbol{\phi}}_r,\boldsymbol{\phi}_s\big)z_r\bar{z}_r z_s \\
&\quad + 2\boldsymbol{\mathcal{C}}\big(\boldsymbol{\phi}_r,\bar{\boldsymbol{\phi}}_r,\bar{\boldsymbol{\phi}}_s\big)z_r\bar{z}_r\bar{z}_s + \boldsymbol{\mathcal{C}}\big(\bar{\boldsymbol{\phi}}_r,\bar{\boldsymbol{\phi}}_r,\boldsymbol{\phi}_s\big)\bar{z}_r\bar{z}_r z_s + \boldsymbol{\mathcal{C}}\big(\bar{\boldsymbol{\phi}}_r,\bar{\boldsymbol{\phi}}_r,\bar{\boldsymbol{\phi}}_s\big)\bar{z}_r\bar{z}_r\bar{z}_s \\
c_{rss} &= \boldsymbol{\mathcal{C}}\big(\boldsymbol{\phi}_r,\boldsymbol{\phi}_s,\boldsymbol{\phi}_s\big)z_r z_s z_s + \boldsymbol{\mathcal{C}}\big(\bar{\boldsymbol{\phi}}_r,\boldsymbol{\phi}_s,\boldsymbol{\phi}_s\big)\bar{z}_r z_s z_s + 2\boldsymbol{\mathcal{C}}\big(\boldsymbol{\phi}_r,\boldsymbol{\phi}_s,\bar{\boldsymbol{\phi}}_s\big)z_r z_s\bar{z}_s \\
&\quad + 2\boldsymbol{\mathcal{C}}\big(\bar{\boldsymbol{\phi}}_r,\boldsymbol{\phi}_s,\bar{\boldsymbol{\phi}}_s\big)\bar{z}_r z_s\bar{z}_s + \boldsymbol{\mathcal{C}}\big(\boldsymbol{\phi}_r,\bar{\boldsymbol{\phi}}_s,\bar{\boldsymbol{\phi}}_s\big)z_r\bar{z}_s\bar{z}_s + \boldsymbol{\mathcal{C}}\big(\bar{\boldsymbol{\phi}}_r,\bar{\boldsymbol{\phi}}_s,\bar{\boldsymbol{\phi}}_s\big)\bar{z}_r\bar{z}_s\bar{z}_s \\
c_{rst} &= \boldsymbol{\mathcal{C}}\big(\boldsymbol{\phi}_r,\boldsymbol{\phi}_s,\boldsymbol{\phi}_t\big)z_r z_s z_t + \boldsymbol{\mathcal{C}}\big(\boldsymbol{\phi}_r,\boldsymbol{\phi}_s,\bar{\boldsymbol{\phi}}_t\big)z_r z_s\bar{z}_t + \boldsymbol{\mathcal{C}}\big(\boldsymbol{\phi}_r,\bar{\boldsymbol{\phi}}_s,\boldsymbol{\phi}_t\big)z_r\bar{z}_s z_t \\
&\quad + \boldsymbol{\mathcal{C}}\big(\boldsymbol{\phi}_r,\bar{\boldsymbol{\phi}}_s,\bar{\boldsymbol{\phi}}_t\big)z_r\bar{z}_s\bar{z}_t + \boldsymbol{\mathcal{C}}\big(\bar{\boldsymbol{\phi}}_r,\boldsymbol{\phi}_s,\boldsymbol{\phi}_t\big)\bar{z}_r z_s z_t + \boldsymbol{\mathcal{C}}\big(\bar{\boldsymbol{\phi}}_r,\boldsymbol{\phi}_s,\bar{\boldsymbol{\phi}}_t\big)\bar{z}_r z_s\bar{z}_t \\
&\quad + \boldsymbol{\mathcal{C}}\big(\bar{\boldsymbol{\phi}}_r,\bar{\boldsymbol{\phi}}_s,\boldsymbol{\phi}_t\big)\bar{z}_r\bar{z}_s z_t + \boldsymbol{\mathcal{C}}\big(\bar{\boldsymbol{\phi}}_r,\bar{\boldsymbol{\phi}}_s,\bar{\boldsymbol{\phi}}_t\big)\bar{z}_r\bar{z}_s\bar{z}_t
\end{aligned}
\tag{A.2}
$$

Function	Direct	Exploiting Symmetry
$\boldsymbol{\mathcal{B}}$	$4m^2$	$2m^2+m$
$\boldsymbol{\mathcal{C}}$	$8m^3$	$\frac{2}{3}\left(2m^3+3m^2+m\right)$
$\boldsymbol{\mathcal{D}}$	$16m^4$	$\frac{1}{6}\left(4m^4+12m^3+11m^2+3m\right)$
$\boldsymbol{\mathcal{E}}$	$32m^5$	$\frac{1}{15}\left(4m^5+20m^4+35m^3+25m^2+6m\right)$

Table A.1: Number of terms required per function

$$
\begin{aligned}
d_{rrrr} &= \boldsymbol{\mathcal{D}}\left(\phi_r,\phi_r,\phi_r,\phi_r\right)z_r z_r z_r z_r + 4\boldsymbol{\mathcal{D}}\left(\phi_r,\phi_r,\phi_r,\bar{\phi}_r\right)z_r z_r z_r \bar{z}_r + 6\boldsymbol{\mathcal{D}}\left(\phi_r,\phi_r,\bar{\phi}_r,\bar{\phi}_r\right)z_r z_r \bar{z}_r \bar{z}_r \\
&\quad + 4\boldsymbol{\mathcal{D}}\left(\phi_r,\bar{\phi}_r,\bar{\phi}_r,\bar{\phi}_r\right)z_r \bar{z}_r \bar{z}_r \bar{z}_r + \boldsymbol{\mathcal{D}}\left(\bar{\phi}_r,\bar{\phi}_r,\bar{\phi}_r,\bar{\phi}_r\right)\bar{z}_r \bar{z}_r \bar{z}_r \bar{z}_r \\
d_{rrrs} &= \boldsymbol{\mathcal{D}}\left(\phi_r,\phi_r,\phi_r,\phi_s\right)z_r z_r z_r z_s + \boldsymbol{\mathcal{D}}\left(\phi_r,\phi_r,\phi_r,\bar{\phi}_s\right)z_r z_r z_r \bar{z}_s + 3\boldsymbol{\mathcal{D}}\left(\bar{\phi}_r,\phi_r,\phi_r,\phi_s\right)\bar{z}_r z_r z_r z_s \\
&\quad + 2\boldsymbol{\mathcal{D}}\left(\bar{\phi}_r,\bar{\phi}_r,\phi_r,\phi_s\right)\bar{z}_r \bar{z}_r z_r z_s + 2\boldsymbol{\mathcal{D}}\left(\phi_r,\phi_r,\bar{\phi}_r,\bar{\phi}_s\right)z_r z_r \bar{z}_r \bar{z}_s + 3\boldsymbol{\mathcal{D}}\left(\phi_r,\bar{\phi}_r,\bar{\phi}_r,\bar{\phi}_s\right)z_r \bar{z}_r \bar{z}_r \bar{z}_s \\
&\quad + \boldsymbol{\mathcal{D}}\left(\bar{\phi}_r,\bar{\phi}_r,\bar{\phi}_r,\phi_s\right)\bar{z}_r \bar{z}_r \bar{z}_r z_s + \boldsymbol{\mathcal{D}}\left(\bar{\phi}_r,\bar{\phi}_r,\bar{\phi}_r,\bar{\phi}_s\right)\bar{z}_r \bar{z}_r \bar{z}_r \bar{z}_s \\
d_{rrss} &= \boldsymbol{\mathcal{D}}\left(\phi_r,\phi_r,\phi_s,\phi_s\right)z_r z_r z_s z_s + 2\boldsymbol{\mathcal{D}}\left(\phi_r,\phi_r,\phi_s,\bar{\phi}_s\right)z_r z_r z_s \bar{z}_s + 2\boldsymbol{\mathcal{D}}\left(\bar{\phi}_r,\phi_r,\phi_s,\phi_s\right)\bar{z}_r z_r z_s z_s \\
&\quad + \boldsymbol{\mathcal{D}}\left(\bar{\phi}_r,\bar{\phi}_r,\phi_s,\phi_s\right)\bar{z}_r \bar{z}_r z_s z_s + 4\boldsymbol{\mathcal{D}}\left(\phi_r,\bar{\phi}_r,\phi_s,\bar{\phi}_s\right)z_r \bar{z}_r z_s \bar{z}_s + \boldsymbol{\mathcal{D}}\left(\phi_r,\phi_r,\bar{\phi}_s,\bar{\phi}_s\right)z_r z_r \bar{z}_s \bar{z}_s \\
&\quad + 2\boldsymbol{\mathcal{D}}\left(\bar{\phi}_r,\bar{\phi}_r,\bar{\phi}_s,\phi_s\right)\bar{z}_r \bar{z}_r \bar{z}_s z_s + 2\boldsymbol{\mathcal{D}}\left(\phi_r,\bar{\phi}_r,\bar{\phi}_s,\bar{\phi}_s\right)z_r \bar{z}_r \bar{z}_s \bar{z}_s + \boldsymbol{\mathcal{D}}\left(\bar{\phi}_r,\bar{\phi}_r,\bar{\phi}_s,\bar{\phi}_s\right)\bar{z}_r \bar{z}_r \bar{z}_s \bar{z}_s \\
d_{rsss} &= \boldsymbol{\mathcal{D}}\left(\phi_r,\phi_s,\phi_s,\phi_s\right)z_r z_s z_s z_s + 3\boldsymbol{\mathcal{D}}\left(\phi_r,\phi_s,\phi_s,\bar{\phi}_s\right)z_r z_s z_s \bar{z}_s + \boldsymbol{\mathcal{D}}\left(\bar{\phi}_r,\phi_s,\phi_s,\phi_s\right)\bar{z}_r z_s z_s z_s \\
&\quad + 2\boldsymbol{\mathcal{D}}\left(\bar{\phi}_r,\bar{\phi}_s,\phi_s,\phi_s\right)\bar{z}_r \bar{z}_s z_s z_s + 2\boldsymbol{\mathcal{D}}\left(\phi_r,\phi_s,\bar{\phi}_s,\bar{\phi}_s\right)z_r z_s \bar{z}_s \bar{z}_s + \boldsymbol{\mathcal{D}}\left(\phi_r,\bar{\phi}_s,\bar{\phi}_s,\bar{\phi}_s\right)z_r \bar{z}_s \bar{z}_s \bar{z}_s \\
&\quad + 3\boldsymbol{\mathcal{D}}\left(\bar{\phi}_r,\bar{\phi}_s,\bar{\phi}_s,\phi_s\right)\bar{z}_r \bar{z}_s \bar{z}_s z_s + \boldsymbol{\mathcal{D}}\left(\bar{\phi}_r,\bar{\phi}_s,\bar{\phi}_s,\bar{\phi}_s\right)\bar{z}_r \bar{z}_s \bar{z}_s \bar{z}_s \\
d_{rrst} &= \boldsymbol{\mathcal{D}}\left(\phi_r,\phi_r,\phi_s,\phi_t\right)z_r z_r z_s z_t + \boldsymbol{\mathcal{D}}\left(\phi_r,\phi_r,\phi_s,\bar{\phi}_t\right)z_r z_r z_s \bar{z}_t + \boldsymbol{\mathcal{D}}\left(\phi_r,\phi_r,\bar{\phi}_s,\phi_t\right)z_r z_r \bar{z}_s z_t \\
&\quad + 2\boldsymbol{\mathcal{D}}\left(\bar{\phi}_r,\phi_r,\phi_s,\phi_t\right)\bar{z}_r z_r z_s z_t + \boldsymbol{\mathcal{D}}\left(\phi_r,\phi_r,\bar{\phi}_s,\bar{\phi}_t\right)z_r z_r \bar{z}_s \bar{z}_t + \boldsymbol{\mathcal{D}}\left(\bar{\phi}_r,\bar{\phi}_r,\phi_s,\phi_t\right)\bar{z}_r \bar{z}_r z_s z_t \\
&\quad + 2\boldsymbol{\mathcal{D}}\left(\bar{\phi}_r,\phi_r,\bar{\phi}_s,\phi_t\right)\bar{z}_r z_r \bar{z}_s z_t + 2\boldsymbol{\mathcal{D}}\left(\bar{\phi}_r,\phi_r,\phi_s,\bar{\phi}_t\right)\bar{z}_r z_r z_s \bar{z}_t + 2\boldsymbol{\mathcal{D}}\left(\phi_r,\bar{\phi}_r,\bar{\phi}_s,\bar{\phi}_t\right)z_r \bar{z}_r \bar{z}_s \bar{z}_t \\
&\quad + \boldsymbol{\mathcal{D}}\left(\bar{\phi}_r,\bar{\phi}_r,\bar{\phi}_s,\phi_t\right)\bar{z}_r \bar{z}_r \bar{z}_s z_t + \boldsymbol{\mathcal{D}}\left(\bar{\phi}_r,\bar{\phi}_r,\phi_s,\bar{\phi}_t\right)\bar{z}_r \bar{z}_r z_s \bar{z}_t + \boldsymbol{\mathcal{D}}\left(\bar{\phi}_r,\bar{\phi}_r,\bar{\phi}_s,\bar{\phi}_t\right)\bar{z}_r \bar{z}_r \bar{z}_s \bar{z}_t \\
d_{rsst} &= \boldsymbol{\mathcal{D}}\left(\phi_r,\phi_s,\phi_s,\phi_t\right)z_r z_s z_s z_t + \boldsymbol{\mathcal{D}}\left(\phi_r,\phi_s,\phi_s,\bar{\phi}_t\right)z_r z_s z_s \bar{z}_t + \boldsymbol{\mathcal{D}}\left(\bar{\phi}_r,\phi_s,\phi_s,\phi_t\right)\bar{z}_r z_s z_s z_t \\
&\quad + 2\boldsymbol{\mathcal{D}}\left(\phi_r,\bar{\phi}_s,\phi_s,\phi_t\right)z_r \bar{z}_s z_s z_t + \boldsymbol{\mathcal{D}}\left(\bar{\phi}_r,\phi_s,\phi_s,\bar{\phi}_t\right)\bar{z}_r z_s z_s \bar{z}_t + \boldsymbol{\mathcal{D}}\left(\phi_r,\bar{\phi}_s,\bar{\phi}_s,\phi_t\right)z_r \bar{z}_s \bar{z}_s z_t \\
&\quad + 2\boldsymbol{\mathcal{D}}\left(\bar{\phi}_r,\phi_s,\bar{\phi}_s,\phi_t\right)\bar{z}_r z_s \bar{z}_s z_t + 2\boldsymbol{\mathcal{D}}\left(\phi_r,\bar{\phi}_s,\phi_s,\bar{\phi}_t\right)z_r \bar{z}_s z_s \bar{z}_t + \boldsymbol{\mathcal{D}}\left(\bar{\phi}_r,\bar{\phi}_s,\bar{\phi}_s,\phi_t\right)\bar{z}_r \bar{z}_s \bar{z}_s z_t \\
&\quad + \boldsymbol{\mathcal{D}}\left(\phi_r,\bar{\phi}_s,\bar{\phi}_s,\bar{\phi}_t\right)z_r \bar{z}_s \bar{z}_s \bar{z}_t + 2\boldsymbol{\mathcal{D}}\left(\bar{\phi}_r,\phi_s,\bar{\phi}_s,\bar{\phi}_t\right)\bar{z}_r z_s \bar{z}_s \bar{z}_t + \boldsymbol{\mathcal{D}}\left(\bar{\phi}_r,\bar{\phi}_s,\bar{\phi}_s,\bar{\phi}_t\right)\bar{z}_r \bar{z}_s \bar{z}_s \bar{z}_t \\
d_{rstt} &= \boldsymbol{\mathcal{D}}\left(\phi_r,\phi_s,\phi_t,\phi_t\right)z_r z_s z_t z_t + 2\boldsymbol{\mathcal{D}}\left(\phi_r,\phi_s,\phi_t,\bar{\phi}_t\right)z_r z_s z_t \bar{z}_t + \boldsymbol{\mathcal{D}}\left(\phi_r,\bar{\phi}_s,\phi_t,\phi_t\right)z_r \bar{z}_s z_t z_t \\
&\quad + \boldsymbol{\mathcal{D}}\left(\bar{\phi}_r,\phi_s,\phi_t,\phi_t\right)\bar{z}_r z_s z_t z_t + \boldsymbol{\mathcal{D}}\left(\phi_r,\phi_s,\bar{\phi}_t,\bar{\phi}_t\right)z_r z_s \bar{z}_t \bar{z}_t + 2\boldsymbol{\mathcal{D}}\left(\phi_r,\bar{\phi}_s,\bar{\phi}_t,\phi_t\right)z_r \bar{z}_s \bar{z}_t z_t \\
&\quad + 2\boldsymbol{\mathcal{D}}\left(\bar{\phi}_r,\phi_s,\bar{\phi}_t,\phi_t\right)\bar{z}_r z_s \bar{z}_t z_t + \boldsymbol{\mathcal{D}}\left(\bar{\phi}_r,\bar{\phi}_s,\phi_t,\bar{\phi}_t\right)\bar{z}_r \bar{z}_s z_t \bar{z}_t + 2\boldsymbol{\mathcal{D}}\left(\bar{\phi}_r,\bar{\phi}_s,\bar{\phi}_t,\phi_t\right)\bar{z}_r \bar{z}_s \bar{z}_t z_t \\
&\quad + \boldsymbol{\mathcal{D}}\left(\bar{\phi}_r,\phi_s,\bar{\phi}_t,\bar{\phi}_t\right)\bar{z}_r z_s \bar{z}_t \bar{z}_t + \boldsymbol{\mathcal{D}}\left(\phi_r,\bar{\phi}_s,\bar{\phi}_t,\bar{\phi}_t\right)z_r \bar{z}_s \bar{z}_t \bar{z}_t + \boldsymbol{\mathcal{D}}\left(\bar{\phi}_r,\bar{\phi}_s,\bar{\phi}_t,\bar{\phi}_t\right)\bar{z}_r \bar{z}_s \bar{z}_t \bar{z}_t \\
d_{rstu} &= \boldsymbol{\mathcal{D}}\left(\phi_r,\phi_s,\phi_t,\phi_u\right)z_r z_s z_t z_u + \boldsymbol{\mathcal{D}}\left(\phi_r,\phi_s,\phi_t,\bar{\phi}_u\right)z_r z_s z_t \bar{z}_u + \boldsymbol{\mathcal{D}}\left(\phi_r,\phi_s,\bar{\phi}_t,\phi_u\right)z_r z_s \bar{z}_t z_u \\
&\quad + \boldsymbol{\mathcal{D}}\left(\phi_r,\bar{\phi}_s,\phi_t,\phi_u\right)z_r \bar{z}_s z_t z_u + \boldsymbol{\mathcal{D}}\left(\bar{\phi}_r,\phi_s,\phi_t,\phi_u\right)\bar{z}_r z_s z_t z_u + \boldsymbol{\mathcal{D}}\left(\bar{\phi}_r,\bar{\phi}_s,\phi_t,\phi_u\right)\bar{z}_r \bar{z}_s z_t z_u \\
&\quad + \boldsymbol{\mathcal{D}}\left(\phi_r,\bar{\phi}_s,\bar{\phi}_t,\phi_u\right)z_r \bar{z}_s \bar{z}_t z_u + \boldsymbol{\mathcal{D}}\left(\phi_r,\phi_s,\bar{\phi}_t,\bar{\phi}_u\right)z_r z_s \bar{z}_t \bar{z}_u + \boldsymbol{\mathcal{D}}\left(\bar{\phi}_r,\phi_s,\phi_t,\bar{\phi}_u\right)\bar{z}_r z_s z_t \bar{z}_u \\
&\quad + \boldsymbol{\mathcal{D}}\left(\bar{\phi}_r,\phi_s,\bar{\phi}_t,\phi_u\right)\bar{z}_r z_s \bar{z}_t z_u + \boldsymbol{\mathcal{D}}\left(\phi_r,\bar{\phi}_s,\phi_t,\bar{\phi}_u\right)z_r \bar{z}_s z_t \bar{z}_u + \boldsymbol{\mathcal{D}}\left(\bar{\phi}_r,\bar{\phi}_s,\phi_t,\phi_u\right)\bar{z}_r \bar{z}_s z_t z_u \\
&\quad + \boldsymbol{\mathcal{D}}\left(\bar{\phi}_r,\bar{\phi}_s,\phi_t,\bar{\phi}_u\right)\bar{z}_r \bar{z}_s z_t \bar{z}_u + \boldsymbol{\mathcal{D}}\left(\bar{\phi}_r,\phi_s,\bar{\phi}_t,\bar{\phi}_u\right)\bar{z}_r z_s \bar{z}_t \bar{z}_u + \boldsymbol{\mathcal{D}}\left(\phi_r,\bar{\phi}_s,\bar{\phi}_t,\bar{\phi}_u\right)z_r \bar{z}_s \bar{z}_t \bar{z}_u \\
&\quad + \boldsymbol{\mathcal{D}}\left(\bar{\phi}_r,\bar{\phi}_s,\bar{\phi}_t,\bar{\phi}_u\right)\bar{z}_r \bar{z}_s \bar{z}_t \bar{z}_u
\end{aligned}
\tag{A.3}
$$

while similar expressions can be obtained for functions required for $\boldsymbol{\mathcal{E}}$. These are omitted here for clarity while the different permutations of subscripts are shown below. Then, using the auxiliary terms, functions $\boldsymbol{\mathcal{B}}$ through $\boldsymbol{\mathcal{E}}$ contained in function $\boldsymbol{F}$ are fully expanded as

$$\begin{aligned}
\boldsymbol{\mathcal{B}}(\boldsymbol{w},\boldsymbol{w}) &= \sum_{r,s=1}^{m} b_{rs} \\
\boldsymbol{\mathcal{C}}(\boldsymbol{w},\boldsymbol{w},\boldsymbol{w}) &= \sum_{r,s,t=1}^{m} c_{rst} \\
\boldsymbol{\mathcal{D}}(\boldsymbol{w},\boldsymbol{w},\boldsymbol{w},\boldsymbol{w}) &= \sum_{r,s,t,u=1}^{m} d_{rstu} \\
\boldsymbol{\mathcal{E}}(\boldsymbol{w},\boldsymbol{w},\boldsymbol{w},\boldsymbol{w},\boldsymbol{w}) &= \sum_{r,s,t,u,v=1}^{m} e_{rstuv}
\end{aligned} \tag{A.4}$$

Exploiting symmetry properties, the functions $\boldsymbol{\mathcal{B}}$ through $\boldsymbol{\mathcal{E}}$ are reformulated as

$$\begin{aligned}
\boldsymbol{\mathcal{B}}(\boldsymbol{w},\boldsymbol{w}) &= \sum_{r=1}^{m}\left(b_{rr} + \sum_{s=r+1}^{m} 2b_{rs}\right) \\
\boldsymbol{\mathcal{C}}(\boldsymbol{w},\boldsymbol{w},\boldsymbol{w}) &= \sum_{r=1}^{m}\left(c_{rrr} + \sum_{s=r+1}^{m}\left(3\left(c_{rrs}+c_{rss}\right) + \sum_{t=s+1}^{m} 6c_{rst}\right)\right) \\
\boldsymbol{\mathcal{D}}(\boldsymbol{w},\boldsymbol{w},\boldsymbol{w},\boldsymbol{w}) &= \sum_{r=1}^{m}\left(d_{rrrr} + \sum_{s=r+1}^{m}\left(4d_{rrrs} + 6d_{rrss} + 4d_{rsss}\right.\right. \\
&\quad \left.\left. + \sum_{t=s+1}^{m}\left(12\left(d_{rrst}+d_{rsst}+d_{rstt}\right) + \sum_{u=t+1}^{m} 24d_{rstu}\right)\right)\right) \\
\boldsymbol{\mathcal{E}}(\boldsymbol{w},\boldsymbol{w},\boldsymbol{w},\boldsymbol{w},\boldsymbol{w}) &= \sum_{r=1}^{m}\left(e_{rrrrr} + \sum_{s=r+1}^{m}\left(5e_{rrrrs} + 10e_{rrrss} + 10e_{rrsss} + 5e_{rssss}\right.\right. \\
&\quad + \sum_{t=s+1}^{m}\left(20e_{rrrst} + 30e_{rrsst} + 30e_{rrstt} + 20e_{rssst} + 30e_{rsstt} + 20e_{rsttt}\right. \\
&\quad \left.\left.\left. + \sum_{u=t+1}^{m}\left(60\left(e_{rrstu}+e_{rsstu}+e_{rsttu}+e_{rstuu}\right) + \sum_{v=u+1}^{m} 120e_{rstuv}\right)\right)\right)\right)
\end{aligned} \tag{A.5}$$

The total number of terms based on these new formulations as given in Table A.1 as well as the direct approach are illustrated in Fig. 2.1.

As discussed in Section 2.3, finite difference evaluations are often required to form the terms when analytical expressions of the derivatives are not available. For example, the following second order central difference schemes in one argument vector $\boldsymbol{x}$ can be

used

$$
\begin{aligned}
A\boldsymbol{x} &= \tfrac{1}{2\varepsilon}\Big(\boldsymbol{R}_{+1} - \boldsymbol{R}_{-1}\Big) + \mathcal{O}\big(\varepsilon^2\big) \\
\boldsymbol{\mathcal{B}}\left(\boldsymbol{x},\boldsymbol{x}\right) &= \tfrac{1}{\varepsilon^2}\Big(\boldsymbol{R}_{+1} - 2\boldsymbol{R}_0 + \boldsymbol{R}_{-1}\Big) + \mathcal{O}\big(\varepsilon^2\big) \\
\boldsymbol{\mathcal{C}}\left(\boldsymbol{x},\boldsymbol{x},\boldsymbol{x}\right) &= \tfrac{1}{2\varepsilon^3}\Big(\boldsymbol{R}_{+2} - 2\boldsymbol{R}_{+1} + 2\boldsymbol{R}_{-1} - \boldsymbol{R}_{-2}\Big) + \mathcal{O}\big(\varepsilon^2\big) \\
\boldsymbol{\mathcal{D}}\left(\boldsymbol{x},\boldsymbol{x},\boldsymbol{x},\boldsymbol{x}\right) &= \tfrac{1}{\varepsilon^4}\Big(\boldsymbol{R}_{+2} - 4\boldsymbol{R}_{+1} + 6\boldsymbol{R}_0 - 4\boldsymbol{R}_{-1} + \boldsymbol{R}_{-2}\Big) + \mathcal{O}\big(\varepsilon^2\big) \\
\boldsymbol{\mathcal{E}}\left(\boldsymbol{x},\boldsymbol{x},\boldsymbol{x},\boldsymbol{x},\boldsymbol{x}\right) &= \tfrac{1}{2\varepsilon^5}\Big(\boldsymbol{R}_{+3} - 4\boldsymbol{R}_{+2} + 5\boldsymbol{R}_{+1} - 5\boldsymbol{R}_{-1} + 4\boldsymbol{R}_{-2} - \boldsymbol{R}_{-3}\Big) + \mathcal{O}\big(\varepsilon^2\big) \quad \text{(A.6)}
\end{aligned}
$$

where $\boldsymbol{R}_l = \boldsymbol{R}\left(\boldsymbol{W}_0 + l\varepsilon\boldsymbol{x}\right)$.

Appendix B

Details of Centre Manifold Dynamics

The determination of the terms $\boldsymbol{k}_{20}$, $\boldsymbol{k}_{11}$ and $\boldsymbol{k}_{02}$ begins with the expression for the time derivative of $\boldsymbol{y}$ in Eq. (2.14). This is given as

$$\boldsymbol{y} = \boldsymbol{w} - z\boldsymbol{\phi}_c - \bar{z}\bar{\boldsymbol{\phi}}_c = \boldsymbol{w} - \bar{\boldsymbol{\psi}}_c^T \boldsymbol{w}\boldsymbol{\phi}_c - \boldsymbol{\psi}_c^T \boldsymbol{w}\bar{\boldsymbol{\phi}}_c \tag{B.1}$$

$$\dot{\boldsymbol{y}} = \dot{\boldsymbol{w}} - \bar{\boldsymbol{\psi}}_c^T \dot{\boldsymbol{w}}\boldsymbol{\phi}_c - \boldsymbol{\psi}_c^T \dot{\boldsymbol{w}}\bar{\boldsymbol{\phi}}_c \tag{B.2}$$

Assuming a periodic variation in frequency ω for z that is

$$\dot{z} = i\omega z, \qquad \dot{\bar{z}} = -i\omega\bar{z} \tag{B.3}$$

it is possible to evaluate the time derivative of Eq. (2.15) directly

$$\dot{\boldsymbol{y}} = i\omega\boldsymbol{k}_{20}z^2 - i\omega\boldsymbol{k}_{02}\bar{z}^2 \tag{B.4}$$

Since Eq. (B.4) is second order in z and $\bar{z}$, for simplicity, it is possible to retain up to second order terms in z and $\bar{z}$ for the expression of $\dot{\boldsymbol{w}}$

$$\dot{\boldsymbol{w}} = A\boldsymbol{w} + \tfrac{1}{2}\boldsymbol{\mathcal{B}}(\boldsymbol{w},\boldsymbol{w}) + \mathcal{O}\left(z^3\right) \tag{B.5}$$

Substituting Eq. (B.5) into Eq. (B.2) gives

$$\begin{aligned}\dot{\boldsymbol{y}} = {} & A\boldsymbol{w} - \bar{\boldsymbol{\psi}}_c^T A\boldsymbol{w}\boldsymbol{\phi}_c - \boldsymbol{\psi}_c^T A\boldsymbol{w}\bar{\boldsymbol{\phi}}_c \\ & + \tfrac{1}{2}\boldsymbol{\mathcal{B}}(\boldsymbol{w},\boldsymbol{w}) - \tfrac{1}{2}\bar{\boldsymbol{\psi}}_c^T \boldsymbol{\mathcal{B}}(\boldsymbol{w},\boldsymbol{w})\boldsymbol{\phi}_c - \tfrac{1}{2}\boldsymbol{\psi}_c^T \boldsymbol{\mathcal{B}}(\boldsymbol{w},\boldsymbol{w})\bar{\boldsymbol{\phi}}_c\end{aligned} \tag{B.6}$$

$$\begin{aligned}\dot{\boldsymbol{y}} = A\boldsymbol{y} &+ \tfrac{1}{2}\left(\boldsymbol{\mathcal{B}}\left(\boldsymbol{\phi}_c,\boldsymbol{\phi}_c\right) - \bar{\boldsymbol{\psi}}_c^T\boldsymbol{\mathcal{B}}\left(\boldsymbol{\phi}_c,\boldsymbol{\phi}_c\right)\boldsymbol{\phi}_c - \boldsymbol{\psi}_c^T\boldsymbol{\mathcal{B}}\left(\boldsymbol{\phi}_c,\boldsymbol{\phi}_c\right)\bar{\boldsymbol{\phi}}_c\right) z^2 \\ &+ \left(\boldsymbol{\mathcal{B}}\left(\boldsymbol{\phi}_c,\bar{\boldsymbol{\phi}}_c\right) - \bar{\boldsymbol{\psi}}_c^T\boldsymbol{\mathcal{B}}\left(\boldsymbol{\phi}_c,\bar{\boldsymbol{\phi}}_c\right)\boldsymbol{\phi}_c - \boldsymbol{\psi}_c^T\boldsymbol{\mathcal{B}}\left(\boldsymbol{\phi}_c,\bar{\boldsymbol{\phi}}_c\right)\bar{\boldsymbol{\phi}}_c\right) z\bar{z} \\ &+ \frac{1}{2}\left(\boldsymbol{\mathcal{B}}\left(\bar{\boldsymbol{\phi}}_c,\bar{\boldsymbol{\phi}}_c\right) - \bar{\boldsymbol{\psi}}_c^T\boldsymbol{\mathcal{B}}\left(\bar{\boldsymbol{\phi}}_c,\bar{\boldsymbol{\phi}}_c\right)\boldsymbol{\phi}_c - \boldsymbol{\psi}_c^T\boldsymbol{\mathcal{B}}\left(\bar{\boldsymbol{\phi}}_c,\bar{\boldsymbol{\phi}}_c\right)\bar{\boldsymbol{\phi}}_c\right)\bar{z}^2 \end{aligned} \tag{B.7}$$

This is written in compact form

$$\dot{\boldsymbol{y}} = A\boldsymbol{y} + \frac{1}{2}\boldsymbol{H}_{20}z^2 + \boldsymbol{H}_{11}z\bar{z} + \frac{1}{2}\boldsymbol{H}_{02}\bar{z}^2 \tag{B.8}$$

where

$$\boldsymbol{H}_{20} = \boldsymbol{\mathcal{B}}\left(\boldsymbol{\phi}_c,\boldsymbol{\phi}_c\right) - \bar{\boldsymbol{\psi}}_c^T\boldsymbol{\mathcal{B}}\left(\boldsymbol{\phi}_c,\boldsymbol{\phi}_c\right)\boldsymbol{\phi}_c - \boldsymbol{\psi}_c^T\boldsymbol{\mathcal{B}}\left(\boldsymbol{\phi}_c,\boldsymbol{\phi}_c\right)\bar{\boldsymbol{\phi}}_c \tag{B.9}$$

$$\boldsymbol{H}_{11} = \boldsymbol{\mathcal{B}}\left(\boldsymbol{\phi}_c,\bar{\boldsymbol{\phi}}_c\right) - \bar{\boldsymbol{\psi}}_c^T\boldsymbol{\mathcal{B}}\left(\boldsymbol{\phi}_c,\bar{\boldsymbol{\phi}}_c\right)\boldsymbol{\phi}_c - \boldsymbol{\psi}_c^T\boldsymbol{\mathcal{B}}\left(\boldsymbol{\phi}_c,\bar{\boldsymbol{\phi}}_c\right)\bar{\boldsymbol{\phi}}_c \tag{B.10}$$

$$\boldsymbol{H}_{02} = \boldsymbol{\mathcal{B}}\left(\bar{\boldsymbol{\phi}}_c,\bar{\boldsymbol{\phi}}_c\right) - \bar{\boldsymbol{\psi}}_c^T\boldsymbol{\mathcal{B}}\left(\bar{\boldsymbol{\phi}}_c,\bar{\boldsymbol{\phi}}_c\right)\boldsymbol{\phi}_c - \boldsymbol{\psi}_c^T\boldsymbol{\mathcal{B}}\left(\bar{\boldsymbol{\phi}}_c,\bar{\boldsymbol{\phi}}_c\right)\bar{\boldsymbol{\phi}}_c \tag{B.11}$$

Comparing Eqs. (B.8) and (B.4) and equating the coefficients for z^2, $z\bar{z}$ and $\bar{z}^2$ results in explicit expressions for $\boldsymbol{k}_{20}$, $\boldsymbol{k}_{11}$ and $\boldsymbol{k}_{02}$

$$\left(i\omega I - \tfrac{1}{2}A\right)\boldsymbol{k}_{20} = \tfrac{1}{2}\boldsymbol{H}_{20} \tag{B.12}$$

$$\left(-i\omega I - \tfrac{1}{2}A\right)\boldsymbol{k}_{02} = \tfrac{1}{2}\boldsymbol{H}_{02} \tag{B.13}$$

$$-A\boldsymbol{k}_{11} = \boldsymbol{H}_{11} \tag{B.14}$$

The Eqs. (B.12), (B.13) and (B.14) provide direct solutions to $\boldsymbol{k}_{20}$, $\boldsymbol{k}_{11}$ and $\boldsymbol{k}_{02}$, respectively.

The explicit form of the functions $\boldsymbol{\mathcal{B}}$ and $\boldsymbol{\mathcal{C}}$ in Eq. (2.16) are given by

$$\begin{aligned}\boldsymbol{\mathcal{B}}\left(\boldsymbol{w},\boldsymbol{w}\right) = z^2\boldsymbol{\mathcal{B}}\left(\boldsymbol{\phi}_c,\boldsymbol{\phi}_c\right) + 2z\bar{z}\boldsymbol{\mathcal{B}}\left(\boldsymbol{\phi}_c,\bar{\boldsymbol{\phi}}_c\right) + \bar{z}^2\boldsymbol{\mathcal{B}}\left(\bar{\boldsymbol{\phi}}_c,\bar{\boldsymbol{\phi}}_c\right) \\ + 2z\boldsymbol{\mathcal{B}}\left(\boldsymbol{\phi}_c,\boldsymbol{y}\right) + 2\bar{z}\boldsymbol{\mathcal{B}}\left(\bar{\boldsymbol{\phi}}_c,\boldsymbol{y}\right) + \boldsymbol{\mathcal{B}}\left(\boldsymbol{y},\boldsymbol{y}\right)\end{aligned} \tag{B.15}$$

and

$$\begin{aligned}\boldsymbol{\mathcal{C}}\left(\boldsymbol{w},\boldsymbol{w},\boldsymbol{w}\right) = z^3\boldsymbol{\mathcal{C}}\left(\boldsymbol{\phi}_c,\boldsymbol{\phi}_c,\boldsymbol{\phi}_c\right) + 3z^2\bar{z}\boldsymbol{\mathcal{C}}\left(\boldsymbol{\phi}_c,\boldsymbol{\phi}_c,\bar{\boldsymbol{\phi}}_c\right) + 3z\bar{z}^2\boldsymbol{\mathcal{C}}\left(\boldsymbol{\phi}_c,\bar{\boldsymbol{\phi}}_c,\bar{\boldsymbol{\phi}}_c\right) \\ + \bar{z}^3\boldsymbol{\mathcal{C}}\left(\bar{\boldsymbol{\phi}}_c,\bar{\boldsymbol{\phi}}_c,\bar{\boldsymbol{\phi}}_c\right) + 3z^2\boldsymbol{\mathcal{C}}\left(\boldsymbol{\phi}_c,\boldsymbol{\phi}_c,\boldsymbol{y}\right) + 3\bar{z}^2\boldsymbol{\mathcal{C}}\left(\bar{\boldsymbol{\phi}}_c,\bar{\boldsymbol{\phi}}_c,\boldsymbol{y}\right) \\ + 3z\boldsymbol{\mathcal{C}}\left(\boldsymbol{\phi}_c,\boldsymbol{y},\boldsymbol{y}\right) + 3\bar{z}\boldsymbol{\mathcal{C}}\left(\bar{\boldsymbol{\phi}}_c,\boldsymbol{y},\boldsymbol{y}\right) + 6z\bar{z}\boldsymbol{\mathcal{C}}\left(\boldsymbol{\phi}_c,\bar{\boldsymbol{\phi}}_c,\boldsymbol{y}\right) + \boldsymbol{\mathcal{C}}\left(\boldsymbol{y},\boldsymbol{y},\boldsymbol{y}\right)\end{aligned} \tag{B.16}$$

similar expressions are obtained for $\boldsymbol{\mathcal{D}}$ and $\boldsymbol{\mathcal{E}}$.

Appendix C

Coefficients of Models

C.1 Pitch-Plunge Aerofoil with Trailing Edge Flap

Equation (3.23) and (3.24) in Chapter 3 are restated here

$$M\ddot{\boldsymbol{x}}_s + C\dot{\boldsymbol{x}}_s + K\boldsymbol{x}_s + \boldsymbol{k}_N + W\boldsymbol{w}_f = \boldsymbol{f}_a + \boldsymbol{f}_e$$

$$\dot{\boldsymbol{w}}_f = A_{ff}\boldsymbol{w}_f + A_{fx}\boldsymbol{x}_s + \boldsymbol{f}_g$$

The analytical evaluations of each term in these equations are given as follows

$$M = \begin{pmatrix} c_0 & c_1 & c_{17} \\ d_0 & d_1 & d_{17} \\ p_0 & p_1 & p_{16} \end{pmatrix} \tag{C.1}$$

$$C = \begin{pmatrix} c_2 & c_3 & c_{16} \\ d_5 & d_2 & d_{16} \\ p_2 & p_3 & p_{15} \end{pmatrix} \tag{C.2}$$

$$K = \begin{pmatrix} c_4 & c_6 & c_{15} \\ d_6 & d_3 & d_{15} \\ p_4 & p_5 & p_{12} \end{pmatrix} \tag{C.3}$$

$$\boldsymbol{k}_N = \begin{pmatrix} c_5\xi^3 + c_{51}\xi^5 \\ d_4\alpha^3 + d_{41}\alpha^5 \\ p_{13}\delta^3 + p_{14}\delta^5 \end{pmatrix} \tag{C.4}$$

$$W = \begin{pmatrix} c_9 & c_{10} & c_7 & c_8 & c_{11} & c_{12} & c_{13} & c_{14} \\ d_9 & d_{10} & d_7 & d_8 & d_{11} & d_{12} & d_{13} & d_{14} \\ p_6 & p_7 & p_8 & p_9 & p_{10} & p_{11} & 0 & 0 \end{pmatrix} \tag{C.5}$$

$$A_{fx} = \begin{pmatrix} 1 & 0 & 0 \\ 1 & 0 & 0 \\ 0 & 1 & 0 \\ 0 & 1 & 0 \\ 0 & 0 & 1 \\ 0 & 0 & 1 \\ 0 & 0 & 0 \\ 0 & 0 & 0 \end{pmatrix} \tag{C.6}$$

$$A_{ff} = -\mathrm{diag}\left(\varepsilon_1, \varepsilon_2, \varepsilon_1, \varepsilon_2, \varepsilon_1, \varepsilon_2, \varepsilon_3, \varepsilon_4\right) \tag{C.7}$$

$$\boldsymbol{f}_g = [0, 0, 0, 0, 0, 0, W_g, W_g]^T \tag{C.8}$$

$$\boldsymbol{f}_a = \begin{pmatrix} f(\tau) \\ g(\tau) \\ h(\tau) \end{pmatrix} \quad \text{and} \quad \boldsymbol{f}_e = \begin{pmatrix} 0 \\ 0 \\ \overline{H}_\delta(\tau) \end{pmatrix} \tag{C.9}$$

Here, the notation presented by Lee [46] is followed. The additional terms are introduced by extending the subscript numbers. The parameters for the plunge equation are

$$
\begin{aligned}
c_0 =& 1 + \frac{1}{\mu} \\
c_1 =& x_\alpha - \frac{a_h}{\mu} \\
c_2 =& 2\zeta_\xi \frac{\bar{\omega}_1}{\bar{u}} + \frac{2}{\mu}\left(1 - \Psi_1 - \Psi_2\right) \\
c_3 =& \frac{1}{\mu} + \frac{2}{\mu}\left(\tfrac{1}{2} - a_h\right)\left(1 - \Psi_1 - \Psi_2\right) \\
c_4 =& \frac{\bar{\omega}_1^2}{\bar{u}^2} + \frac{2}{\mu}\left(\varepsilon_1\Psi_1 + \varepsilon_2\Psi_2\right) \\
c_5 =& \frac{\bar{\omega}_1^2}{\bar{u}^2}\beta_\xi \\
c_{51} =& \frac{\bar{\omega}_1^2}{\bar{u}^2}\beta_{\xi 5} \\
c_6 =& \frac{2}{\mu}\left(\left(1 - \Psi_1 - \Psi_2\right) + \left(\tfrac{1}{2} - a_h\right)\left(\varepsilon_1\Psi_1 + \varepsilon_2\Psi_2\right)\right) \\
c_7 =& \frac{2}{\mu}\varepsilon_1\Psi_1\left(1 - \varepsilon_1\left(\tfrac{1}{2} - a_h\right)\right) \\
c_8 =& \frac{2}{\mu}\varepsilon_2\Psi_2\left(1 - \varepsilon_2\left(\tfrac{1}{2} - a_h\right)\right) \\
c_9 =& -\frac{2}{\mu}\varepsilon_1^2\Psi_1 \\
c_{10} =& -\frac{2}{\mu}\varepsilon_2^2\Psi_2 \\
c_{11} =& \frac{\varepsilon_1\Psi_1}{\pi\mu}\left(2T_{10} - \varepsilon_1 T_{11}\right) \\
c_{12} =& \frac{\varepsilon_2\Psi_2}{\pi\mu}\left(2T_{10} - \varepsilon_2 T_{11}\right) \\
c_{13} =& \frac{2}{\mu}\varepsilon_3\Psi_3 \\
c_{14} =& \frac{2}{\mu}\varepsilon_4\Psi_4 \\
c_{15} =& \frac{1}{\pi\mu}\left(2T_{10}\left(1 - \Psi_1 - \Psi_2\right) + T_{11}\left(\varepsilon_1\Psi_1 + \varepsilon_2\Psi_2\right)\right) \\
c_{16} =& \frac{1}{\pi\mu}\left(-T_4 + T_{11}\left(1 - \Psi_1 - \Psi_2\right)\right) \\
c_{17} =& x_\delta - \frac{1}{\pi\mu}T_1
\end{aligned}
\tag{C.10}
$$

The parameters for the pitch equation are

$$
\begin{aligned}
d_0 =& \frac{x_\alpha}{r_\alpha^2} - \frac{a_h}{\mu r_\alpha^2} \\
d_1 =& 1 + \frac{a_h^2}{\mu r_\alpha^2} + \frac{1}{8\mu r_\alpha^2} \\
d_2 =& 2\zeta_\alpha \frac{1}{\bar{u}} - \frac{1}{\mu r_\alpha^2}\left(\left(2a_h+1\right)\left(\tfrac{1}{2}-a_h\right)\left(1-\Psi_1-\Psi_2\right) - \left(\tfrac{1}{2}-a_h\right)\right) \\
d_3 =& \frac{1}{\bar{u}^2} - \frac{1}{\mu r_\alpha^2}\left(\left(2a_h+1\right)\left(1-\Psi_1-\Psi_2\right) + \left(2a_h+1\right)\left(\tfrac{1}{2}-a_h\right)\left(\varepsilon_1\Psi_1+\varepsilon_2\Psi_2\right)\right) \\
d_4 =& \frac{1}{\bar{u}^2}\beta_\alpha \\
d_{41} =& \frac{1}{\bar{u}^2}\beta_{\alpha 5} \\
d_5 =& -\frac{\left(2a_h+1\right)}{\mu r_\alpha^2}\left(1-\Psi_1-\Psi_2\right) \\
d_6 =& -\frac{\left(2a_h+1\right)}{\mu r_\alpha^2}\left(\varepsilon_1\Psi_1+\varepsilon_2\Psi_2\right) \\
d_7 =& -\frac{\left(2a_h+1\right)}{\mu r_\alpha^2}\varepsilon_1\Psi_1\left(1-\varepsilon_1\left(\tfrac{1}{2}-a_h\right)\right) \\
d_8 =& -\frac{\left(2a_h+1\right)}{\mu r_\alpha^2}\varepsilon_2\Psi_2\left(1-\varepsilon_2\left(\tfrac{1}{2}-a_h\right)\right) \\
d_9 =& \frac{\left(2a_h+1\right)}{\mu r_\alpha^2}\varepsilon_1^2\Psi_1 \\
d_{10} =& \frac{\left(2a_h+1\right)}{\mu r_\alpha^2}\varepsilon_2^2\Psi_2 \\
d_{11} =& -\frac{\left(2a_h+1\right)}{\pi\mu r_\alpha^2}\left(T_{10}\varepsilon_1\Psi_1 - \tfrac{1}{2}T_{11}\varepsilon_1^2\Psi_1\right) \\
d_{12} =& -\frac{\left(2a_h+1\right)}{\pi\mu r_\alpha^2}\left(T_{10}\varepsilon_2\Psi_2 - \tfrac{1}{2}T_{11}\varepsilon_2^2\Psi_2\right) \\
d_{13} =& -\frac{\left(2a_h+1\right)}{\mu r_\alpha^2}\varepsilon_3\Psi_3 \\
d_{14} =& -\frac{\left(2a_h+1\right)}{\mu r_\alpha^2}\varepsilon_4\Psi_4 \\
d_{15} =& -\frac{1}{\pi\mu r_\alpha^2}\left(-\left(T_4+T_{10}\right) + \left(2a_h+1\right)\left(T_{10}\left(1-\Psi_1-\Psi_2\right) + \tfrac{1}{2}T_{11}\left(\varepsilon_1\Psi_1+\varepsilon_2\Psi_2\right)\right)\right) \\
d_{16} =& -\frac{1}{\pi\mu r_\alpha^2}\left(-\left(T_1 - T_8 - \left(c_h-a_h\right)T_4\right) + T_{11}\right) + \left(a_h+\tfrac{1}{2}\right)\tfrac{1}{2}T_{11}\left(1-\Psi_1-\Psi_2\right) \\
d_{17} =& \left(\frac{r_\delta^2}{r_\alpha^2} + \frac{\left(c_h-a_h\right)x_\delta}{r_\alpha^2}\right) - \frac{1}{\pi\mu r_\alpha^2}\left(T_7 + \left(c_h-a_h\right)T_1\right)
\end{aligned}
\tag{C.11}
$$

Defining the expression $Q = \left(\pi\mu r_\delta^2\right)^{-1}$, the parameters for the flap equation are

$$
\begin{aligned}
p_0 =& \frac{x_\delta}{r_\delta^2} - QT_{11} \\
p_1 =& 1 + \frac{(c_h - a_h)\, x_\delta}{r_\delta^2} + 2QT_{13} \\
p_2 =& QT_{12}\left(1 - \Psi_1 - \Psi_2\right) \\
p_3 =& QT_{12}\left(\tfrac{1}{2} - a_h\right)\left(1 - \Psi_1 - \Psi_2\right) + Q\left(T_4\left(a_h - \tfrac{1}{2}\right) - T_1 - 2T_9\right) \\
p_4 =& QT_{12}\left(\varepsilon_1\Psi_1 + \varepsilon_2\Psi_2\right) \\
p_5 =& QT_{12}\left(\left(\tfrac{1}{2} - a_h\right)\left(\varepsilon_1\Psi_1 + \varepsilon_2\Psi_2\right) + \left(1 - \Psi_1 - \Psi_2\right)\right) \\
p_6 =& QT_{12}\left(\left(\tfrac{1}{2} - a_h\right)\left(-\varepsilon_1^2\Psi_1\right) + \varepsilon_1\Psi_1\right) \\
p_7 =& QT_{12}\left(\left(\tfrac{1}{2} - a_h\right)\left(-\varepsilon_2^2\Psi_2\right) + \varepsilon_2\Psi_2\right) \\
p_8 =& QT_{12}\left(-\varepsilon_1^2\Psi_1\right) \\
p_9 =& QT_{12}\left(-\varepsilon_2^2\Psi_2\right) \\
p_{10} =& QT_{12}\left(\tfrac{1}{2}\pi^{-1}T_{11}\left(-\varepsilon_1^2\Psi_1\right) + \pi^{-1}T_{10}\left(\varepsilon_1\Psi_1\right)\right) \\
p_{11} =& QT_{12}\left(\tfrac{1}{2}\pi^{-1}T_{11}\left(-\varepsilon_2^2\Psi_2\right) + \pi^{-1}T_{10}\left(\varepsilon_2\Psi_2\right)\right) \\
p_{12} =& \frac{\bar{\omega}_2^2}{\bar{u}^2} + QT_{12}\left(\tfrac{1}{2}\pi^{-1}T_{11}\left(\varepsilon_1\Psi_1 + \varepsilon_2\Psi_2\right) + \pi^{-1}T_{10}\left(1 - \Psi_1 - \Psi_2\right)\right) + Q\pi^{-1}\left(T_5 - T_4T_{10}\right) \\
p_{13} =& \frac{\bar{\omega}_2^2}{\bar{u}^2}\beta_\delta \\
p_{14} =& \frac{\bar{\omega}_2^2}{\bar{u}^2}\beta_{\delta 5} \\
p_{15} =& 2\zeta_\delta\tfrac{\bar{\omega}_2}{\bar{u}} + QT_{12}\left(\tfrac{1}{2}\pi^{-1}T_{11}\left(1 - \Psi_1 - \Psi_2\right)\right) + Q\tfrac{1}{2}\pi^{-1}\left(-T_4T_{11}\right) \\
p_{16} =& 1 - Q\pi^{-1}T_3
\end{aligned}
$$

Integration by parts of Eqs. (3.12) through (3.14) leaves the following terms depending on initial conditions

$$
\begin{aligned}
f(\tau) &= \frac{2}{\mu}\left(\xi(0) + \left(\tfrac{1}{2} - a_h\right)\alpha(0) + \tfrac{1}{2}\pi^{-1}T_{11}\delta(0)\right)\left(\varepsilon_1\Psi_1 e^{-\varepsilon_1\tau} + \varepsilon_2\Psi_2 e^{-\varepsilon_2\tau}\right) \\
g(\tau) &= -\frac{2a_h + 1}{2r_\alpha^2} f(\tau) \\
h(\tau) &= \frac{1}{2}T_{12}Q\mu f(\tau)
\end{aligned}
\tag{C.12}
$$

Similarly for Eqs. (3.16) and (3.17), we find

$$
\begin{aligned}
f^g(\tau) &= -\frac{2}{\mu\bar{u}}\left(1 - \Psi_3 - \Psi_4\right) W_g(\tau) = 0 \\
g^g(\tau) &= -\frac{(2a_h + 1)}{2r_\alpha^2} f^g(\tau) = 0
\end{aligned}
\tag{C.13}
$$

Note that $1 - \Psi_3 - \Psi_4$ is zero.

C.2 Geometrically Exact Nonlinear Beam

Equation (4.12) in Chapter 4 is restated here

$$\boldsymbol{F}^{(j)A} = M_a^{(j)A}\ddot{\boldsymbol{x}}_e^{(j)A} + C_a^{(j)A}\dot{\boldsymbol{x}}_e^{(j)A} + K_a^{(j)A}\boldsymbol{x}_e^{(j)A} + D_a^{(j)A}\boldsymbol{w}^{(j)} + B_c^{(j)}\boldsymbol{u}_c^{(j)} + B_g^{(j)}W_g$$

The non-zero components of the matrices in this equation are

$$\begin{aligned}
&M_{a22}^{(j)} = -q_0c_1, && M_{a26}^{(j)} = -q_0c_2, && M_{a62}^{(j)} = q_0cd_1, && M_{a66}^{(j)} = q_0cd_2\\
&C_{a22}^{(j)} = -q_1c_3, && C_{a26}^{(j)} = -q_1c_4, && C_{a62}^{(j)} = q_1cd_3, && C_{a66}^{(j)} = q_1cd_4\\
&K_{a22}^{(j)} = -q_2c_5, && K_{a26}^{(j)} = -q_2c_6, && K_{a62}^{(j)} = q_2cd_5, && K_{a66}^{(j)} = q_2cd_6\\
&B_{c21}^{(j)} = -q_2c_{15} && B_{c22}^{(j)} = -q_1c_{16} && B_{c23}^{(j)} = -q_0c_{17}\\
&B_{c61}^{(j)} = -q_2cd_{15} && B_{c62}^{(j)} = -q_1cd_{16} && B_{c63}^{(j)} = -q_0cd_{17}
\end{aligned}$$

$$\begin{aligned}
D_{a2k}^{(j)} &= -q_2c_{6+k}, \quad \text{for} \quad k = 1, 2, ..., 8\\
D_{a6k}^{(j)} &= -q_2cd_{6+k}, \quad \text{for} \quad k = 1, 2, ..., 8
\end{aligned} \tag{C.14}$$

where $q_0 = \frac{1}{2}\rho S$, $q_1 = q_0U$, $q_2 = q_1U$. Note that q_2 is the dynamic pressure and S is the beam finite element reference area.

Equation (4.13) in Chapter 4 is restated here

$$\dot{\boldsymbol{w}}^{(j)} = A_{ff}^{(j)}\boldsymbol{w}^{(j)} + A_{fx}^{(j)}\boldsymbol{x}_e^{(j)A} + A_{fc}^{(j)}\boldsymbol{u}_c^{(j)} + A_{fg}^{(j)}W_g$$

The non-zero components of the matrices in this equation are

$$\begin{aligned}
&A_{fx16}^{(j)} = \tfrac{U}{b} && A_{fx26}^{(j)} = \tfrac{U}{b}, && A_{fx32}^{(j)} = \tfrac{U}{b^2} && A_{fx41}^{(j)} = \tfrac{U}{b^2}\\
&A_{ff11}^{(j)} = -\tfrac{\epsilon_1 U}{b} && A_{ff22}^{(j)} = -\tfrac{\epsilon_2 U}{b} && A_{ff33}^{(j)} = -\tfrac{\epsilon_1 U}{b} && A_{ff44}^{(j)} = -\tfrac{\epsilon_2 U}{b}\\
&A_{ff55}^{(j)} = -\tfrac{\epsilon_1 U}{b} && A_{ff66}^{(j)} = -\tfrac{\epsilon_2 U}{b} && A_{ff77}^{(j)} = -\tfrac{\epsilon_3 U}{b} && A_{ff88}^{(j)} = -\tfrac{\epsilon_4 U}{b}\\
&A_{fc51}^{(j)} = \tfrac{U}{b} && A_{fc61}^{(j)} = \tfrac{U}{b} && A_{fg71}^{(j)} = \tfrac{U}{b} && A_{fg81}^{(j)} = \tfrac{U}{b}
\end{aligned} \tag{C.15}$$

The explicit expressions for the coefficients of the above matrices are computed only once for a given geometry and corresponding aerodynamic model and are given as

$$
\begin{aligned}
c_1 &= \pi b \\
c_2 &= -\pi a_h b^2 \\
c_3 &= 2\pi(1 - \Psi_1 - \Psi_2) \\
c_4 &= \pi b(1 + (1 - 2a_h)(1 - \Psi_1 - \Psi_2)) \\
c_5 &= \frac{2\pi}{b}(\epsilon_1\Psi_1 + \epsilon_2\Psi_2) \\
c_6 &= 2\pi((1 - \Psi_1 - \Psi_2) + (\tfrac{1}{2} - a_h)(\epsilon_1\Psi_1 + \epsilon_2\Psi_2)) \\
c_7 &= 2\pi\epsilon_1\Psi_1(1 - \epsilon_1(\tfrac{1}{2} - a_h)) \\
c_8 &= 2\pi\epsilon_2\Psi_2(1 - \epsilon_2(\tfrac{1}{2} - a_h)) \\
c_9 &= -2\pi\epsilon_1^2\Psi_1 \\
c_{10} &= -2\pi\epsilon_2^2\Psi_2 \\
c_{11} &= \epsilon_1\Psi_1 2T_{10} - \epsilon_1^2\Psi_1 T_{11} \\
c_{12} &= \epsilon_2\Psi_2 2T_{10} - \epsilon_2^2\Psi_2 T_{11} \\
c_{13} &= 2\pi\epsilon_3\Psi_3 \\
c_{14} &= 2\pi\epsilon_4\Psi_4 \\
c_{15} &= c_\delta \\
c_{16} &= b c_{\delta'} \\
c_{17} &= b^2 c_{\delta''}
\end{aligned}
\tag{C.16}
$$

$$
\begin{aligned}
d_1 &= \frac{\pi}{2} a_h b \\
d_2 &= -\frac{\pi}{2}(a_h^2 + \tfrac{1}{8}) b^2 \\
d_3 &= \pi(\tfrac{1}{2} + a_h)(1 - \Psi_1 - \Psi_2) \\
d_4 &= \pi b(\tfrac{1}{2} - a_h)((\tfrac{1}{2} + a_h)(1 - \Psi_1 - \Psi_2) - \tfrac{1}{2}) \\
d_5 &= \frac{\pi}{b}(\tfrac{1}{2} + a_h)(\epsilon_1 \Psi_1 + \epsilon_2 \Psi_2) \\
d_6 &= \pi(\tfrac{1}{2} + a_h)((1 - \Psi_1 - \Psi_2) + (\tfrac{1}{2} - a_h)((\epsilon_1 \Psi_1 + \epsilon_2 \Psi_2))) \\
d_7 &= \pi(\tfrac{1}{2} + a_h)(\epsilon_1 \Psi_1 (1 - \epsilon_1(\tfrac{1}{2} - a_h))) \\
d_8 &= \pi(\tfrac{1}{2} + a_h)(\epsilon_2 \Psi_2 (1 - \epsilon_2(\tfrac{1}{2} - a_h))) \\
d_9 &= -\pi(\tfrac{1}{2} + a_h)\epsilon_1^2 \Psi_1 \\
d_{10} &= -\pi(\tfrac{1}{2} + a_h)\epsilon_2^2 \Psi_2 \\
d_{11} &= (\tfrac{1}{2} + a_h)(T_{10}\epsilon_1 \Psi_1 - \tfrac{1}{2} T_{11} \epsilon_1^2 \Psi_1) \\
d_{12} &= (\tfrac{1}{2} + a_h)(T_{10}\epsilon_2 \Psi_2 - \tfrac{1}{2} T_{11} \epsilon_2^2 \Psi_2) \\
d_{13} &= \pi(\tfrac{1}{2} + a_h)\epsilon_3 \Psi_3 \\
d_{14} &= \pi(\tfrac{1}{2} + a_h)\epsilon_4 \Psi_4 \\
d_{15} &= d_\delta \\
d_{16} &= b d_{\delta'} \\
d_{17} &= b^2 d_{\delta''}
\end{aligned}
\tag{C.17}
$$

Note that these constants are dimensional and analogous to the non-dimensional coefficients derived for the 2D aerofoil models presented in Chapter 3 and given in Appendix C.1.

Appendix D

FFAST Aircraft Beam Element Geometric Properties

Table D.1: FFAST Aircraft Beam Element Geometric Properties

Element	A	I_1	I_2	J	c
1	0.2026	0.0269	0.3616	0.0992	10.800
2	0.1960	0.0260	0.3276	0.0957	10.800
3	0.1768	0.0212	0.2496	0.0778	9.4672
4	0.1528	0.0148	0.1739	0.0540	8.1350
5	0.1290	0.0100	0.1114	0.0363	7.3340
6	0.1133	0.0071	0.0797	0.0259	6.5332
7	0.1003	0.0052	0.0580	0.0188	5.7325
8	0.0851	0.0034	0.0378	0.0122	4.9287
9	0.0667	0.0018	0.0200	0.0065	4.1280
10	0.0442	$5.21E-04$	0.0058	0.0019	3.1325
11	0.0353	$3.45E-05$	$3.82E-04$	$1.32E-04$	2.1370